九州大学学術情報リポジトリ
Kyushu University Institutional Repository

Study on Experimental Demonstration and Numerical Simulation of Magnetic Thrust Chamber System

前野, 旭弘

https://doi.org/10.15017/1485068

出版情報：九州大学, 2014, 博士（工学）, 課程博士
バージョン：published
権利関係：全文ファイル公表済

KYUSHU UNIVERSITY

Doctoral Dissertation

Study on Experimental Demonstration and Numerical Simulation of Magnetic Thrust Chamber System
磁気スラストチャンバーシステムの実験的実証と数値シミュレーションに関する研究

指導教員　中島　秀紀　教授
指導教員　山本　直嗣　准教授

Kyushu University
Interdisciplinary Graduate School of Engineering Science Department of Advanced Energy Engineering School of Engineering Sciences

Akihiro Maeno

August 6, 2014

Contents

1 Introduction **1**

1.1 Interplanetary spaceflight 1

1.2 Nuclear fusion 2

1.3 Inertial Confinement Fusion 4

1.4 The Sun's energy 6

1.5 Laser Fusion Rocket 7

1.6 Magnetic thrust chamber system of LFR 7

1.7 Past works 10

1.8 Aim of this study 11

1.9 Table of contents 12

Bibliography 14

2 Laser-target interaction **18**

2.1 Introduction 18

2.2 Laser parameters 18

2.3 Elements of plasma physics 19

2.3.1 Dielectric functions for transverse and longitudinal plasma waves 19

2.3.2 Transverse electromagnetic waves 22

2.4 Collisional absorption of laser light in laser-produced plasma . 24

2.4.1 Scaling with wavelength and incident intensity 24

2.4.2 Absorption coefficient 24
2.4.3 Model for collisional absorption 25
2.4.4 Dependence of absorption on wavelength 25
2.5 1D Lagrangian radiation hydrodynamic code 26
2.5.1 Hydrodynamic equations 26
2.5.2 Radiative transport equations 29
2.6 Summary 29
Bibliography 31

3 3D Hybrid PIC Code 34
3.1 Introduction 34
3.2 Particles in electromagnetic field 35
3.2.1 PIC algorithm 35
3.2.2 Digital filter 37
3.3 Basic equations 39
3.4 Leapfrog algorithm 41
3.4.1 Initial steps 42
3.4.2 Cycle steps 44
3.5 Calculation of electromagnetic field 44
3.5.1 Plasma-vacuum interface 44
3.5.2 Predictor corrector algorithm for plasma region 46
Initial step 46
Cycle steps 47
3.5.3 SOR algorithm for vacuum region 48
3.6 Summary 50
Bibliography 51

4 Direct measurement of impulse 53
4.1 Introduction 53
4.2 Dependence of impulse on laser pulse duration 54

4.2.1 Experimental setup for EUV facility 54
4.2.2 Pendulum type thrust stand for EUV facility 57
4.2.3 Results and discussion for EUV facility 59
4.3 Dependence of impulse on laser pulse wavelength and incident laser energy 62
4.3.1 Experimental setup for GXII facility 62
4.3.2 Pendulum type thrust stand for GXII facility 62
4.3.3 Results and discussion for GXII facility 66
4.4 Comparison of measured and calculated impulse 68
4.4.1 Numerical simulation with and without considering creation process of laser-produced plasma 68
4.4.2 Results and discussion for numerical simulations 72
4.5 Summary 74
Bibliography 77

5 Comparison of ion expansion velocity 78
5.1 Introduction 78
5.2 Experiment for measuring ion expansion velocity 79
5.2.1 Experimental setup 79
5.2.2 Charge collector with a Faraday cup 81
5.2.3 Pulsed power supply for generating high pulsed current 83
Pulse Forming Network 83
Rogowski coil 86
5.3 Numerical simulation with and without considering creation process of laser-produced plasma 90
5.3.1 Calculation model of Star-1D 90
5.3.2 Results and discussion of Star-1D 92
5.3.3 Calculation model of 3D hybrid PIC code 94
5.4 Results and discussion 96

5.5 Summary 96
Bibliography 98

6 Effect of magnetic field **100**
6.1 Introduction 100
6.2 Dependence on ion expansion velocity distribution in initial laser-produced plasma 101
6.2.1 Calculation model of 3D hybrid PIC code 101
6.2.2 Results and discussion 104
Diamagnetic cavity 104
Thrust energy and impulse 108
Discussion 110
6.3 Thrust performances for various magnetic field strengths . . . 112
6.3.1 Numerical simulation conditions 112
6.3.2 Results and discussion 112
6.4 Summary 117

7 Summary **118**

A Ampere's law with Darwin approximation **123**

B Components of matrix equations **127**
B.1 x component of $\boldsymbol{v}_{\mathrm{i}}^{n+\frac{1}{2}}$ 127
B.2 x component of $\boldsymbol{E}^{n}$ 130

C Neumann boundary condition **131**

D Normalization **135**

E CFL condition **136**

List of Figures

1.1 Four stages of a direct-drive implosion. 5

1.2 Mechanism for generating impulse in the magnetic thrust chamber system of LFR. 9

2.1 Target irradiated and focused by a single laser beam. 20

2.2 Normal incidence of the laser light on planar ablation plasma. 27

2.3 Ion and electron temperature, ablation plasma velocity and electron density distributions in a laser-produced plasma. . . . 27

3.1 Particle and eight nearest grid points. • and ∘ shows particle and grid point, respectively. 36

3.2 Eighteen nearest grid points. The points indicate middle, side and corner points. 38

3.3 Update steps in time of leapfrog algorithm. 43

3.4 A schematic of the grid points used in the plasma and vacuum region. The black area is the outside of calculation region. . . 45

4.1 Vacuum chamber in the EUV facility. 55

4.2 Experimental setup for EUV facility. 55

4.3 Calculated magnetic field strength produced by the permanent magnets at the z-axis at $x = y = 0$ and in the $z - x$ plane at $y = 0$. The magnetic field strength at the origin is 0.12 T. . . 56

4.4 Schematic of the pendulum type thrust stand for EUV facility. (vertical sectional view) 58
4.5 Applied calibration force as a function of the signals of LED sensors and the liner curve fitting to the calibration data. . . . 58
4.6 Impulses measured on the pendulum type thrust stand as a function of incident laser energies for laser pulse duration of 3 ns and 9 ns. 61
4.7 Impulse model of the product of plasma ablation mass and ion acoustic speed. 61
4.8 Vacuum chamber in the GXII facility. 64
4.9 Experimental setup & Schematic of the pendulum type thrust stand for GXII facility. 64
4.10 Calculated magnetic field strength produced by the permanent magnet at the z-axis at $x = y = 0$ and in the $z - x$ plane at $y = 0$. The magnetic field strength at the origin is 0.1 T. . . . 65
4.11 Applied calibration force as a function of the signals of LED sensors and the liner curve fitting to the calibration data. . . . 65
4.12 Impulses measured on the pendulum type thrust stand as a function of incident laser energies for laser pulse wavelength. . 67
4.13 Maxwell super particle velocity distribution. The characteristic velocity is assumed to be v_p=2.4 km/s. 70
4.14 Cubic calculation model of 3D hybrid PIC code. 71
4.15 Unit vector distributions of diamagnetic current calculated by modified and original numerical simulation. 73

5.1 Experimental setup & Cubic calculation model of 3D hybrid PIC code. 80
5.2 Edgewise coil for generating a pulsed magnetic filed. 80

5.3 Charge collector with a Faraday cup and an I-V converter. The 2-mm-diameter hole is covered with a mesh to prevent electrons in the plasma from entering the Faraday cup. 82
5.4 Circuit diagram of pulsed power supply with a 3-step PFN. . . 85
5.5 Pulsed power supply made by myself. 85
5.6 Rogowski coil for measuring a pulsed current. 87
5.7 Equivalent circuit diagram of integral and non-inverting amplifier circuits. 87
5.8 Experimental and theoretical output currents of pulsed power supply at the peak current of 450 A. Current starts flowing 31 μs before laser ignition. 89
5.9 Lagrangian calculation model for ray-tracing. 91
5.10 Gaussian time-variable power profile of a single laser beam. . . 91
5.11 1D distributions of plasma for ion density, ion expansion velocity, and charge state as a function of plasma radius at 75 ns. 93
5.12 Time-variation of plasma kinetic, internal and radiation energies. 93
5.13 Calculated magnetic field strength produced by the edgewise coil at the peak current of 450 A. The magnetic field strength at the origin is 0.0321 T. 95

6.1 Cubic calculation model of 3D hybrid PIC code. 102
6.2 Calculated magnetic field strength produced by the edgewise coil when the peak current is 5.2 kA. The magnetic field strength at the center is 0.51 T. 102
6.3 Magnetic field strength distribution for the original case in $z-x$ plane at $y=0$ for calculation times of 325, 575, 825 ns, and 1.075 μs. A diamagnetic cavity is formed. 105

6.4 Magnetic field strength distribution for the original case in $z-x$ plane at $y = 0$ for calculation times of 1.325, 1.575, 3.075, and 3.575 μs. A diamagnetic cavity is formed. 106

6.5 Magnetic field strength distribution for the modified case in $z-x$ plane at $y = 0$ for calculation times of 1.325, 2.575, 3.825, and 5.075 μs. A diamagnetic cavity is formed. 107

6.6 Time evolutions of thrust energy and impulse. For the original case, thrust energy and impulse saturate at 0.36 J (31%) and 151 μNs (41%), respectively. For the modified case, thrust energy and impulse saturate at 0.37 J (12%) and 31.6 μNs (41%), respectively. 109

6.7 Time evolutions of thrust energy and impulse for (a) slow velocity group and (b) fast velocity group. For group A, thrust energy and impulse saturate at 0.0337 J (125%) and 24.1 μNs (102%). For group B, thrust energy and impulse saturate at 0.34 J (11%) and 7.5 μNs (14%), respectively. 111

6.8 Ion super particle distributions at B=0.0321 T calculated by modified and original numerical simulations. 114

6.9 Ion super particle distributions at B=0.961 T calculated by modified and original numerical simulations. 114

6.10 Ion super particle distributions at B=1.92 T calculated by modified and original numerical simulations. 115

6.11 Ion super particle distributions at B=2.88 T calculated by modified and original numerical simulations. 115

6.12 Impulse for various magnetic field strengths calculated by modified and original numerical simulations. 116

C.1 Orthogonal and nonorthogonal cells. 132

C.2 Two examples of Neumann boundary condition. 132

List of Tables

4.1 Plasma conditions for original and modified cases. 71

5.1 Plasma conditions for original and modified cases. 95

6.1 Plasma conditions for original and modified cases. 103

Chapter 1

Introduction

1.1 Interplanetary spaceflight

Great progress has already been made in exploring the earth and the moon with manned and unmanned missions and surveying other planets in the solar system by using unmanned probes. In the last 18 years, Jet Propulsion Laboratory (JPL) of National Aeronautics Space Administration (NASA) has strongly carried out some robotic space missions to Mars as part of JPL's Mars Exploration Program [1].

Firstly, "Mars Pathfinder" [2] was launched out in December 1996 from the earth and landed on Mars in July 1997. This spaceflight spent 212 days going to the planet. In this mission, from the investigations by scientific instruments on both the lander and the rover, it was suggested that Mars had been warm and existed liquid water in the atmosphere. Eight years later, in January 2004, two robotic geologists (Spirit and Opportunity) [3] landed on Mars after 202 days from they were launched out. This mission is named "Mars Exploration Rover." These robotic explorers have trekked across the Martian surface with surveying the field geology and observing the atmosphere. As a result, they have found that there were wet and habit-

able conditions on ancient Mars. NASA's next rover mission, "Mars Science Laboratory" [4], carried "Curiosity" to Mars. The rover arrived on Mars in August 2012 after a long trip of 254 days. Mars Science Laboratory has been collecting Martian soil and rock samples. These samples have been analyzed whether organic compounds and environmental conditions which could have supported microbial life are existing now or in the past. This rover also carries a radioisotope power system generating electricity from the heat of plutonium's radioactive decay. This power source enables Curiosity to operate a full Martian year (687 days) on Mars' surface.

The aim of JPL's Mars Exploration Program is to investigate the presence of liquid water on Mars, either existed in its ancient past or preserved in the subsurface today. Water is essential for lives. If Mars once had liquid water or still does today, it has the potential to support life. From these factors, the focus for manned transport in a century will undoubtedly be Mars.

However, it takes long time to Mars using electric propulsion (i.e., low thrust and high specific impulse). (Specific impulse is the ratio of the effective exhaust velocity and the acceleration due to gravity.) This means that spaceship crew stay in the harmful radiation environment of the interplanetary space for a long time. It is too dangerous for human. Thus, space propulsion systems which is capable of generating large thrust with high specific impulse will be required for manned interplanetary flights. Large thrust permits high accelerations up to a speed. In the systems, fusion-based nuclear propulsion has the potential to enable fast interplanetary transaction by the huge energy generated by fusion reaction.

1.2 Nuclear fusion

Einstein's Special relativity, probably the most famous equation in physics, is commonly written as $E = mc^2$. This equation represents the amount of

energy associated with the forces holding nucleus together. When light elements combine into a heavier element, the mass of the heavier element is slightly less than the sum of the mass of the light elements. The difference in mass per nucleus is called mass defect. The mass defect multiplied by the speed of light squared is the release energy by nuclear fusion [5]. Nuclear fusion is about 40 billion times more efficient in converting mass into energy than chemical reactions, and about 4 times more efficient than nuclear fission.

One promising nuclear fusion reaction is between deuterium and tritium. Deuterium-tritium (DT) reaction releases 17.6 MeV and produces helium-4 (^{4}He) and neutron (n). Deuterium is naturally present in water and available soon. Tritium is not available naturally and has to be produced from lithium being available widely.

$$\mathrm{D} + \mathrm{T} \rightarrow {}^4\mathrm{He}\ (3.5\mathrm{MeV}) + \mathrm{n}\ (14.1\mathrm{MeV}) \tag{1.1}$$

Another reaction is deuterium-helium-3 (D^{3}He) reaction. This reaction releases 18.4 MeV and produces only charged particle as helium-4 and a free proton (p), not neutron. However, there is a major problem to obtain helium-3 because it is not present on the earth. Although the moon's surface contains helium-3 brought by solar wind, the concentration is extremely low and it would require enormous mining effort to extract helium-3.

$$\mathrm{D} + {}^3\mathrm{He} \rightarrow {}^4\mathrm{He}\ (3.7\mathrm{MeV}) + \mathrm{p}\ (14.7\mathrm{MeV}) \tag{1.2}$$

To initiate these reactions, a lot of energy is needed to bring two nuclei into an encounter close enough. This is because the electric force trying to keep them apart dominates stronger than the attractive nuclear force between two nuclei. One typical approach is magnetic confinement fusion

(MCF). Microwaves or electricity heat and ionize a fuel gas in a vacuum chamber into a plasma state. Magnetic field guides the charged particles along the direction of the field and heats the fuel up. Another is inertial confinement fusion (ICF). Laser beams compress and heat so quickly before the fuel escapes.

1.3 Inertial Confinement Fusion

The ICF [6, 7] releases large amounts of energy and creates high energy density plasma in about 10 ps by focusing homogeneously laser beams onto a millimeter-sized capsule filled with nuclear fusion fuel. When the density of DT fuel is 0.3 g/cm^3, 425 MJ is released from a 2-mm-diameter capsule filled with DT fuel at 100% burn up. This energy equals to the energy released by the combustion of about 10 kg of gasoline. The main sequences of a direct-drive implosion are as follows and sketched in Fig. 1.1.

(a) Strong laser beams are homogeneously focused onto a millimeter-sized spherical fuel target.

(b) The laser energy is absorbed on the critical surface and generates ablation plasma on the outer layer. High pressure of the ablation plasma implodes inwards via a rocket effect.

(c) The capsule is compressed to a density several thousand times greater than that of solid materials. In the center of capsule, the kinetic energy of the compression is converted into the internal energy. When sufficient density and temperature is reached, a central hot spot region is created and ignites via fusion reactions.

(d) Then, a burn wave starting from the hot spot propagates and ignites the whole fuel. The nuclear fusion energy and productions are released.

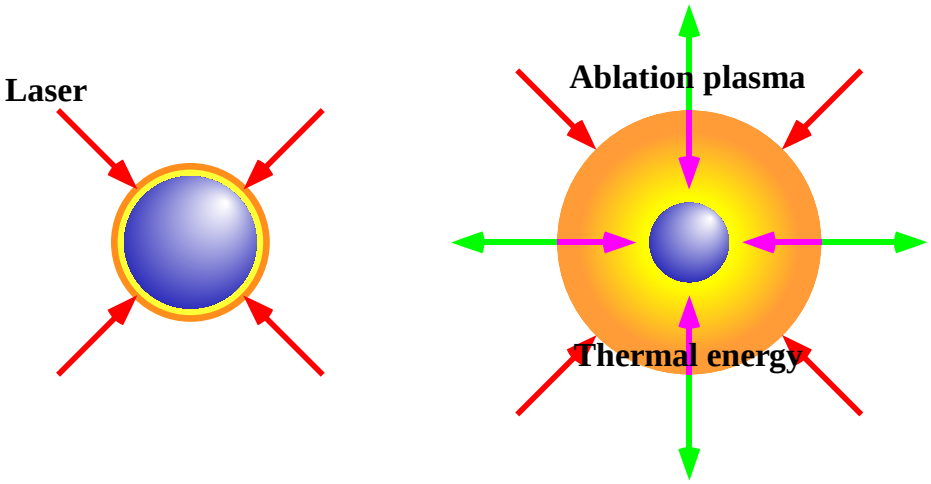

(a) Laser heating of the capsule outer layer.

(b) Ablation plasma of the outer layer compresses the capsule.

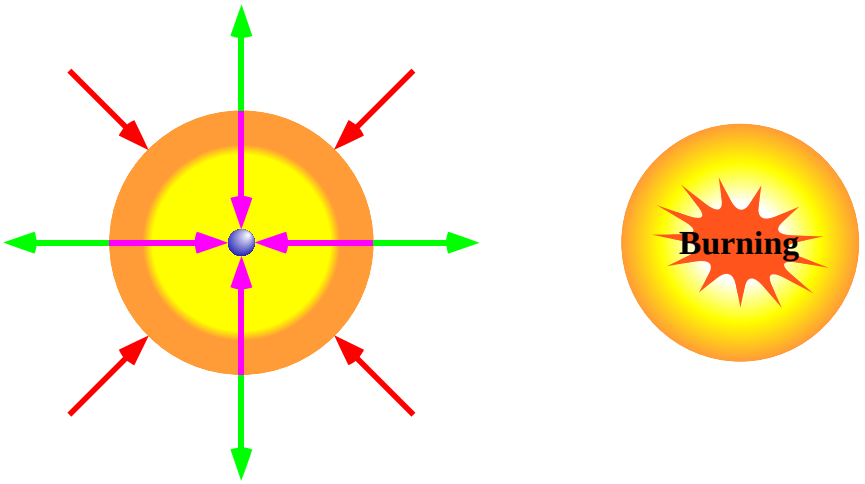

(c) Core reaches the density and temperature enough for ignition.

(d) Fusion reaction spreads rapidly through the compressed fuel.

Figure 1.1: Four stages of a direct-drive implosion.

1.4 The Sun's energy

ICF is the same principle as the Sun [8]. The Sun has a plenty of hydrogen for nuclear fusion. The nuclear fusion reaction in the Sun is the conversion of four protons into a helium-4. This reaction does not happen in a single step. Firstly, two protons combine to form a deuterium as shown in (1.3). The deuterium combines with another proton to form helium-3 as shown in (1.4). Finally, helium-4 and two protons are released from two helium-3 as shown in (1.5). The total amount of energy released from this reaction is about 10 million times more than the chemical reaction.

$$\mathrm{p} + \mathrm{p} \rightarrow \mathrm{D} + \text{positron} \tag{1.3}$$

$$\mathrm{D} + \mathrm{p} \rightarrow {}^{3}\mathrm{He} \tag{1.4}$$

$${}^{3}\mathrm{He} + {}^{3}\mathrm{He} \rightarrow {}^{4}\mathrm{He} + 2\mathrm{p} \tag{1.5}$$

The Sun has high dense core and low dense outer layers. The core exists from the center to 0.3 of the Sun's radius (about 0.7 million km). The hydrogen fuel is compressed to very high density (about 150 g/cm^3), roughly 150 times denser than water. The temperature in the core is about 15 million K. Nuclear fusion reactions take place only in the core. The combination of high density and high temperature makes an enormous pressure for expanding outward. To prevent this pressure, the Sun confines the expansion fusion plasma by the presence of a massive gravitational field of each layer. Gravity can confine the hot plasma despite a very weak force compared to the forces of nuclear physics. This is called hydrostatic equilibrium. In the other hand, the energy is transported outward from the core as the radiation heat through the radiative zone to 0.7 of the radius. As the distance increases from the core, the zone becomes more opaque and radiation becomes

less efficient. The temperature in this zone cools to 2 million K. Then, the energy begins to move through the convective zone outside 0.3 of the Sun's radius. Finally, the energy arrives at the photosphere (the temperature of about 6,000 K) emitting the sunlight. A series of these events is quite a slow process and it takes about a million years for getting out the energy.

1.5 Laser Fusion Rocket

The first concept of fusion-based nuclear propulsion [9] was proposed by Ulam of Los Alamos National Laboratory (LANL) in 1946 and extended further by Ulam and Everett in 1955. Then, Taylor and Dyson [10] conducted Project Orion at the LANL, in the 1950s. Since this project was planning to use hydrogen bomb in space, it was prohibited by the Partial Test Ban Treaty in 1963. Then, Project Daedalus [11] originated by Winterberg [12] was motivated by the British Interplanetary Society. At the same time, the application of ICF to space propulsion was firstly proposed in the 1970s by Balcomb [13] of Los Alamos Scientific Laboratory and Hyde, Wood and Nuckolls [14] of the Lawrence Livermore National Laboratory (LLNL). The propulsion system named as laser fusion rocket (LFR) [15] redirects the emitted charged particles in one direction by a magnetic field. Orth [16, 17] of LLNL estimated that an LFR employing DT reaction have an effective specific impulse of 15,500 s and a thrust of 230 kN. The peak magnetic field is 12 T. The period round-trip to Mars was also estimated to be close to 145 days. This is much shorter than the existing propulsion systems.

1.6 Magnetic thrust chamber system of LFR

LFR employs a magnetic thrust chamber system to generate impulse. The system produces impulse by inducing a diamagnetic current in a laser-

produced plasma as the following processes. Figure 1.2 depicts the mechanism for producing impulse in the system of LFR.

(a) ICF plasma expands in an applied magnetic field with a suitably designed geometry. The magnetic field is typically produced by a solenoid super-conducting magnet (SCM).

(b) Since plasmas are good conductors, the charged particles in the plasma undergo Larmor motion when a magnetic field is applied. This Larmor motion induces the diamagnetic current to sweep aside and compress the magnetic field.

(c) The compressed magnetic field pushes the plasma back in a manner similar to a spring. Then, LFR generates impulse through the interaction between the diamagnetic current in the plasma and the magnetic field generated by the SCM.

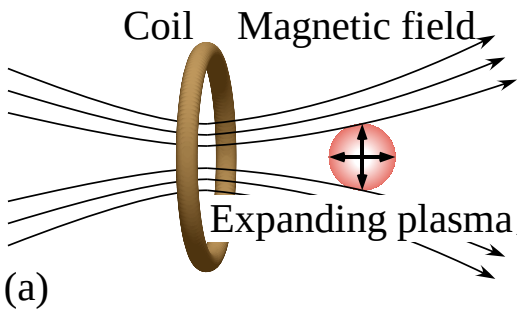

(a) Expanding ICF plasma in an applied magnetic field that has a suitably designed geometry.

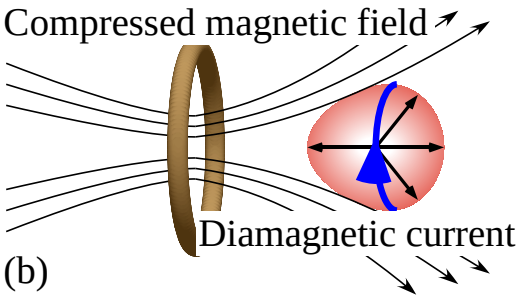

(b) Compressed magnetic field and diamagnetic current induced by Larmor motion.

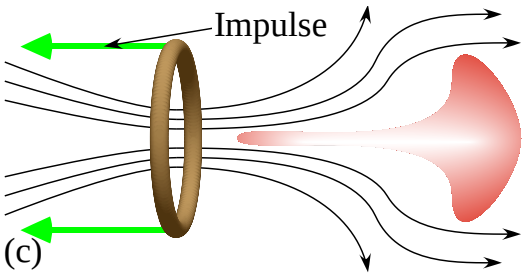

(c) Compressed magnetic field pushes plasma back. LFR produces impulse through the interaction between the diamagnetic current and the magnetic field.

Figure 1.2: Mechanism for generating impulse in the magnetic thrust chamber system of LFR.

The magnetic thrust chamber system of LFR has the following three advantages.

1. The galactic cosmic radiation is the greatest problem associated with manned spaceflight. LFR reduces the period of space missions and the exposure of the spaceflight crew to cosmic radiation because LFR can generate large thrusts with high specific impulses.

2. The thrust can be easily varied during the mission by varying the system parameters. For example, the thrust can be changed by varying the operation frequency of the system because the thrust is proportional to the production frequency of impulses.

3. This system has a long lifetime. The direct plasma impingement on the solid wall of the vehicle is minimized as the plasma is confined by the magnetic field produced by the SCM. Consequently, little charged plasma energy is wasted and the damage of the spacecraft structure is minimized, resulting in long lifetime.

1.7 Past works

The most important thing for realizing LFR is the magnetic thrust chamber system. Several numerical simulations and experiments have been performed to investigate the behavior of charged particles in a magnetic field for the magnetic thrust chamber system of LFR. In experiments, Vchivokv *et al.* [18] observed the temporal plasma behavior in an axially symmetric dipole magnetic field. By using a magnetic probe, they discovered that a diamagnetic cavity forms in the applied magnetic field. Pioneer works related to the plasma cloud expansion were conducted by a Japanese group. Sato *et al.* [19] studied experimentally and numerically the physical mechanism of reconverting the kinetic expansion energy of plasma into thermal energy as

the result of plasma-magnetic field interaction and the occurrence of plasma instability. In numerical simulations [20, 21, 22], Rayleigh-Taylor instability and electrons detachment from magnetic field were suffered. Rayleigh-Taylor instability is a serious problem for plasma explosion and would lead to the impulse reduction. The detachment problem is caused by the Larmor radius difference between ions and electrons. When electrons would not escape from the magnetic field of the system, ions would be pulled back to the space vehicle by the charge-separation electric field generated by the Larmor motions of the ions and electrons. As a result, the space vehicle cannot get enough impulse. Nagamine *et al.* [20] found that Rayleigh-Taylor instability would not be serious problems for the system by using a three-dimensional (3D) hybrid Particle-In-Cell (PIC) code which simulates the behavior of charged particles in a magnetic field. Kawabuchi *et al.* [21] found that electrons detachment would occur and generate impulse by using a two-dimensional (2D) coordinate space and a 3D velocity space electromagnetic full PIC code.

1.8 Aim of this study

Past works have evaluated the behavior of charged particles in a magnetic field for the magnetic thrust chamber system of LFR by using mainly numerical simulation. However, there have already left same challenges in the study of the magnetic thrust chamber system for LFR. To study three challenges of them, the followings are conducted.

1. The direct measurement of impulse due to the interaction between a diamagnetic current and a magnetic field has not been demonstrated experimentally yet. To produce the impulse by using laser-produced plasma and magnet, we attempt to conduct experiments in the actual research laboratory instead of ICF plasma and SCM. The experiments are conducted for various laser pulse energies at Extreme Ultra-Violet

(EUV) database and Gekko XII (GXII) laser facilities of Institute of Laser Engineering (ILE) in the collaboration with Osaka University.

2. The creation process of a laser-produced plasma has not sufficiently been considered in the numerical simulation yet. This process is needed to compare numerical simulations with experiments in the actual research laboratory. By combining a 3D hybrid PIC code with a one-dimensional (1D) Lagrangian radiation hydrodynamic code which can compute the hydrodynamic evolution of radiating plasma heated by laser pulses, we attempt to compute high energy laser injection onto a spherical target and the ablation plasma dynamics in a magnetic field.

3. To find the scaling law of the magnetic thrust chamber system, it is necessary to confirm the validity of the numerical simulation. In order to validate the modified numerical simulation with considering the creation process, the experimental results are compared with these of the numerical simulations which are with and without considering the creation process of a laser-produced plasma.

1.9 Table of contents

The structure of this thesis is as follows. Chapter 2 reviews the energy deposition of high power beams and the 1D Lagrangian radiation hydrodynamic code via the deposition. Chapter 3 describes the basic equations and the numerical algorithms used in the 3D hybrid PIC code. Chapter 4 is devoted to the direct measurement of impulse and the dependences of impulse on the laser parameters. Numerical simulations with and without considering the creation process of a laser-produced plasma are also performed to confirm the validity of the modified numerical simulation. In Chapter 5, the ion expansion velocity of a laser-produced plasma is described. Numerical

simulations are also performed to confirm the validity of the modified numerical simulation. In addition to these, the interaction between the initial plasma condition and magnetic field strength is investigated in Chapter 6. Finally, Chapter 7 contains conclusions and suggestions for the future work.

Bibliography

[1] JPL, "Mars Exploration Program," URL: `http://mars.jpl.nasa.gov` [cited 1 January 2013].

[2] JPL, "NASA Facts: Mars Pathfinder," *NASA Fact Sheet*, URL: `http://www.jpl.nasa.gov/news/fact_sheets/mpf.pdf` [cited 1 January 2013].

[3] JPL, "NASA Facts: Mars Exploration Rover," *NASA Fact Sheet*, URL: `http://marsrovers.jpl.nasa.gov/newsroom/factsheets/pdfs/Mars03Rover041020.pdf` [cited 1 January 2013].

[4] JPL, "NASA Facts: Mars Science Laboratory/Curiosity," *NASA Fact Sheet*, URL: `http://mars.jpl.nasa.gov/msl/news/pdfs/MSL_Fact_Sheet.pdf` [cited 1 January 2013].

[5] McCracken, G. M., and Stott, P. E., *Fusion: The Energy of the Universe*, 1st ed., Academic Press, Massachusetts, 2005, Chaps. 1 and 2.

[6] Atzeni, S., and Meyer-ter-Vehn, J., *The Physics of Inertial Fusion: Beam Plasma Interaction, Hydrodynamics, Hot Dense Matter*, Oxford University Press, London, 2004, Chap. 3.

[7] McCracken, G. M., and Stott, P. E., *Fusion: The Energy of the Universe*, 1st ed., Academic Press, Massachusetts, 2005, Chap. 7.

[8] McCracken, G. M., and Stott, P. E., *Fusion: The Energy of the Universe*, 1st ed., Academic Press, Massachusetts, 2005, Chap. 3.

[9] Long, K. F., *Deep Space Propulsion: A Roadmap to Interstellar Flight*, Springer, Berlin, 2012, Chap. 12.

[10] Dyson, F. J., "Interstellar Transport," *Physics Today*, October 1968, pp. 41-45. doi: 10.1063/1.3034534

[11] Project Daedalus Study Group and British Interplanetary Society, *Project Daedalus: The Final Report on the BIS Starship Study*, Space Educational Aids, London, 1978.

[12] Winterberg, F., "Rocket Propulsion by Thermonuclear Microbombs Ignited with Intense Relativistic Electron Beams," *Raumfahrtforschung*, Vol. 15, 1971, pp. 208-217.

[13] Balcomb, J. D., Booth, L. A., Cotter, T. P., Hedstrom, J. C., Robinson, C. P., Springer, T. E., Watson, C. W., "Nuclear Pulsed Space Propulsion Systems," Los Alamos Scientific Laboratory LA-4541-MS, 1970.

[14] Hyde, R. A., Wood, L. L., and Nuckolls, J. H., "Prospects for Rocket Propulsion with Laser-Induced Fusion Microexplosions," AIAA Paper 72-1063, 1972.

[15] Hyde, R. A., "A Laser Fusion Rocket for Interplanetary Propulsion," Lawrence Livermore National Laboratory UCRL-88857, 1983.

[16] Orth, C. D., Klein, G., Sercel, J., Hoffman, N., Murray, K., and Chang-Diaz, F., "Transport Vehicle for Manned Mars Missions Powered by Inertial Confinement Fusion," Lawrence Livermore National Laboratory UCRL-96832, 1987.

[17] Orth, C. D., "VISTA - A Vehicle for Interplanetary Space Transport Application Powered by Inertial Confinement Fusion," Lawrence Livermore National Laboratory UCRL-LR-110500, 2003.

[18] Vchivokv, K. V., Nakashima, H., Zakharov, Y. P., Esaki, T., Kawano, T., and Muranaka, T., "Laser-Produced Plasma Experiments and Particle in Cell Simulation to Study Thrust Conversion Processes in a Laser Fusion Rocket," *Jpn. J. Appl. Phys.*, Vol. 42, Issue 10, 2003, pp. 6590-6597. doi: 10.1143/JJAP.42.6590

[19] Sato, K., Okada, S., Kogoshi, S., Sudo, S., Tsuji, H., Ohwadano, Y., Sekiguchi, T., Katsurai, M. and Tanaka, H., "HIGH-TEMPERATURE HIGH-QUALITY DEUTERIUM PLASMA PRODUCTION BY LASER BEAM(S) AND INTERACTIONS WITH MAGNETIC FIELDS," Proceedings of the 6th International Conference on Plasma Physics and Controlled Nuclear Fusion Research, held by the International Atomic Energy Agency, at Berchtesgaden, 6-13 October 1976, Nuclear Fusion Supplement, Vol. 2, 1977, pp. 567-575.

[20] Nagamine, Y., and Nakashima, H., "Analysis of Plasma Behavior in a Magnetic Thrust Chamber of a Laser Fusion Rocket," *Fusion Science and Technology*, Vol. 35, Issue 1, 1999, pp. 62-70.

[21] Kawabuchi, R., Matsuda, N., Kajimura, Y., Nakashima, H., and Zakharov, Y. P., "Numerical Simulation of Plasma Detachment from a Magnetic Nozzle by using Fully Particle-In-Cell Code," *J. Phys. Conf. Ser.*, Vol. 112, Issue 4, 2008, pp. 1-4. doi: 10.1088/1742-6596/112/4/042082

[22] Kajimura, Y., Kawabuchi, R., and Nakashima, H., "Control Techniques of Thrust Vector for Magnetic Nozzle in Laser Fusion Rocket," *Fusion*

Engineering and Design, Vol. 81, Issues 23-24, 2006, pp. 2871-2875. doi: 10.1016/j.fusengdes.2006.07.046

Chapter 2

Laser-target interaction

2.1 Introduction

For creation of a laser-produced plasma, a fuel target is driven by external laser beams. The beams heat the target rapidly to high temperatures. The beam energy is transferred predominantly to electrons and electron plasma waves. Then, thermalization occurs due to Coulomb collisions between the electrons and the ions and a laser-produced plasma is created. Here, we describe the energy deposition of high power beams and a 1D Lagrangian radiation hydrodynamic code via the deposition. This code can compute the hydrodynamic evolution of radiating plasma heated by laser pulses.

2.2 Laser parameters

The important parameter that dominates the creation process of a laser-produced plasma is the critical density n_{c},

$$n_{\mathrm{c}} = \frac{4\pi^2 m_{\mathrm{e}}}{\mu e^2 \lambda_{\mathrm{L}}^2} \tag{2.1}$$

$$\lambda_{\mathrm{L}} = \frac{2\pi c}{\omega} \tag{2.2}$$

where m_{e} is the electron mass, μ is the magnetic permeability and e is the elementary charge. λ_{L} is the laser wavelength as follows, where c is the speed of light (i.e., $c^2 = 1/\mu\varepsilon$) and ω is the laser frequency. When the target is driven by a laser beam, the beam is reflected on the critical surface and cannot penetrate inside. The incident laser intensity, I_{L}, is defined as the laser power per unit area per one shot as shown in Fig. 2.1, and is given by

$$I_{\mathrm{L}} = \frac{E_{\mathrm{L}}}{\pi r_{\mathrm{spot}}^2 \cdot \tau_{\mathrm{L}}}$$

where E_{L} is the incident laser energy, r_{spot} is the radius of the laser beam spot and τ_{L} is the laser pulse duration, respectively.

2.3 Elements of plasma physics

2.3.1 Dielectric functions for transverse and longitudinal plasma waves

The absorption of external laser beams involves collective plasma effects. The theoretical study is based on Maxwell's equations and the linearized plasma equations, describing small perturbations in an uniform plasma. Equations (2.3) and (2.4) are Maxwell-Faraday equation and the equation for Ampere's law, respectively.

$$\nabla \times \boldsymbol{E} = -\frac{\partial \boldsymbol{B}}{\partial t} \tag{2.3}$$

$$\nabla \times \boldsymbol{B} = \mu \left(\boldsymbol{j} + \varepsilon \frac{\partial \boldsymbol{E}}{\partial t} \right) \tag{2.4}$$

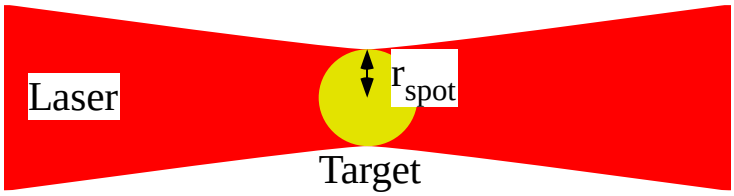

Figure 2.1: Target irradiated and focused by a single laser beam.

where $\boldsymbol{E}$ is the electric field, and $\boldsymbol{B}$ is the magnetic field, t is time and ε is the permeability. By substituting Eq. (2.3) into the time partial differential equation of Eq. (2.4), we obtain the following equation.

$$\nabla \times (\nabla \times \boldsymbol{E}) = -\mu \frac{\partial \boldsymbol{j}}{\partial t} - \frac{1}{c^2} \frac{\partial^2 \boldsymbol{E}}{\partial t^2} \tag{2.5}$$

Equation (2.5) describes the propagation of electromagnetic waves in a plasma. For the sake of conveniences, all perturbations are expressed in terms of their Fourier modes as shown below,

$$\boldsymbol{A} = \Re[\hat{A} \exp(-i\omega t + i\boldsymbol{k} \cdot \boldsymbol{r})]$$

where $\hat{A}$ is the complex magnitude and $\boldsymbol{r}$ is the position. Time and space derivatives are replaced by the frequency $-i\omega$ and the wave vector $i\boldsymbol{k}$, respectively. Then, Eq. (2.5) has the form by Fourier transformation (i.e., $\nabla = i\boldsymbol{k}, \partial/\partial t = -i\omega$), and the wave equation is

$$\begin{aligned} -\boldsymbol{k} \times (\boldsymbol{k} \times \boldsymbol{E}) &= i\mu\omega \boldsymbol{j} + \frac{\omega^2}{c^2} \boldsymbol{E} \\ &= \frac{\omega^2}{c^2} \varepsilon \boldsymbol{E} \end{aligned} \tag{2.6}$$

Here, from the Ohm's law $\boldsymbol{j} = \sigma \boldsymbol{E}$, the definition of dielectric tensor ε is

$$\varepsilon = 1 + i \frac{\mu c^2}{\omega} \sigma \tag{2.7}$$

where σ is the electrical conductivity tensor. For non-magnetized plasmas, the dielectric tensor has the only diagonal elements, ε_{T} for the two transverse directions ($\boldsymbol{E} \perp \boldsymbol{k}$) and ε_{L} for the longitudinal direction ($\boldsymbol{E} \parallel \boldsymbol{k}$; $\boldsymbol{k} \times \boldsymbol{E} = 0$). Consequently, Eq. (2.6) separates into a transverse part shown in Eq. (2.8) and a longitudinal part shown in Eq. (2.9) [1, 2].

$$|\boldsymbol{k}|^2 = \frac{\omega^2}{c^2}\varepsilon_{\mathrm{T}} \tag{2.8}$$

$$\varepsilon_{\mathrm{L}} = 0 \tag{2.9}$$

In the case of $\boldsymbol{k} \times (\boldsymbol{k} \times \boldsymbol{E}) = 0$, the plasma and displacement currents compensate each other. The dielectric functions ε_{T} and ε_{L} have to be determined from the plasma equations and they depend on the wave number $|\boldsymbol{k}|$ and ω for an isotropic plasma.

2.3.2 Transverse electromagnetic waves

In the lowest linear order, when the ion is assumed to be static, the electromagnetic waves induce a transverse perturbation in the plasma electrons. This is described by Newton's equation for the electron velocity $\boldsymbol{v}_{\mathrm{e}}$ and Fourier transformation.

$$m_{\mathrm{e}}\frac{\mathrm{d}\boldsymbol{v}_{\mathrm{e}}}{\mathrm{d}t} = -i\omega m_{\mathrm{e}}\boldsymbol{v}_{\mathrm{e}} = -e\boldsymbol{E} - m_{\mathrm{e}}\nu_{\mathrm{ei}}\boldsymbol{v}_{\mathrm{e}} \tag{2.10}$$

Equation (2.10) includes electron-ion collisions, where ν_{ei} is the electron-ion collision frequency. The friction term ($\propto \nu_{\mathrm{ei}}$) is essential for collisional absorption. The electron velocity is given by Eq. (2.10).

$$\boldsymbol{v}_{\mathrm{e}} = -\frac{e\boldsymbol{E}}{m_{\mathrm{e}}(\nu_{\mathrm{ei}} - i\omega)} \tag{2.11}$$

From Eq. (2.11), the transverse current density is obtained.

$$\boldsymbol{j} = -n_{\mathrm{e}}e\boldsymbol{v}_{\mathrm{e}} = \frac{n_{\mathrm{e}}e^2}{m_{\mathrm{e}}(\nu_{\mathrm{ei}} - i\omega)}\boldsymbol{E} = \sigma\boldsymbol{E} \tag{2.12}$$

and from Eqs. (2.7) and (2.12), the transverse dielectric function is given by

$$\sigma = \frac{i\omega_{\mathrm{pe}}^2 \varepsilon}{\omega + i\nu_{\mathrm{ei}}}$$

$$\omega_{\mathrm{pe}}^2 = \frac{n_{\mathrm{e}} e^2}{\varepsilon m_{\mathrm{e}}}$$

$$\varepsilon_{\mathrm{T}} = 1 - \frac{\omega_{\mathrm{pe}}^2}{\omega(\omega + i\nu_{\mathrm{ei}})} \tag{2.13}$$

where ω_{pe} is the electron plasma frequency and n_{e} is the electron density. The imaginary term in Eq. (2.13) leads to damping of the electromagnetic wave. Replacing $\boldsymbol{k}$ by $k + iK_{\mathrm{a}}/2$, the incident laser intensity becomes $I_{\mathrm{L}} \propto |\boldsymbol{E}|^2 \propto \exp(-K_{\mathrm{a}}\boldsymbol{r})$, where K_{a} is the absorption coefficient. By inserting Eq. (2.13) into Eq. (2.8), the dispersion equation is given as Eq. (2.14). From the real part of Eq. (2.14), the dispersion relation for the electromagnetic waves, Eq. (2.15), is obtained. The coefficient for collisional absorption, Eq. (2.16) is obtained from the imaginary part of the dispersion equation [1, 2].

$$|\boldsymbol{k}|^2 \left(\frac{c}{\omega}\right)^2 = 1 - \left(\frac{\omega_{\mathrm{pe}}}{\omega}\right)^2 \frac{\omega}{\omega + i\nu_{\mathrm{ei}}} \tag{2.14}$$

Here, we assumed $\omega \gg \nu_{\mathrm{ei}}$. The group velocity v_{g} is the speed of the overall shape of the wave's amplitude propagation through the space.

$$k = \frac{\omega}{c}\sqrt{1 - \left(\frac{\omega_{\mathrm{pe}}}{\omega}\right)^2} \tag{2.15}$$

$$K_{\mathrm{a}} = \frac{\nu_{\mathrm{ei}}}{v_{\mathrm{g}}} \left(\frac{\omega_{\mathrm{pe}}}{\omega}\right)^2 \tag{2.16}$$

$$v_{\mathrm{g}} = \frac{\partial \omega}{\partial k} = c\sqrt{1 - \left(\frac{\omega_{\mathrm{pe}}}{\omega}\right)^2} \tag{2.17}$$

2.4 Collisional absorption of laser light in laser-produced plasma

2.4.1 Scaling with wavelength and incident intensity

When $\omega_{\rm pe}$ is larger than ω, Eq. (2.15) is not valid. This means that the laser beam is reflected on the critical surface defined from the relation $\omega_{\rm pe}^2/\omega^2 = n_{\rm e}/n_{\rm c}$. The beam is not propagating inside, as shown in Fig. 2.2. Here, $\omega^2 = n_{\rm c}e^2/\varepsilon m_{\rm e}$ is obtained by substituting Eq. (2.2) into Eq. (2.1). For driving matters with laser beams, the collisional absorption of the light in the ablation plasma is the dominant absorption mechanism, and it is called inverse-bremsstrahlung [3]. Other mechanisms such as resonance and parametric absorptions are not considered because they mostly convert the light energy to the energy of the plasma waves and produce superthermal electrons. In general, such mechanisms do not cause local thermalization on the critical surface. However, the deposited energy by the inverse-bremsstrahlung does local thermalization. The light can travel through the ablation plasma up to the critical surface. For sufficiently small wavelengths, this collisional absorption is considered to be the dominant process and assumed to be about 1, since the critical density strongly depends on the laser wavelength as seen in Eq. (2.1).

2.4.2 Absorption coefficient

The coefficient of the collisional absorption [4, 5], given by Eq. (2.16), may be rewritten in the following form by using $\omega_{\rm pe}^2/\omega^2 = n_{\rm e}/n_{\rm c}$,

$$K_{\rm a} = \frac{\nu_{\rm ei}}{v_{\rm g}} \left(\frac{n_{\rm e}}{n_{\rm c}}\right)^2$$
$$= \frac{1}{v_{\rm g}} \frac{4\sqrt{2m_{\rm e}}\pi^{3/2}c^2e^2Z^* \ln\Lambda_{\rm ei}}{3\lambda_{\rm L}^2(k_{\rm B}T_{\rm e})^{3/2}} \left(\frac{n_{\rm e}}{n_{\rm c}}\right)^2 \quad (2.18)$$

where Z is the charge state of ion, $\ln\Lambda_{\rm ei}$ is the Coulomb logarithm [6] for electron-ion collisions, $k_{\rm B}$ is the Boltzmann constant and $T_{\rm e}$ is the electron temperature, respectively. Z^* is defined as $< Z^2 > / < Z >$, where $<>$ indicates averaging over the ion species. The collisional frequency, $\nu_{\rm ei}$, on the critical surface is taken from the Spitzer relaxation time [7],

$$\nu_{\rm ei} = \frac{8\sqrt{2\pi m_{\rm e}}e^4 n_{\rm i} < Z^2 > \ln\Lambda_{\rm ei}}{3m_{\rm i}(k_{\rm B}T_{\rm e})^{3/2}} \quad (2.19)$$

where $n_{\rm i}$ is the ion density and $m_{\rm i}$ is the ion mass.

2.4.3 Model for collisional absorption

The total fraction of the collisional absorption of the laser light on its path to the critical surface and the backward path after reflection is determined from the Lambert-Beer law $\mathrm{d}I_{\rm L}/\mathrm{d}x = -K_{\rm a}I_{\rm L}$ as shown in Fig. 2.2.

$$\eta_{\rm a} = 1 - \exp\left(-2\int_0^L K_{\rm a}\mathrm{d}x\right) \quad (2.20)$$

2.4.4 Dependence of absorption on wavelength

The most outstanding feature of the collisional absorption is the strong dependence on wavelength, since the laser beam is reflected on the critical surface. When the wavelength becomes a half, the critical density becomes four times larger as seen from Eq. (2.1). Thus, the short wavelength light can penetrate deeper, and enhance the collisional absorption given in Eq.

(2.18). Finally, the deposited energy in the low density region is transported to the high density plasma and continues creating ablation plasma on the ablation surface, as shown in Fig. 2.3.

2.5 1D Lagrangian radiation hydrodynamic code

2.5.1 Hydrodynamic equations

A 1D Lagrangian radiation hydrodynamic code [8, 9, 10, 11] named Star-1D was developed by Sunahara [12, 13]. Star-1D is able to compute the hydrodynamic evolution of radiating plasma heated by laser pulses. It employs a one-fluid, two-temperature ($T_\mathrm{i} \neq T_\mathrm{e}$) model, as shown in Fig. 2.3, where T_i is the ion temperature. The plasma is assumed to be quasi-neutral due to co-moving electrons (i.e., $Zn_\mathrm{i} = n_\mathrm{e}$). We solve the following equations.

Equation (2.21) is the equation of continuity, where ρ is the mass density and $\boldsymbol{v}$ is the fluid velocity. Equation (2.22) is the equation of motion in planar and spherical geometries in which the artificial viscosity q smoothens the shock front. p_s is the pressure. Here, the subscript s indicates either an ion (i) or an electron (e).

$$\frac{\mathrm{d}\rho}{\mathrm{d}t} + \rho\nabla\cdot\boldsymbol{v} = 0 \tag{2.21}$$

$$\frac{\mathrm{d}\boldsymbol{v}}{\mathrm{d}t} = -\frac{1}{\rho}\nabla(p_\mathrm{i} + p_\mathrm{e} + q) \tag{2.22}$$

Equations (2.23) and (2.24) are the energy equations for ions and electrons, where $c_{\mathrm{V}\mathrm{s}}$ is the specific heat, κ_s the thermal conductivity and α the thermal relaxation coefficient, respectively.

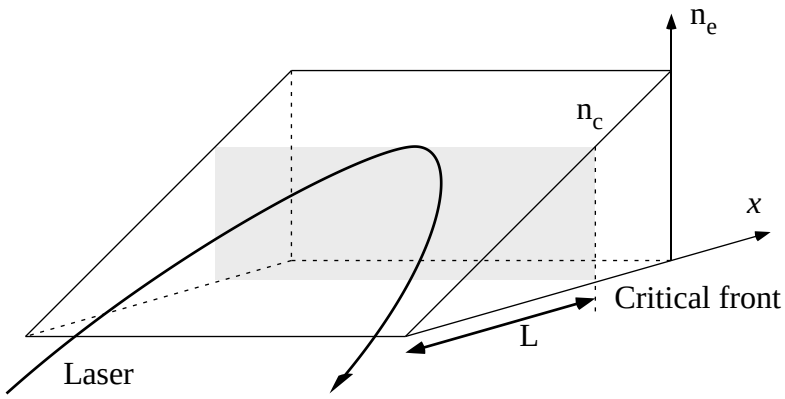

Figure 2.2: Normal incidence of the laser light on planar ablation plasma.

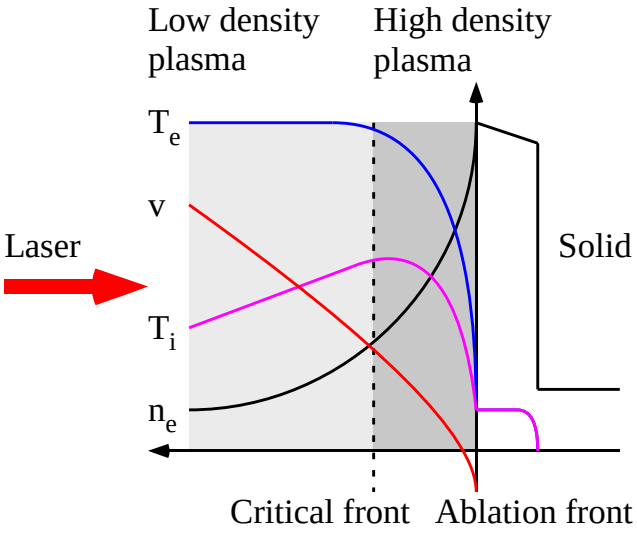

Figure 2.3: Ion and electron temperature, ablation plasma velocity and electron density distributions in a laser-produced plasma.

$$\rho c_{\mathrm{Vi}} \frac{\mathrm{d}T_{\mathrm{i}}}{\mathrm{d}t} = -p_{\mathrm{THi}} \nabla \cdot \boldsymbol{v} + \nabla \cdot (\kappa_{\mathrm{i}} \nabla T_{\mathrm{i}}) + \alpha (T_{\mathrm{e}} - T_{\mathrm{i}}) + Q_{\mathrm{i}} \tag{2.23}$$

$$\rho c_{\mathrm{Ve}} \frac{\mathrm{d}T_{\mathrm{e}}}{\mathrm{d}t} = -p_{\mathrm{THe}} \nabla \cdot \boldsymbol{v} + \nabla \cdot (\kappa_{\mathrm{e}} \nabla T_{\mathrm{e}}) - \alpha (T_{\mathrm{e}} - T_{\mathrm{i}}) + Q_{\mathrm{e}} \tag{2.24}$$

$$p_{\mathrm{THs}} = T_{\mathrm{s}} \left(\frac{\partial p_{\mathrm{s}}}{\partial T_{\mathrm{s}}} \right)_{\rho} \tag{2.25}$$

In Eqs. (2.22)-(2.25), the variables p_{s}, c_{Vs}, and p_{THs} are functions of n_{i} and T_{s}. They are obtained from the SESAME equation of state tables [14] based on the local thermodynamic equilibrium (LTE) model. The second terms on the right-hand sides of Eqs. (2.23) and (2.24) represent the thermal conduction due to ions [15] and electrons [16, 17], as shown in Eq. (2.26).

$$\begin{aligned} \kappa_{\mathrm{i}} &= \frac{2.925 (k_{\mathrm{B}} T_{\mathrm{i}})^{5/2}}{\sqrt{\pi m_{\mathrm{i}}} e^4 < Z^2 >^2 \ln \Lambda_{\mathrm{ii}}} \\ \kappa_{\mathrm{e}} &= \frac{16 \sqrt{2} (k_{\mathrm{B}} T_{\mathrm{e}})^{5/2}}{\phi \pi^{5/2} \sqrt{m_{\mathrm{e}}} e^4 Z^* \ln \Lambda_{\mathrm{ei}}}, \qquad \phi = \frac{Z^* + 4.2}{Z^* + 0.24} \end{aligned} \tag{2.26}$$

We used the flux-limited Spitzer-Härm model [18] (with a flux limit factor of 0.1 [19]) . The third terms in Eqs. (2.23) and (2.24) indicate the electron-ion temperature relaxation, and $\alpha (= 1.5 k_{\mathrm{B}} n_{\mathrm{e}} \nu_{\mathrm{ei}} / f)$ is determined. f is the reduction factor of the laser absorption due to the Langdon effect [20], which is important for long wavelength laser irradiation. $Q_{\mathrm{i}} (= -q \nabla \cdot \boldsymbol{v})$ is the viscous heat, generated by conversion of the kinetic energy to the ion thermal energy, due to the viscosity. Q_{e} represents a laser energy absorption for electrons and radiation. The laser energy deposited between the vacuum plasma boundary (the expansion surface) and the critical surface is calculated by ray tracing using 100 rays. We assumed the inverse bremsstrahlung to occur in the laser energy absorption process. The calculated deposition at each calculation mesh is $P \propto \exp(-v_{\mathrm{g}} K_{\mathrm{a}} \Delta t)$, where P is the local laser

power, and Δt is the time required for the laser ray to pass through each mesh size at its group velocity.

2.5.2 Radiative transport equations

Equation (2.27) is the radiative transport equation, where E_ν is the photon energy density for ν, D_ν the diffusion coefficient for ν, η_ν the emissivity for ν, χ_ν the absorption coefficient for ν, and ν the frequency group, respectively. Here, the emissivity and the opacity have [W/m^3/second/dν/steradian] and [1/m] in SI-unit, respectively. To study the radiation transport process, the multi-group diffusion approximation model [21] using a flux limit as shown in Eq. (2.28) is applied. The photon energy $h\nu$ is in the range of 0-1 keV, and the range is divided into 100 bins for ν to solve Eq. (2.27) numerically. h is the Planck constant. $h\nu$ and the opacity $\kappa_\nu (= \chi_\nu/\rho)$ are evaluated using the collisional radiative equilibrium (CRE) model. In CRE model, the plasma is assumed to be optically thin: plasma does not reabsorb its radiation energy.

$$\rho \frac{\mathrm{d}}{\mathrm{d}t}\left(\frac{E_\nu}{\rho}\right) + \nabla \cdot (D_\nu \nabla E_\nu) = 4\pi\eta_\nu - c\chi_\nu E_\nu \tag{2.27}$$

$$D_\nu = -\frac{c}{3\chi_\nu + |\nabla E_\nu|/E_\nu} \tag{2.28}$$

2.6 Summary

In this Chapter, we described the energy deposition of high power beams and a 1D Lagrangian radiation hydrodynamic code (named Star-1D) which can compute the hydrodynamic evolution of radiating plasma heated by laser pulses.

In the modified numerical simulation computing high energy laser injection onto a spherical target and the ablation plasma dynamics in a magnetic

field, the results of Star-1D are used as 3D distributions of ion super particle for the particle position, expansion velocity, charge state and mass. They are inputted into a 3D hybrid PIC code. To convert from a 1D Lagrangian mesh model to a 3D Cartesian coordinate particle model, the plasma is assumed to expand into the vacuum isotropically as the 1D meshes are elements along the radius of multi-layer sphere. Since the number of ions in each shell is calculated by multiplying the shell volume by the ion density, it is easy that to divide the ion super particles into each shell. Finally, the physical quantities of the 1D meshes are distributed among the ion super particles.

Bibliography

[1] Dawson, J. M., and Oberman, C. R., "High-Frequency Conductivity and the Emission and Absorption Coefficients of a Fully Ionized Plasma," *Phys. Fluids*, Vol. 5, Issue 5, 1962, pp. 517-524. doi: 10.1063/1.1706652

[2] Atzeni, S., and Meyer-ter-Vehn, J., *The Physics of Inertial Fusion: Beam Plasma Interaction, Hydrodynamics, Hot Dense Matter*, Oxford University Press, London, 2004, Chap. 11.

[3] Kruer, W. L., *The Physics of Laser Plasma Interactions*, Westview Press, Colorado, 2003, pp. 45-56.

[4] Shearer, J. W., "Effect of Oblique Incidence on Optical Absorption of Laser Light by a Plasma," *Phys. Fluids*, Vol. 14, Issue 1, 1970, pp. 183-185. doi: 10.1063/1.1693272

[5] Johnston, T. W., and Dawson, J. M., "Correct Values for High-Frequency Power Absorption by Inverse Bremsstrahlung in Plasmas" *Phys. Fluids*, Vol. 16, Issue 5, 1973, pp. 722. doi: 10.1063/1.1694419

[6] Skupsky, S., "Coulomb Logarithm for Inverse-Bremsstrahlung Laser Absorption," *Phys. Rev. A*, Vol. 36, Issue 12, 1987, pp. 5701-5712. doi: 10.1103/PhysRevA.36.5701

[7] Spitzer Jr., L., *Physics of Fully Ionized Gases*, 2nd ed., Dover Publications, New York, 2006, pp. 131-136.

[8] Sizyuk, V., Hassanein, A., Morozov, V., Tolkach, V., Sizyuk, T., and Rice, B., "Numerical Simulation of Laser-Produced Plasma Devices for EUV Lithography Using the Heights Integrated Model," *Numer. Heat Transfer Part A Appl.*, Vol. 49, Issue 3, 2006, pp. 215-236. doi: 10.1080/10407780500324996

[9] MacFarlane, J. J., Golovkin, I. E., and Woodruff, P. R., "HELIOS-CR: A 1-D Radiation-Magnetohydrodynamics Code with Inline Atomic Kinetics Modeling," *J. Quant. Spectrosc. Radiat. Transfer*, Vol. 99, Issue 1-3, 2006, pp. 381-397. doi: 10.1016/j.jqsrt.2005.05.031

[10] Nagatomo, H., "Computational Simulation for Laser Driven Implosion," *J. Plasma Fusion Res.*, Vol. 81, 2005, pp. 59-63. [In Japanese]

[11] Ohnishi, N., "Fundamentals of Radiation Hydrodynamics Simulation," *J. Plasma Fusion Res.*, Vol. 88, Issue 9, 2012, pp. 467-474. [In Japanese]

[12] Sunahara, A., Nishihara, K., and Sasaki, A., "Optimization of Extreme Ultraviolet Emission from Laser-Produced Tin Plasmas Based on Radiation Hydrodynamics Simulations," *Plasma and Fusion Res.*, Vol. 3, Issue 43, 2008, pp. 1-5. doi: 10.1585/pfr.3.043

[13] Sunahara, A., Sasaki A., Tanuma, H., Nishihara, K., Nishikawa, T., Koike, F., Fujioka, S., Aota, T., Yamamura, M., Shimada, Y., Nishimura, H., Izawa, Y., Miyanaga, N., and Mima, K., "Radiation Hydrodynamic Simulation of Extreme Ultra-Violet Emission from Laser-Produced Tin Plasmas," *J. Plasma Fusion Res.*, Vol. 83, Issue 11, 2007, pp. 920-926. [In Japanese]

[14] Lyon, S. P., and Johnson, J. D., "SESAME: The Los Alamos National Laboratory Equation of State. Database," Los Alamos National Laboratory LA-UR-92-3407, 1992.

[15] Braginskii, S. I., "Transport Processes in a Plasma," *Rev. Plasma Phys.*, Vol. 1, Consultants Bureau, New York, 1965, pp. 250.

[16] Spitzer Jr., L., and Härm, R., "Transport Phenomena in a Completely Ionized Gas," *Phys. Rev.*, Vol. 89, Issue 5, 1953, pp. 977-981. doi: 10.1103/PhysRev.89.977

[17] Lee, Y. T., and More, R. M., "An Electron Conductivity Model for Dense Plasmas," *Phys. Fluids*, Vol. 27, Issue 5, 1984, pp. 1273-1286. doi: 10.1063/1.864744

[18] Malone, R. C., McCrory, R. L., and Morse, R. L., "Indications of Strongly Flux-Limited Electron Thermal Conduction in Laser-Target Experiments," *Phys. Rev. Lett.*, Vol. 34, 1975, pp. 721-724. doi: 10.1103/PhysRevLett.34.721

[19] Azechi, H., "Concept of Laser Fusion.," *J. Plasma Fusion Res.*, Vol. 81, 2005, pp. 2-10. [in Japanese].

[20] Langdon, A. B., "Nonlinear Inverse Bremsstrahlung and Heated-Electron Distributions," *Phys. Rev. Lett.*, Vol. 44, Issue 9, 1980, pp. 575-579. doi: 10.1103/PhysRevLett.44.575

[21] Minerbo, G. N., "Maximum Entropy Eddington Factors," *J. Quant. Spectrosc. Radiat. Transfer*, Vol. 20, Issue 16, 1978, pp. 541-545. doi: 10.1016/0022-4073(78)90024-9

Chapter 3

3D Hybrid PIC Code

3.1 Introduction

The 3D hybrid PIC code used in the present study for simulating the behavior of charged particles in a magnetic field is based on the model proposed by Horowitz [1]. Ions and electrons are treated as individual super particles and a magnetic hydrodynamic fluid, respectively. This approach is valid when the system is dominated by ion dynamics [2, 3, 4, 5]. The motion of an ion is solved self-consistently, that is, ions affect electromagnetic field in a 3D Cartesian coordinates and move in the field. In addition, this code has some assumptions about ions, electrons and the field. The mass of electron is assumed to be zero (i.e., m_{e}=0) to eliminate the kinetic electron effect such as electron plasma oscillation and cyclotron motion. The plasma is also assumed to be quasi-neutrality due to co-moving electrons (i.e., $Zn_{\mathrm{i}} = n_{\mathrm{e}}$). Z, n_{i} and n_{e} is charge state of ion, ion density and electron density, respectively. In order to combine this code with Star-1D, this code was improved to treat 3D distributions of ion super particle for the charge state and mass in addition to the particle position and expansion velocity. The results of Star-1D are inputted into the 3D hybrid PIC code. Here, we describe the

basic equations and the numerical algorithms used in this code.

3.2 Particles in electromagnetic field

3.2.1 PIC algorithm

In this code, the electromagnetic field is only calculated on the discrete rectangular grid points as shown in Fig. 3.1. • and ∘ indicate a particle and grid points, respectively. The field is linearly interpolated to the continuous particle positions for giving the correct ion acceleration. After the ions are moved, the ion density and ion current density redeposit to the eight nearest grid points. The algorithm to avoid a self-force (i.e., a particle accelerates itself.) is PIC algorithm [6, 7] by using the same weighting in both density and field calculations. The first-order weighting of Eq. (3.1) reduces high frequency noise and smooths the density and field variation, where V is the cell volume and V_n is the assignment volume. Equation (3.2) solves physical component ϕ at the particle position by using the triangle weighting.

$$\delta V_n = \frac{V_n}{V} \tag{3.1}$$

$$V = \sum_{1}^{8} V_n$$

$$\begin{aligned}\phi =& \phi_{i+1,j,k} \times \delta V_1 + \phi_{i,j,k} \times \delta V_2 \\ &+ \phi_{i+1,j+1,k} \times \delta V_3 + \phi_{i,j+1,k} \times \delta V_4 \\ &+ \phi_{i+1,j,k+1} \times \delta V_5 + \phi_{i,j,k+1} \times \delta V_6 \\ &+ \phi_{i+1,j+1,k+1} \times \delta V_7 + \phi_{i,j+1,k+1} \times \delta V_8\end{aligned} \tag{3.2}$$

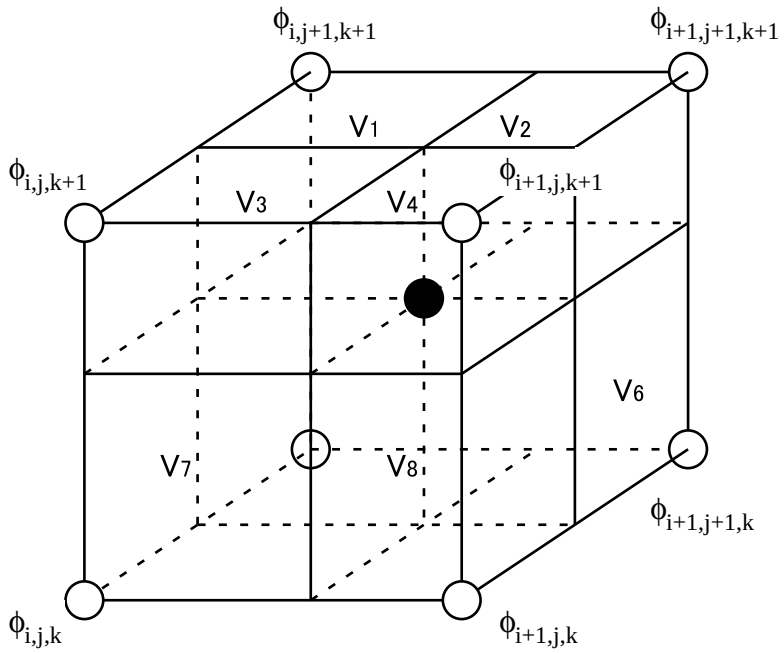

Figure 3.1: Particle and eight nearest grid points. • and ∘ shows particle and grid point, respectively.

3.2.2 Digital filter

The digital filter [8] improves overall accuracy and reduces the noise by ignoring source terms at short wavelengths. The phenomena of high frequency plasma are also neglected. The filter is limited to operate the eighteen nearest grid points as shown in Fig. 3.2. This filter is designated by the values (M, S, K), where M=middle, S=side and K=corner weights, as shown in Eqs. (3.3), (3.4) and (3.5). New physical component $\phi^{\text{new}}_{i,j,k}$ is obtained Eq. (3.6) given by substituting a binomial eighteen-points filter (12, 4, 1) into Eq. (3.3).

$$\phi^{\text{new}}_{i,j,k} \leftarrow \frac{M\phi_{i,j,k} + S\phi^{\text{side}}_{i,j,k} + K\phi^{\text{corner}}_{i,j,k}}{M + 6S + 12K} \tag{3.3}$$

$$\phi^{\text{side}}_{i,j,k} = \phi_{i-1,j,k} + \phi_{i+1,j,k} + \phi_{i,j-1,k} + \phi_{i,j+1,k} + \phi_{i,j,k-1} + \phi_{i,j,k+1} \tag{3.4}$$

$$\begin{aligned}\phi^{\text{corner}}_{i,j,k} = {} & \phi_{i,j-1,k-1} + \phi_{i,j+1,k-1} + \phi_{i,j-1,k+1} + \phi_{i,j+1,k+1} + \phi_{i-1,j,k-1} + \phi_{i+1,j,k-1} \\ & + \phi_{i-1,j,k+1} + \phi_{i+1,j,k+1} + \phi_{i-1,j-1,k} + \phi_{i+1,j-1,k} + \phi_{i-1,j+1,k} + \phi_{i+1,j+1,k}\end{aligned} \tag{3.5}$$

$$\phi^{\text{new}}_{i,j,k} = \frac{1}{4}\phi_{i,j,k} + \frac{1}{12}\phi^{\text{side}}_{i,j,k} + \frac{1}{48}\phi^{\text{corner}}_{i,j,k} \tag{3.6}$$

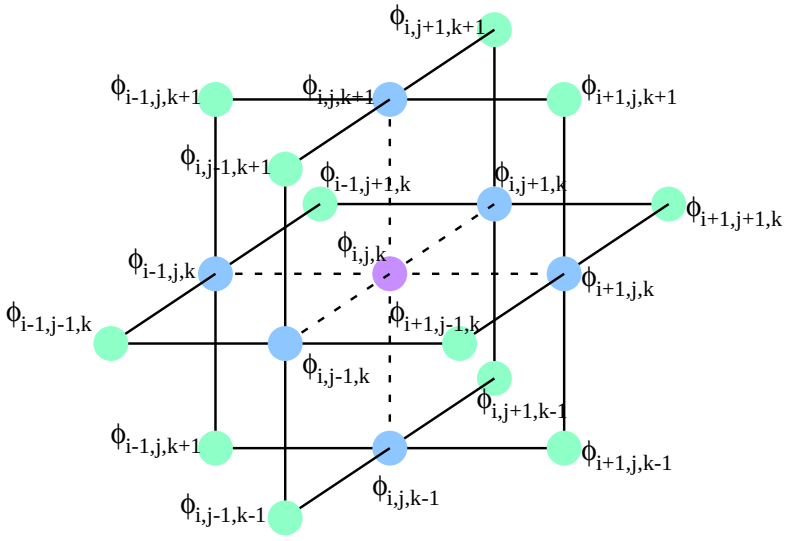

Figure 3.2: Eighteen nearest grid points. The points indicate middle, side and corner points.

3.3 Basic equations

The basic equations of this code are given below, where m_i is the ion mass, $\boldsymbol{v}_\mathrm{i}$ is the ion velocity, t is time, e is the elementary charge, $\boldsymbol{E}$ is the electric field, $\boldsymbol{B}$ is the magnetic field, $\boldsymbol{v}_\mathrm{e}$ is the electron velocity and p_e is the electron pressure, respectively.

$$n_\mathrm{i} m_\mathrm{i} \frac{\mathrm{d}\boldsymbol{v}_\mathrm{i}}{\mathrm{d}t} = Z e n_\mathrm{i}(\boldsymbol{E} + \boldsymbol{v}_\mathrm{i} \times \boldsymbol{B}) - \boldsymbol{R} \tag{3.7}$$

$$\frac{\mathrm{d}\boldsymbol{x}}{\mathrm{d}t} = \boldsymbol{v}_\mathrm{i}$$

$$n_\mathrm{e} m_\mathrm{e} \frac{\mathrm{d}\boldsymbol{v}_\mathrm{e}}{\mathrm{d}t} = 0 = -e n_\mathrm{e}(\boldsymbol{E} + \boldsymbol{v}_\mathrm{e} \times \boldsymbol{B}) + \boldsymbol{R} - \nabla p_\mathrm{e} \tag{3.8}$$

Equations (3.7) and (3.8) are the equations for particle and inertia-less fluid motion, respectively. The term $\boldsymbol{R}$ on the equations is friction term for the momentum of electron colliding with ion [9, 10]. This term solves magnetic field diffusion on the boundary between plasma and magnetic field and is given by

$$\begin{aligned} \boldsymbol{R} &= n_\mathrm{e} m_\mathrm{e}(\boldsymbol{v}_\mathrm{i} - \boldsymbol{v}_\mathrm{e})\nu_\mathrm{ei} \\ &= n_\mathrm{e}\eta e(\boldsymbol{j}_\mathrm{i} - e n_\mathrm{e}\boldsymbol{v}_\mathrm{e}) \end{aligned} \tag{3.9}$$

where ν_ei is the electron-ion collision frequency and $\boldsymbol{j}_\mathrm{i}(= Z e n_\mathrm{i}\boldsymbol{v}_\mathrm{i})$ is the ion current density. The resistivity η is usually taken as a scalar with a constant coefficient $m_\mathrm{e}\nu_\mathrm{ei}/n_\mathrm{e}e^2$ and is a parameter depending on the electron-ion collision frequency. The third term on Eq. (3.8) is the relationship between the pressure and the temperature. Because this relationship is assumed to be an isothermal or adiabatic while plasma expands, the electron temperature is assumed to be uniform for simplicity. ∇p_e is given by

$$\begin{aligned}\nabla p_{\mathrm{e}} &= \nabla\left(n_{\mathrm{e}} k_{\mathrm{B}} T_{\mathrm{e}}\right) \\ &= n_{\mathrm{e}} \nabla k_{\mathrm{B}} T_{\mathrm{e}} + k_{\mathrm{B}} T_{\mathrm{e}} \nabla n_{\mathrm{e}} \\ &= k_{\mathrm{B}} T_{\mathrm{e}} \nabla n_{\mathrm{e}} \end{aligned} \tag{3.10}$$

where k_{B} is the Boltzmann constant and T_{e} is the electron temperature. By substituting Eqs. (3.9) and (3.10) into Eq. (3.8), we obtain the following equation, where $\boldsymbol{j}(=\boldsymbol{j}_{\mathrm{i}}+\boldsymbol{j}_{\mathrm{e}})$ is the current density and $\boldsymbol{j}_{\mathrm{e}}(=-en_{\mathrm{e}}\boldsymbol{v}_{\mathrm{e}})$ is the electron current density.

$$0 = -en_{\mathrm{e}}(\boldsymbol{E} + \boldsymbol{v}_{\mathrm{e}} \times \boldsymbol{B} - \eta \boldsymbol{j}) - k_{\mathrm{B}} T_{\mathrm{e}} \nabla n_e \tag{3.11}$$

Ampere's law with Darwin approximation (See Appendix A) of Eq. (3.12) neglects the effects of high frequency phenomena such as electromagnetic radiation and waves associated with electron inertia, that is, the electromagnetic field is treated in the low frequency approximation. The electron velocity is expressed as follows, where μ_0 is the permeability of vacuum.

$$\begin{aligned}\nabla \times \boldsymbol{B} &= \mu_0 \boldsymbol{j} \qquad (3.12) \\ &= \mu_0(\boldsymbol{j}_{\mathrm{i}} - en_{\mathrm{e}}\boldsymbol{v}_{\mathrm{e}}) \\ \boldsymbol{v}_{\mathrm{e}} &= \frac{1}{en_{\mathrm{e}}}\left(\boldsymbol{j}_{\mathrm{i}} - \frac{\nabla \times \boldsymbol{B}}{\mu_0}\right) \qquad (3.13)\end{aligned}$$

The electric field in the plasma region is computed by substituting Eq. (3.13) into Eq. (3.11).

$$0 = en_{\mathrm{e}} \left\{ \boldsymbol{E} + \frac{1}{en_{\mathrm{e}}} \left(\boldsymbol{j}_{\mathrm{i}} - \frac{\nabla \times \boldsymbol{B}}{\mu_0} \right) \times \boldsymbol{B} - \eta \boldsymbol{j} \right\} + k_{\mathrm{B}} T_{\mathrm{e}} \nabla n_{\mathrm{e}}$$

$$\begin{aligned} \boldsymbol{E} &= -\frac{1}{Zen_{\mathrm{i}}} \left\{ \left(\boldsymbol{j}_{\mathrm{i}} - \frac{\nabla \times \boldsymbol{B}}{\mu_0} \right) \times \boldsymbol{B} + k_{\mathrm{B}} T_{\mathrm{e}} Z \nabla n_{\mathrm{i}} \right\} + \eta \boldsymbol{j} \\ &= -\frac{1}{Zen_{\mathrm{i}}} \left\{ \left(\boldsymbol{j}_{\mathrm{i}} - \frac{\nabla \times \boldsymbol{B}}{\mu_0} \right) \times \boldsymbol{B} + k_{\mathrm{B}} T_{\mathrm{e}} Z \nabla n_{\mathrm{i}} \right\} + \frac{\eta}{\mu_0} \nabla \times \boldsymbol{B} \end{aligned} \tag{3.14}$$

The partial differential equation for the time development of the magnetic field is advanced by Eq. (3.14), Maxwell-Faraday's law of Eq. (3.15) and the vector triple product of magnetic field (i.e., $\nabla \times (\nabla \times \boldsymbol{B}) = -\nabla^2 \boldsymbol{B} + \nabla(\nabla \cdot \boldsymbol{B})$).

$$\nabla \times \boldsymbol{E} = -\frac{\partial \boldsymbol{B}}{\partial t} \tag{3.15}$$

$$\frac{\partial \boldsymbol{B}}{\partial t} = \frac{1}{Zen_{\mathrm{i}}} \nabla \times \left\{ \left(\boldsymbol{j}_{\mathrm{i}} - \frac{\nabla \times \boldsymbol{B}}{\mu_0} \right) \times \boldsymbol{B} + k_{\mathrm{B}} T_{\mathrm{e}} Z \nabla n_{\mathrm{i}} \right\} + \frac{\eta}{\mu_0} \nabla^2 \boldsymbol{B} \tag{3.16}$$

After the advance of magnetic field is solved, the electric field can be solved. Then, the motion of ion is simulated by using leapfrog algorithm. Here, η and T_{e} is assumed to be zero for simplicity.

3.4 Leapfrog algorithm

The time integration scheme for solving partial differential equation is followed by the second-order leapfrog algorithm. The updates in time are relatively straightforward. The calculation steps at the time step n (denoted by the superscript) are as follows. Figure 3.3 indicates the initial step (1, 2, 3, 4) and the cycle steps (5, 6, 7) of leapfrog algorithm. (The components of ion velocity and electric field are indicated in Appendix B.) The time step Δt is according to the Courant Friedrichs Lewy (CFL) condition as the speed of light is replaced by the Alfven speed, since hybrid PIC code uses the implicit method not the explicit method.

3.4.1 Initial steps

1. $\boldsymbol{x}^0$, $\boldsymbol{v}_\mathrm{i}^0$, Z and m_i of each particle are inputted, where $\boldsymbol{x}$ is the particle position. $\boldsymbol{B}^0$ of each grid points is also inputted to this 3D hybrid PIC code. PIC algorithm interpolates n_i^0, $\boldsymbol{j}_\mathrm{i}^0$, Z^0 and m_i^0 for each grid point from $\boldsymbol{x}^0$ and $\boldsymbol{v}_\mathrm{i}^0$. For calculating electromagnetic field, the grid points in the calculation region are divided to the plasma and vacuum region. (○ in Fig. 3.3.)

2. Since n_i^0, $\boldsymbol{j}_\mathrm{i}^0$, Z^0 and $\boldsymbol{B}^0$ are known, $\boldsymbol{E}^0$ is obtained by using Eq. (3.17) given from Eq. (3.14). (● in Fig. 3.3.)

$$\boldsymbol{E}^n = -\frac{1}{Z^n e n_\mathrm{i}^n}\left\{\left(\boldsymbol{j}_\mathrm{i}^n - \frac{\nabla\times\boldsymbol{B}^n}{\mu_0}\right)\times\boldsymbol{B}^n + k_\mathrm{B}T_\mathrm{e}Z^n\nabla n_\mathrm{i}^n\right\} + \frac{\eta}{\mu_0}\nabla\times\boldsymbol{B}^n \tag{3.17}$$

3. By substituting Eqs. (3.9) and (3.13) into Eq. (3.7), Eq. (3.18) as implicit formula is obtained for solving $\boldsymbol{v}_\mathrm{i}^{n+\frac{1}{2}}$ analytically. Thus, $\boldsymbol{v}_\mathrm{i}^{\frac{1}{2}}$ is obtained from $\boldsymbol{v}_\mathrm{i}^0$, Z^0, m_i^0, $\boldsymbol{E}^0$ and $\boldsymbol{B}^0$ by usinfg Eq. (3.19). (● in Fig. 3.3.)

$$m_\mathrm{i}^n\frac{\mathrm{d}\boldsymbol{v}_\mathrm{i}^n}{\mathrm{d}t} = Z^n e\left(\boldsymbol{E}^n + \boldsymbol{v}_\mathrm{i}^n\times\boldsymbol{B}^n - \frac{\eta}{\mu_0}\nabla\times\boldsymbol{B}^n\right) \tag{3.18}$$

$$\frac{\mathrm{d}\boldsymbol{v}_\mathrm{i}^0}{\mathrm{d}t} = \frac{\boldsymbol{v}_\mathrm{i}^{\frac{1}{2}} - \boldsymbol{v}_\mathrm{i}^0}{\Delta t/2} \tag{3.19}$$

4. The central difference of $\boldsymbol{v}_\mathrm{i}^{n+\frac{1}{2}}$ as Eq. (3.20) is divided into Eqs. (3.21) and (3.22). Since $\boldsymbol{v}_\mathrm{i}^{\frac{1}{2}}$ is known, $\boldsymbol{x}^{\frac{1}{2}}$ and $\boldsymbol{x}^1$ are obtained from Eqs. (3.21) and (3.22), respectively. Then, PIC algorithm interpolates $n_\mathrm{i}^{\frac{1}{2}}$, $\boldsymbol{j}_\mathrm{i}^{\frac{1}{2}}$, $Z^{\frac{1}{2}}$ and $m_\mathrm{i}^{\frac{1}{2}}$ for each grid point. (● in Fig. 3.3.)

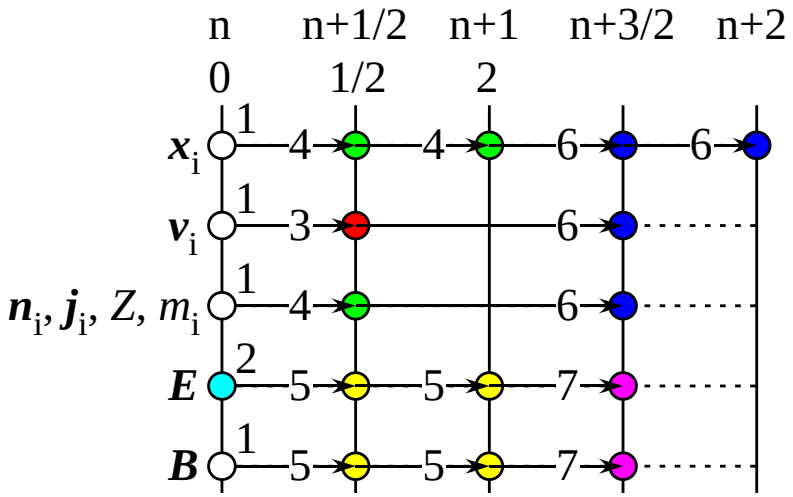

Figure 3.3: Update steps in time of leapfrog algorithm.

$$\frac{\mathrm{d}\boldsymbol{x}^{n+\frac{1}{2}}}{\mathrm{d}t} = \frac{\boldsymbol{x}^{n+1} - \boldsymbol{x}^{n}}{\Delta t} = \boldsymbol{v}_{\mathrm{i}}^{n+\frac{1}{2}} \tag{3.20}$$

$$\boldsymbol{x}^{n+\frac{1}{2}} = \boldsymbol{x}^{n} + \frac{\Delta t}{2}\boldsymbol{v}_{\mathrm{i}}^{n+\frac{1}{2}} \tag{3.21}$$

$$\boldsymbol{x}^{n+1} = \boldsymbol{x}^{n+\frac{1}{2}} + \frac{\Delta t}{2}\boldsymbol{v}_{\mathrm{i}}^{n+\frac{1}{2}} \tag{3.22}$$

3.4.2 Cycle steps

Firstly, $\boldsymbol{x}^n$, $\boldsymbol{B}^n$, $\boldsymbol{E}^n$, $\boldsymbol{v}_{\mathrm{i}}^{n+\frac{1}{2}}$, $n_{\mathrm{i}}^{n+\frac{1}{2}}$, $\boldsymbol{j}_{\mathrm{i}}^{n+\frac{1}{2}}$, $Z^{n+\frac{1}{2}}$, $m_{\mathrm{i}}^{n+\frac{1}{2}}$ and $\boldsymbol{x}^{n+1}$ are already known. The predictor corrector algorithm and the successive over-relaxation (SOR) algorithm are used to solve equations iteratively for $\boldsymbol{E}^{n+1}$ and $\boldsymbol{B}^{n+1}$. By using the new electromagnetic field, the particle positions can be advanced to $n + 3/2$. Finally, $\boldsymbol{x}^{n+1}$, $\boldsymbol{B}^{n+1}$, $\boldsymbol{E}^{n+1}$, $\boldsymbol{v}_{\mathrm{i}}^{n+\frac{3}{2}}$, $n_{\mathrm{i}}^{n+\frac{3}{2}}$, $\boldsymbol{j}_{\mathrm{i}}^{n+\frac{3}{2}}$, $Z^{n+\frac{3}{2}}$, $m_{\mathrm{i}}^{n+\frac{3}{2}}$ and $\boldsymbol{x}^{n+2}$ are obtained.

3.5 Calculation of electromagnetic field

3.5.1 Plasma-vacuum interface

In order to calculate the field quantities at the grid points, this code determines by whether that the grid points is in the plasma or vacuum region as shown in Fig. 3.4. The black area indicates the outside of calculation region. The moving plasma-vacuum interface is not used to treat vacuum region (See Appendix C). This method adequately treats variation in low density plasma region to depart the two regions. The threshold of ion density is empirically determined as 10^{16} cm^{-3}. Thus, the grid points which ion density is larger than the threshold are in the plasma region. The other points are determined to be the vacuum region. Then, in each region, the electric field is calculated by predictor corrector and SOR algorithms, respectively.

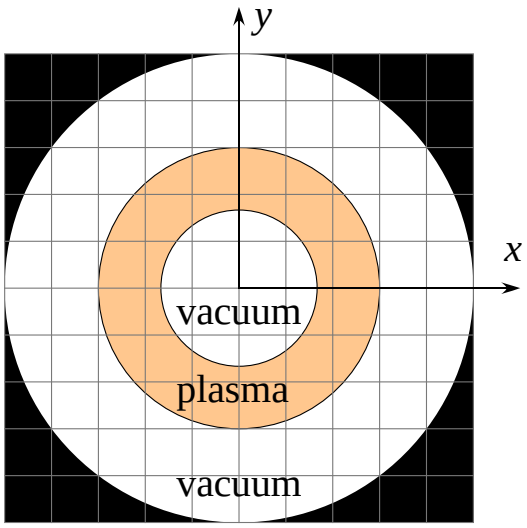

Figure 3.4: A schematic of the grid points used in the plasma and vacuum region. The black area is the outside of calculation region.

3.5.2 Predictor corrector algorithm for plasma region

The time advance of the electromagnetic field in the plasma region is accomplished by the predictor corrector algorithm. This algorithm is numerically stability, gives good energy conservation and is also used the arbitrary plasma-vacuum interface. The calculation processes are as follows. (Figure 3.3 indicates the each step.)

Initial step

5. Equation (3.23) shows Maxwell-Faraday's law. Equation (3.24) indicates the central difference of $\boldsymbol{B}^n$. By substituting Eq. (3.24) into (3.23), Eq. (3.25) is obtained. The straightforward way to advance the magnetic field to level $n + 1/2$ is to use Eq. (3.25) and $\boldsymbol{E}^n$.

$$\frac{\mathrm{d}\boldsymbol{B}^n}{\mathrm{d}t} = \frac{\boldsymbol{B}^{n+\frac{1}{2}} - \boldsymbol{B}^{n-\frac{1}{2}}}{\Delta t} = -\nabla \times \boldsymbol{E}^n \tag{3.23}$$

$$\boldsymbol{B}^n = \frac{\boldsymbol{B}^{n+\frac{1}{2}} + \boldsymbol{B}^{n-\frac{1}{2}}}{2} \tag{3.24}$$

$$\boldsymbol{B}^{n+\frac{1}{2}} = \boldsymbol{B}^n - \frac{\Delta t}{2}\nabla \times \boldsymbol{E}^n \tag{3.25}$$

Since $\boldsymbol{B}^{n+\frac{1}{2}}$ is known, $\boldsymbol{E}^{n+\frac{1}{2}}$ is calculated from Eq. (3.17). Thus, $\boldsymbol{E}^{n+1}_{\mathrm{pred}}$ is predicted from the following equation Eq. (3.26).

$$\boldsymbol{E}^{n+\frac{1}{2}} = \frac{\boldsymbol{E}^{n+1}_{\mathrm{pred}} + \boldsymbol{E}^n}{2}$$

$$\boldsymbol{E}^{n+1}_{\mathrm{pred}} = 2\boldsymbol{E}^{n+\frac{1}{2}} - \boldsymbol{E}^n \tag{3.26}$$

$\boldsymbol{B}^{n+1}_{\mathrm{pred}}$ is predicted from Eq. (3.27). (○ in Fig. 3.3.)

$$\frac{\boldsymbol{B}^{n+\frac{3}{2}} - \boldsymbol{B}^{n+\frac{1}{2}}}{\Delta t} = -\nabla \times \boldsymbol{E}^{n+1}$$

$$\boldsymbol{B}^{n+1} = \frac{\boldsymbol{B}^{n+\frac{3}{2}} + \boldsymbol{B}^{n+\frac{1}{2}}}{2}$$

$$\boldsymbol{B}^{n+1}_{\mathrm{pred}} = \boldsymbol{B}^{n+\frac{1}{2}} - \frac{\Delta t}{2}\nabla \times \boldsymbol{E}^{n+1}_{\mathrm{pred}} \tag{3.27}$$

6. Because $\mathrm{d}\boldsymbol{v}_{\mathrm{i}}^{n+1}/\mathrm{d}t$ is given as following equation Eq. (3.28), $\boldsymbol{v}_{\mathrm{i,pred}}^{n+\frac{3}{2}}$ is predicted by using Eq. (3.18). $\boldsymbol{x}_{\mathrm{pred}}^{n+\frac{3}{2}}$ is also predicted by using Eq. (3.21). PIC algorithm calculates $n_{\mathrm{i,pred}}^{n+\frac{3}{2}}, \boldsymbol{j}_{\mathrm{i,pred}}^{n+\frac{3}{2}}, Z_{\mathrm{pred}}^{n+\frac{3}{2}}$ and $m_{\mathrm{i,pred}}^{n+\frac{3}{2}}$. Finally, $\boldsymbol{x}_{\mathrm{pred}}^{n+2}$ is obtained by using Eq. (3.22). (● in Fig. 3.3.)

$$\frac{\mathrm{d}\boldsymbol{v}_{\mathrm{i}}^{n+1}}{\mathrm{d}t} = \frac{\boldsymbol{v}_{\mathrm{i,pred}}^{n+\frac{3}{2}} - \boldsymbol{v}_{\mathrm{i}}^{n+\frac{1}{2}}}{\Delta t} \tag{3.28}$$

7. Some iteration is needed to give convergence because the magnetic field has to been improved in advancing after the electric field advanced. (● in Fig. 3.3.)

Cycle steps

(a) The predicted fields at the time step $n+3/2$ is computed with the newly $\boldsymbol{E}^{n+\frac{1}{2}}$ evaluated by using Eq. (3.17). Maxwell-Faraday's law as shown in Eq. (3.27) can be used to push magnetic field to the newly $\boldsymbol{B}_{\mathrm{pred}}^{n+1}$. Equation (3.29) indicates $\boldsymbol{B}_{\mathrm{pred}}^{n+\frac{3}{2}}$ by using Eq. (3.25).

$$\boldsymbol{B}^{n+\frac{3}{2}}_{\mathrm{pred}} = \boldsymbol{B}^{n+1}_{\mathrm{pred}} - \frac{\Delta t}{2}\nabla \times \boldsymbol{E}^{n+1}_{\mathrm{pred}} \tag{3.29}$$

$\boldsymbol{E}_{\rm pred}^{n+\frac{3}{2}}$ is predicted by using Eq. (3.17). The corrected electronic field at the time step $n+1$ is determined from Eq. (3.30).

$$\boldsymbol{E}^{n+1} = \frac{\boldsymbol{E}_{\rm pred}^{n+\frac{3}{2}} + \boldsymbol{E}^{n+\frac{1}{2}}}{2} \tag{3.30}$$

(b) The corrected magnetic field at the time step $n+1$ is determined from Eq. (3.31).

$$\boldsymbol{B}^{n+1} = \boldsymbol{B}^{n+\frac{1}{2}} - \frac{\Delta t}{2}\nabla \times \boldsymbol{E}^{n+1} \tag{3.31}$$

(c) The processes could be repeated to improve the accuracy as shown in Eq. (3.32).

$$\frac{|\boldsymbol{B}^{n+1,\rm new} - \boldsymbol{B}^{n+1,\rm old}|}{|\boldsymbol{B}^{n+1,\rm old}|} \leq 0.01 \tag{3.32}$$

3.5.3 SOR algorithm for vacuum region

The rhs of Eq. (3.14) includes the term inversely proportional to the ion density. In the vacuum region, this term becomes infinity and the calculation diverges. To avoid this problem, the Laplace equation $\nabla^2 \boldsymbol{E} = 0$ is solved to obtain the electric field in the vacuum region. Equation (3.33) is the central difference of the Laplace equation, where Δp is the mesh width and Ep is the electric field for each direction. The subscription p indicates x or y or z direction.

$$\frac{Ep_{i-1,j,k} - 2Ep_{i,j,k} + Ep_{i+1,j,k}}{\Delta x^2}$$
$$+\frac{Ep_{i,j-1,k} - 2Ep_{i,j,k} + Ep_{i,j+1,k}}{\Delta y^2}$$
$$+\frac{Ep_{i,j,k-1} - 2Ep_{i,j,k} + Ep_{i,j,k+1}}{\Delta z^2} = 0 \tag{3.33}$$

When Δx is equal to Δy, the newly electric field is taken from Eq. (3.33).

$$Ep^{*\text{old}}_{i,j,k} = \frac{\Delta z^2}{4\Delta z^2 + 2\Delta x^2}\{Ep^{\text{old}}_{i-1,j,k} + Ep^{\text{old}}_{i+1,j,k} + Ep^{\text{old}}_{i,j-1,k} + Ep^{\text{old}}_{i,j+1,k}\}$$
$$+\frac{\Delta x^2}{4\Delta z^2 + 2\Delta x^2}\{Ep^{\text{old}}_{i,j,k-1} + Ep^{\text{old}}_{i,j,k+1}\} \tag{3.34}$$

The new electric field is predicted by using Eq. (3.35) and SOR method.

$$Ep^{\text{new}}_{i,j,k} = Ep^{\text{old}}_{i,j,k} + \alpha(Ep^{*\text{old}}_{i,j,k} - Ep^{\text{old}}_{i,j,k}) \tag{3.35}$$

Equation (3.36) indicates the acceleration coefficient for the rectangular area which is usually set between 0 and 2, where L is the represent length. Here, α is determined to be 1. This is called Gauss-Seidel method.

$$\alpha = \frac{2}{1 + \sin(\pi/L)} \tag{3.36}$$

The processes could be repeated to improve the accuracy as shown in Eq. (3.37).

$$\frac{Ep^{*\text{new}}_{i,j,k} - Ep^{\text{new}}_{i,j,k}}{Ep^{*\text{old}}_{i,j,k} - Ep^{\text{old}}_{i,j,k}} \leq 0.01 \tag{3.37}$$

3.6 Summary

In this Chapter, we described the basic equations and the numerical algorithms of the 3D hybrid PIC code used in the present study for simulating the behavior of charged particles in a magnetic field.

Bibliography

[1] Horowitz, E. J., Shumaker, D. E., and Anderson, D. V., "QN3D: A Three-Dimensional Quasi-neutral Hybrid Particle-in-Cell Code with Applications to the Tilt Mode Instability in Field Reversed Configurations," *J. Comput. Phys.*, Vol. 84, Issue 2, 1989, pp. 279-310. doi: 10.1016/0021-9991(89)90234-9

[2] Harned, D. S., "Quasineutral Hybrid Simulation of Macroscopic Plasma Phenomena," *J. Comput. Phys.*, Vol. 47, Issue 3, 1982, pp. 452-462. doi: 10.1016/0021-9991(82)90094-8

[3] Winske, D., Yin, L., Omidi, N., Karimabadi, H., and Quest, K. B., "Hybrid Simulation Codes: Past, Present, Future-A Tutorial," *Space Plasma Simulations*, Vol. 615, 2003, pp. 136-165.

[4] Kajimura, Y., and Nakashima, H., "Verification of Hybrid Particle-in-Cell Simulation Model for Advanced Plasma Propulsions: Magneto Plasma Sail and Magnetic Nozzle for Laser Fusion Rocket," *J. Space Technol. Sci.*, Vol. 25, Issue 2, 2011, pp. 34-54.

[5] Matsumoto, M., Kajimura, Y., Funaki, I., and Shinohara, I., "Development of Hybrid Particle-In-Cell Simulation Code for Research of Magnet Plasma Sail," JAXA Research and Development Memorandum RM-11-019, 2012. [In Japanese]

[6] Birdsall, C. K., and Langdon, A. B., "Plasma Physics via Computer Simulation," Francis & Taylor, New York, 2004, Chapter 2.

[7] Naitou, Y., "Basic Theory of Particle Simulation," *J. Plasma Fusion Res.*, Vol. 74, Issue 5, 1998, pp. 470-478. [In Japanese]

[8] Birdsall, C. K., and Langdon, A. B., "Plasma Physics via Computer Simulation," Francis & Taylor, New York, 2004, Appendix C.

[9] Mankofsky, A., Sudan, R. N., and Denavit, J., "Hybrid Simulation of Ion Beams in Background Plasma," *J. Comput. Phys.*, Vol. 70, Issue 1, 1987, pp. 89-116. doi: 10.1016/0021-9991(87)90003-9

[10] Bagdonat, T., and Motschmann, U., "3D Hybrid Simulation Code Using Curvilinear Coordinates," *J. Comp. Phys.*, Vol. 183, Issue 2, pp. 470-485. doi: 10.1006/jcph.2002.7203

Chapter 4

Direct measurement of impulse

4.1 Introduction

Direct measurement of impulse due to the interaction between a diamagnetic current in a laser-produced plasma and a magnetic field produced by cylindrical neodymium permanent magnets were performed. The impulse was directly measured by using a pendulum type thrust stand for various laser pulse energies at EUV database and GXII laser facilities of ILE in the collaboration with Osaka University. [1, 2, 3, 4]. In addition to the experiments, to confirm the validity of the modified numerical simulation computing high energy laser injection onto a spherical target and the ablation plasma dynamics in a magnetic field, the numerical simulations were performed for comparing the measured impulse with the calculated impulse.

4.2 Dependence of impulse on laser pulse duration

4.2.1 Experimental setup for EUV facility

Figure 4.1 is a photo of the vacuum chamber in the EUV database laser facility. The experimental setup for EUV facility is shown in Fig. 4.2. A laser-produced plasma is created by a 1064 nm single-beam neodymium: yttrium aluminum garnet (Nd:YAG) laser focusing into a 500 μm wide in diameter polystyrene ([-CH_2-$CH(C_6H_6)$-]$_n$) spherical target. The target is suspended at the end of a carbon fiber attached to a glass rod to reduce the influence of ablation plasma generated by the glass rod. The laser beam spot diameter is the same as the target diameter by using a lens having F-number of 20. Six cylindrical neodymium permanent magnets connected in the z-axis are used for producing the magnetic field. The permanent magnet itself is 16 mm in diameter and 10 mm long. The surface magnetic flux density of each individual permanent magnet is 0.47 T. The magnetic field strength at the target is calculated to be 0.12 T, as shown in Fig. 4.3. This value was confirmed by a gauss meter. The permanent magnets are arranged so as not to disturb the incoming laser beam. The distance between the surface of the permanent magnets and the target is 11 mm. The angle between the z-axis of the permanent magnets and the laser beam is also 45 °.

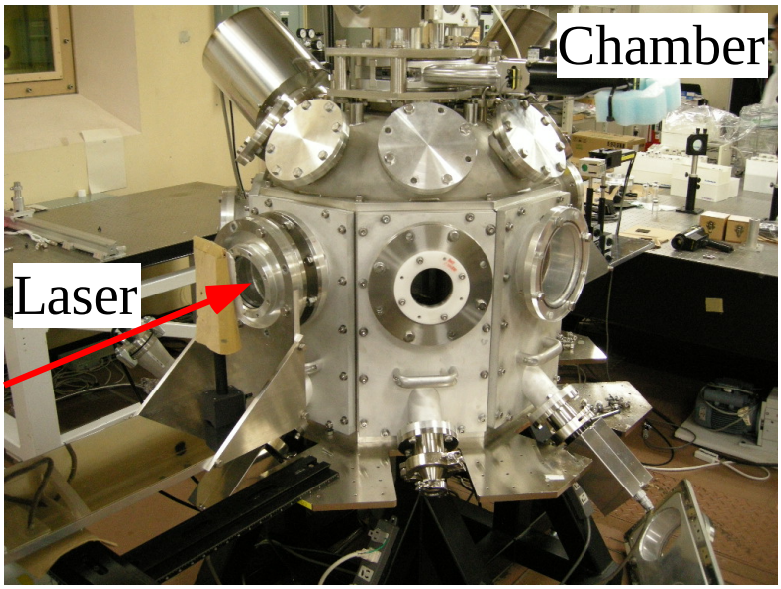

Figure 4.1: Vacuum chamber in the EUV facility.

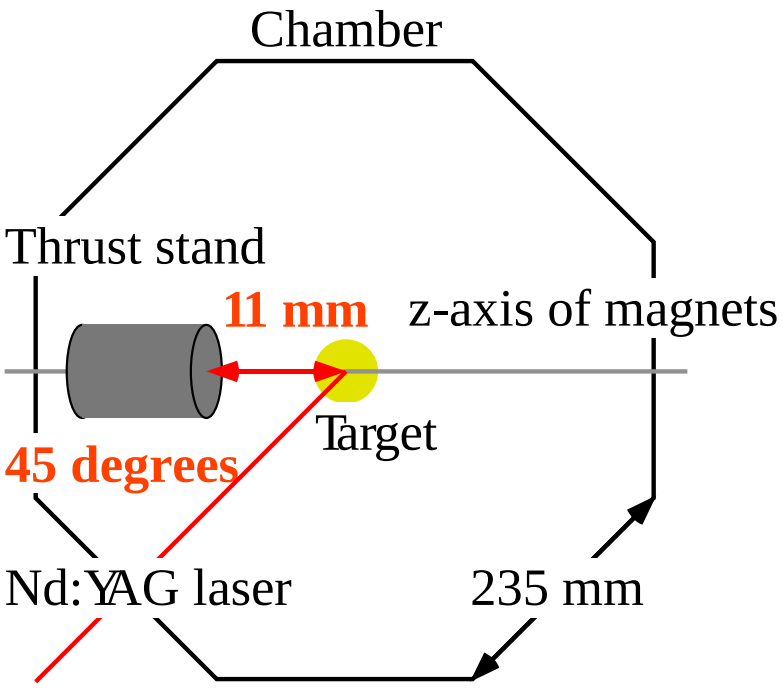

Figure 4.2: Experimental setup for EUV facility.

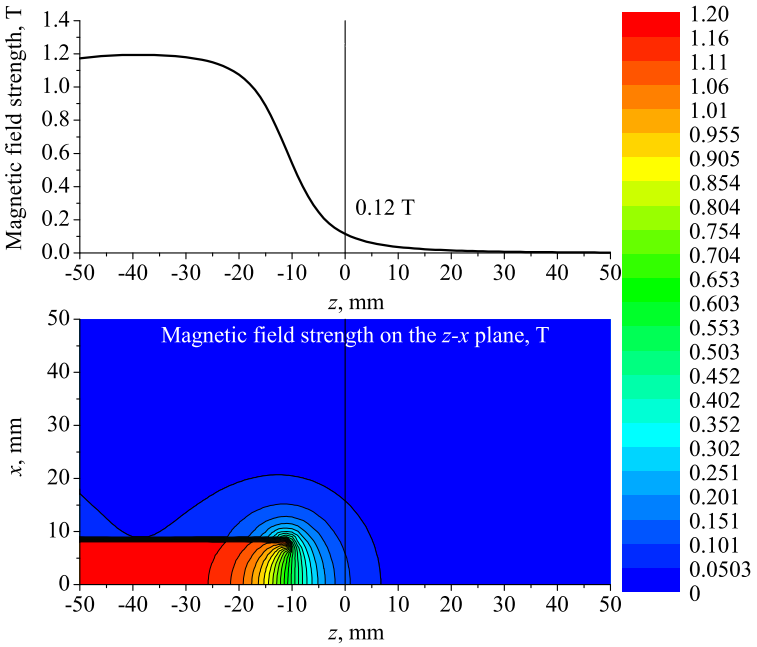

Figure 4.3: Calculated magnetic field strength produced by the permanent magnets at the z-axis at $x = y = 0$ and in the $z - x$ plane at $y = 0$. The magnetic field strength at the origin is 0.12 T.

4.2.2 Pendulum type thrust stand for EUV facility

The impulse is measured by means of a pendulum type thrust stand for EUV facility, as shown in Fig. 4.4. The stand is composed of the permanent magnets, knife edges, counter weights, light emitting diode (LED) displacement sensors, and an oil damper. The magnets are installed on the top of the pendulum. The pendulum is supported by the knife edges mounted on side posts. The counterweight is placed on the pendulum such that the center of gravity lies in the pendulum's axis of rotation. This ensures that the pendulum swings easily even for a small impulse. The natural period of this pendulum is 1.2 second. The LED sensors detect the deflection of the pendulum. To decrease the error in the impulse measurement, i.e., to offset the mechanical noise experienced by the sensors, the LED sensors are placed face-to-face and supplied by a single power source. The oil damper is installed to suppress mechanical noise induced by background vibrations, which are critical problems for small impulse measurements. To prevent the stand from momentum transfer due to the direct collisions between the expanding plasma and the permanent magnets, a ceramic plate is placed at a distance of 1 mm from the magnets to shield from the plasma. This plate is connected to a grounded vacuum chamber. The stand is calibrated by using small hammer which takes impulse to the stand. The impact is directly measured by a force transducer attached to the counterweight. The force transducer records the impulsive force as a function of time; integrating this yields the applied impulse. It is assumed that the impulse on the force transducer is proportional to the amplitude of the actual response of the LED sensors. This assumption allows for a linear curve fit to the calibration data, as shown in Fig. 4.5. The correlation coefficient (R^2) is determined to be 0.99922. The experimental data are converted into an impulse force using the conversion factor 70 μNs/V found from the calibration.

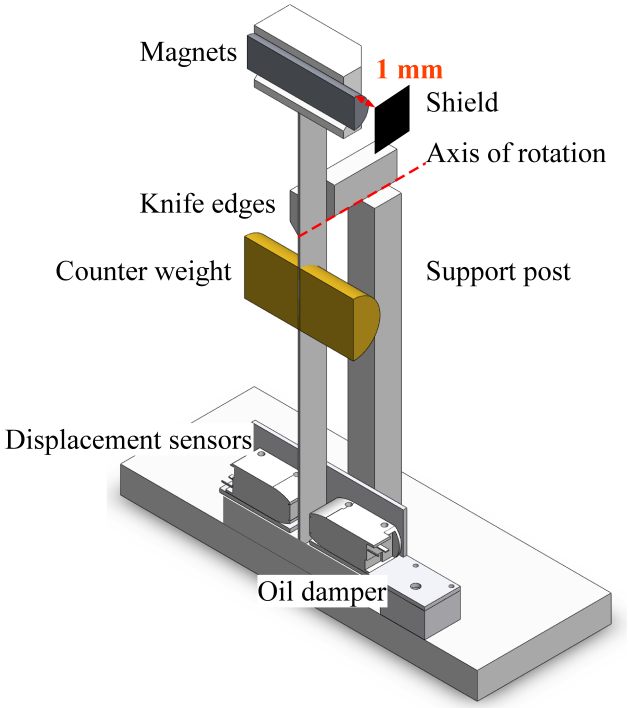

Figure 4.4: Schematic of the pendulum type thrust stand for EUV facility. (vertical sectional view)

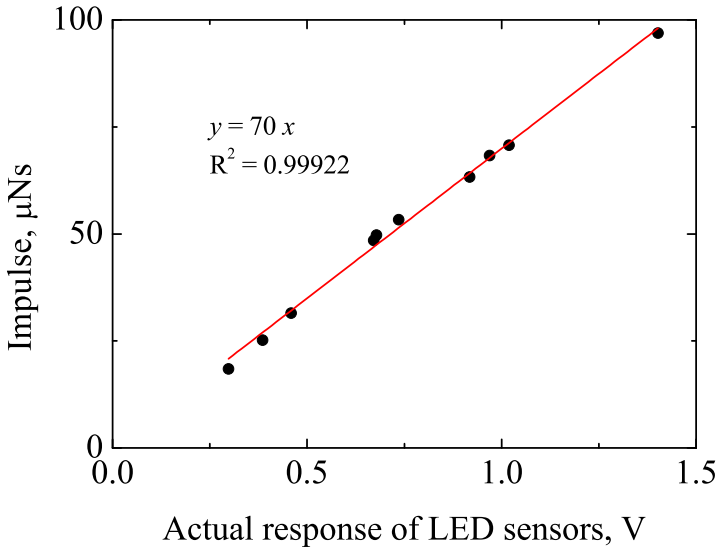

Figure 4.5: Applied calibration force as a function of the signals of LED sensors and the liner curve fitting to the calibration data.

4.2.3 Results and discussion for EUV facility

Figure 4.6 shows the impulses measured on the pendulum type thrust stand for EUV facility as a function of incident laser energies. The two data sets show the measured impulses for single laser shot with laser pulse duration of 9 ns and 3 ns, respectively. Every data point plotted is the average result over more than three shots; the error is estimated for the associated standard deviation. In every shot, the incident laser energy and laser pulse duration have some error from the setting value. The effects of them are considered to be the main cause of the error bars on the measured impulse.

When a non-magnetized iron cylinder is installed on the pendulum type thrust stand instead of the permanent magnets, the measured impulse is zero. The result shows the interaction between the diamagnetic current in the laser-produced plasma and the magnetic field of the permanent magnets. Thus, the magnetic thrust chamber system for LFR is demonstrated to produce impulse experimentally.

The impulse is 2.0 μNs at the laser pulse duration of 9 ns, and it is 1.5 μNs at the laser pulse duration of 3 ns, when the incident laser energy is 0.7 to 0.8 J. The difference between 9 ns and 3 ns can be considered as follows. When charged particles of the laser-produced plasma are pushed back by the magnetic field before they collide to the shield plate, the estimated impulse is assumed to be the product of the plasma ablation mass and the ion acoustic speed C_s, i.e., $S\tau_\mathrm{L}\dot{m}C_\mathrm{s}$. S is the plasma ablation area of the target by focusing the incident laser beam. τ_L is the laser pulse duration. The plasma expansion velocity into a vacuum is approximately equal to the ion acoustic speed. The plasma ablation mass per unit area per unit time $\dot{m}$ and the ion acoustic speed are expressed as follows [5], where m_e is the electron mass and m_i is the ion mass. The critical density n_c is 9.8 $\times 10^{26}$ m^{-3}.

$$\dot{m} = \frac{n_{\mathrm{c}}^{2/3}}{Z}\left(\frac{3K_{\mathrm{a}}I_{\mathrm{L}}}{4f}\right)^{1/3}\sqrt{(1+Z)m_{\mathrm{e}}^{1/3}m_{\mathrm{i}}} \tag{4.1}$$

$$C_{\mathrm{s}} = \left(\frac{3K_{\mathrm{a}}I_{\mathrm{L}}}{4fn_{\mathrm{c}}}\right)^{1/3}\sqrt{\frac{(1+Z)m_{\mathrm{e}}^{1/3}}{m_{\mathrm{i}}}} \tag{4.2}$$

Here, the charge number of ion Z is assumed to be 4 (C^{4+} is assumed to be the primary ion in the plasma), the laser absorption coefficient K_{a} and the flux limit factor f is empirically assumed to be 1 and 0.08 [5], respectively. I_{L} is the incident laser intensity, which has the relationship $I_{\mathrm{L}} = E_{\mathrm{L}}/S\tau_{\mathrm{L}}$, where E_{L} is the incident laser energy. In the experiments, the plasma ablation area is assumed to be the surface of target where the solid angle is 0.4π steradian, as shown in Fig. 4.7. Thus, the plasma ablation area is fixed to be 7.9 $\times 10^{-8}$ m^2.

The curves in Fig. 4.6 represent the estimated impulse, i.e., $S\tau_{\mathrm{L}}\dot{m}C_{\mathrm{s}}$. The solid and dashed lines are shown for laser pulse duration of 9 ns and 3 ns, respectively. According to Eqs. (4.1) and (4.2), the plasma ablation mass and expansion velocity increase with increasing incident laser intensity, that is, $\dot{m} \propto I_{\mathrm{L}}^{1/3}$ and $C_{\mathrm{s}} \propto I_{\mathrm{L}}^{1/3}$. When E_{L} is constant ($\tau_{\mathrm{L}} \propto I_{\mathrm{L}}^{-1}$), the impulse is proportional to $S\tau_{\mathrm{L}}\dot{m}C_{\mathrm{s}} \propto I_{\mathrm{L}}^{-1/3}$, that is, $\tau_{\mathrm{L}}^{1/3}$. Thus, the impulse increases theoretically with the laser pulse duration. The experimental dependence of impulse on laser pulse duration shown in Fig. 4.6 is in good agreement with the estimated values.

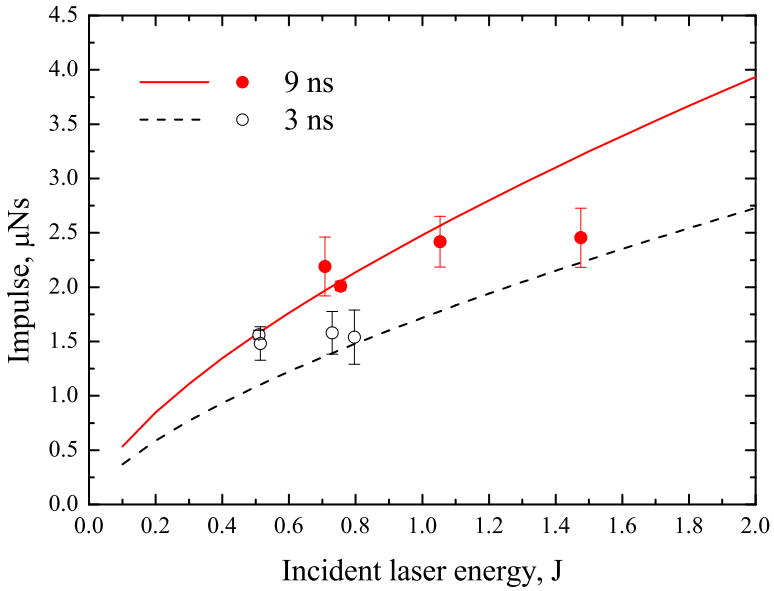

Figure 4.6: Impulses measured on the pendulum type thrust stand as a function of incident laser energies for laser pulse duration of 3 ns and 9 ns.

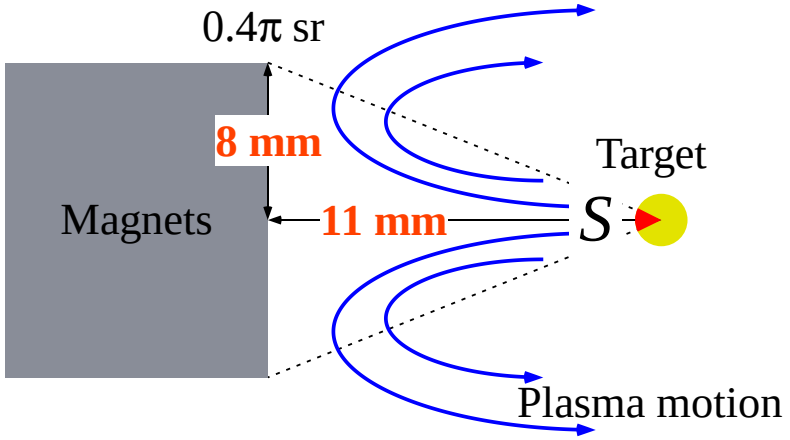

Figure 4.7: Impulse model of the product of plasma ablation mass and ion acoustic speed.

4.3 Dependence of impulse on laser pulse wavelength and incident laser energy

4.3.1 Experimental setup for GXII facility

A plasma is generated by focusing a 1.3 ns laser beam onto a 1.5 mm diameter spherical polyacetal ($[\text{-CH}_2\text{O-}]_n$) target at GXII facility. The target is suspended at the end of a carbon fiber attached to a glass rod to reduce the influence of ablation plasma generated by the glass rod. Figure 4.8 is a picture of the vacuum chamber in the GXII facility. The experimental setup is shown in Fig. 4.9. The glass laser beam is focused using a lens (F-number: 3) so that its diameter is equal to that of the target. A cylindrical neodymium permanent magnet is used to generate the magnetic field. The maximum energy product of the magnet is 0.382 mJ/mm^3. The permanent magnet is 50 mm diameter and 40 mm long. It is located at where it does not obstruct the laser beam. The distance between the permanent magnet surface and the target center is 33 mm and the angle between the permanent magnet axis and the laser beam is 66.5°. The magnetic field strength at the target is calculated to be 0.1 T, as shown in Fig. 4.10. This value was confirmed by a gauss meter.

4.3.2 Pendulum type thrust stand for GXII facility

The impulse is measured using a pendulum type thrust stand for GXII facility (See Fig. 4.9). The pendulum type thrust stand for GXII facility is largely similar to the stand for EUV facility and consists of the permanent magnet, bearings, a counterweight and LED displacement sensors. The pendulum is supported by the bearings, which are mounted on side posts. The pendulum has a natural period of 1.3 s. This is short enough to reduce the mechanical noise induced by background vibrations, which are problematic

when measuring small impulses. A ceramic plate connected to a grounded vacuum chamber is placed 2 mm from the magnet to shield it from the plasma. Figure 4.11 indicates the calibration data. The R^2 coefficient is 0.99953. The experimental data are converted into forces using a conversion factor of 240 μNs/V, which is obtained from the calibration.

Figure 4.8: Vacuum chamber in the GXII facility.

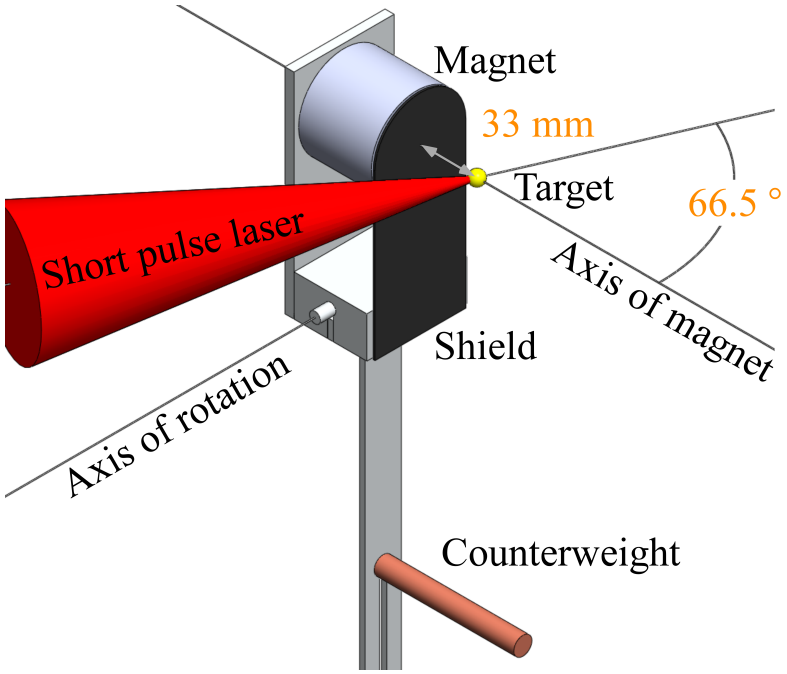

Figure 4.9: Experimental setup & Schematic of the pendulum type thrust stand for GXII facility.

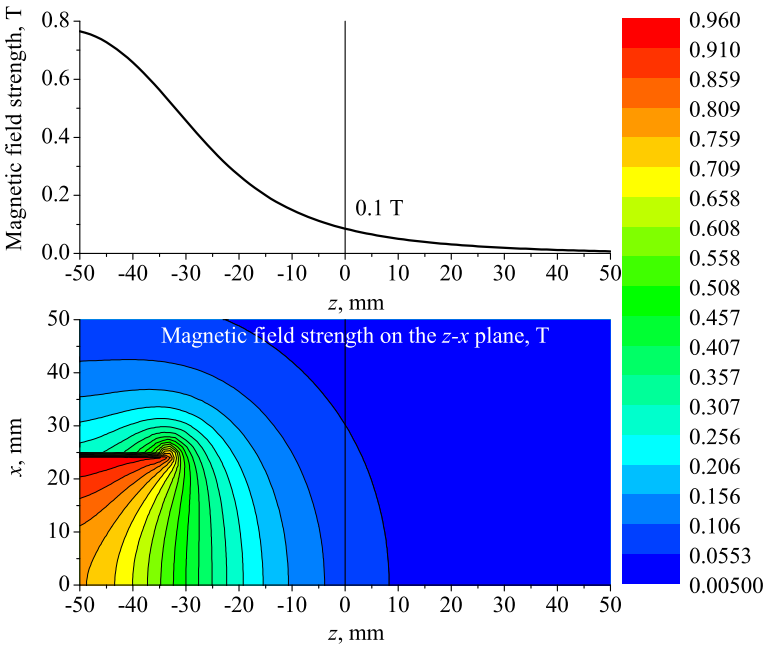

Figure 4.10: Calculated magnetic field strength produced by the permanent magnet at the z-axis at $x = y = 0$ and in the $z - x$ plane at $y = 0$. The magnetic field strength at the origin is 0.1 T.

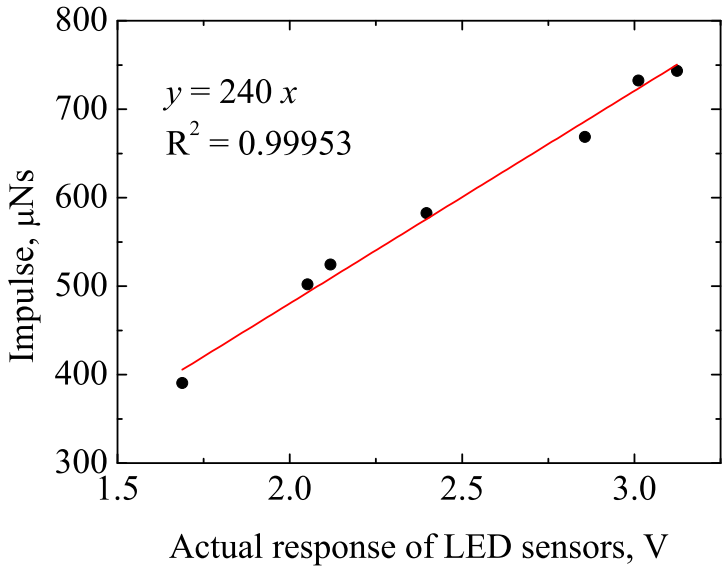

Figure 4.11: Applied calibration force as a function of the signals of LED sensors and the liner curve fitting to the calibration data.

4.3.3 Results and discussion for GXII facility

Figure 4.12 shows the impulses measured on the pendulum type thrust stand as a function of the incident laser energy. The three data sets show impulses for single laser shots with laser frequencies of ω (λ_L=1,053 nm), 2ω (λ_L=527 nm) and 3ω (λ_L=351 nm), where λ_L is the laser pulse wavelength. Impulses of 1.3, 5.0, and 6.4 mNs are generated at laser frequencies of ω, 2ω and 3ω for incident laser energies of 548, 568 and 550 J, respectively. Figure 4.12 shows that impulses 3ω is the largest, followed in order by those of 2ω and ω. In addition, it shows that the impulse increases with increasing incident laser energy.

The impulse for a specific laser wavelength as shown in Fig. 4.12 is estimated using the estimation model similar to that of EUV facility. The lines in Fig. 4.12 are the estimated impulse curves obtained by assuming that the impulse is equal to the product of the plasma ablation mass and the ion acoustic speed. All the plasma is pushed back by the magnetic field before it collides with the plate of the stand. In this case, the plasma ablation area of the target is constant at 3.5×10^{-6} m^2, when the area is assumed to be equal to the target surface for a solid angle of 2π since the target is irradiated by a single laser beam through a lens with an F-number of 3.

The critical density for each laser frequency is 1.0×10^{27} m^{-3} for ω, 4.0×10^{27} m^{-3} for 2ω, and 9.0×10^{27} m^{-3} for 3ω. According to Eqs. (2.1), (4.1) and (4.2), the product of the plasma ablation mass and the expansion velocity increases with increasing critical density and incident laser energy; that is, $\dot{m}C_s \propto \lambda_L^{-2/3}$ and $I_L^{2/3}$. Since τ_L is constant, the impulse is proportional to $S\tau_L\dot{m}C_s \propto \lambda_L^{-2/3}$ and $E_L^{2/3}$. Thus, the estimated impulse increases with decreasing laser pulse wavelength and increasing incident laser energy. The measured impulses, which are indicated by the plots in Fig. 4.12. The results show that the same trends as the estimation model.

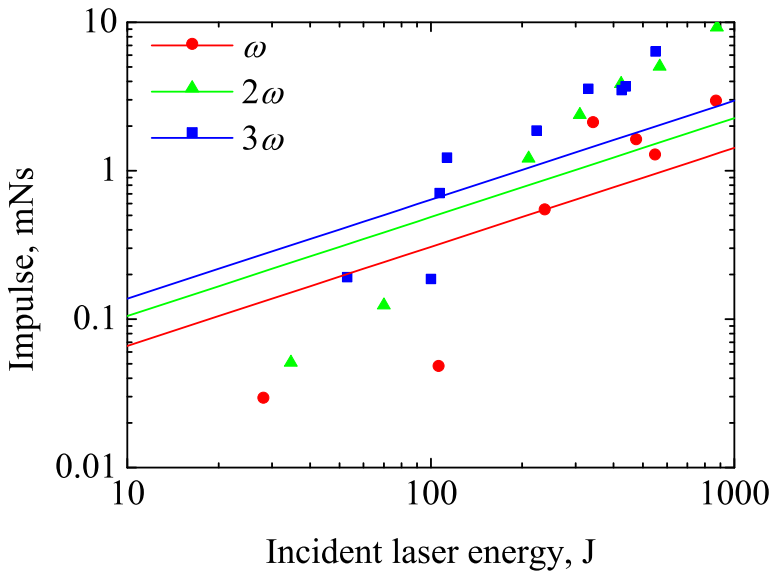

Figure 4.12: Impulses measured on the pendulum type thrust stand as a function of incident laser energies for laser pulse wavelength.

4.4 Comparison of measured and calculated impulse

4.4.1 Numerical simulation with and without considering creation process of laser-produced plasma

In the original numerical simulation modeling the experiment of EUV facility, Maxwellian parameters is used as the initial plasma parameters inputted into the 3D hybrid PIC code. The laser-produced plasma is assumed to be uniform. The plasma radius is set to 9 mm because the plasma expands isotropically. The plasma mass Nm_{i} is equal to the target mass (6.9 $\times$ 10^{-8} kg) under the assumption that all the target is ionized. The number of ion super particles N is 1,000,000. The charge state of the ions $< Z >$ is assumed to be 1.25 (=C^{4+}+H^{+}/4), since laser-produced plasma is weakly ionized plasma. <> indicates averaging over the ion species. The atomic mass m_{i} is 6.5 amu. The ion density is 2.1 $\times$ 10^{18} cm^{-3} since the plasma radius is 9 mm and the mass density of polystyrene is 1.06 $\mathrm{g/cm}^3$. The ion super particle expansion velocity distribution in the plasma is assumed to be Maxwellian, as shown in Eq. (4.3) and Fig. 4.13, where v is the expansion velocity, k_{B} is the Boltzmann constant and T_{i} is the ion temperature. The plasma kinetic energy is 0.3 J for incident laser energy of 1.0 J since the absorption rate is assumed to be 0.3. This is our empirical prediction from the target and laser conditions. The characteristic velocity v_p is 2.4 km/s.

$$
\begin{aligned}
f(v) &= 4\pi v^2 \left(\frac{m_{\mathrm{i}}}{2\pi k_{\mathrm{B}} T_{\mathrm{i}}}\right)^{\frac{3}{2}} \exp\left(\frac{-m_{\mathrm{i}} v^2}{2k_{\mathrm{B}} T_{\mathrm{i}}}\right) \\
\frac{3}{2} N k_{\mathrm{B}} T_{\mathrm{i}} &= 0.3 \ \ \mathrm{J} \\
k_{\mathrm{B}} T_{\mathrm{i}} &= \frac{1}{2} m_{\mathrm{i}} v_p^2
\end{aligned}
\tag{4.3}
$$

Furthermore, to improve the numerical simulation of the magnetic thrust chamber system for LFR, the modified numerical simulation employing a 3D hybrid PIC code and Star-1D, which accounts for the creation process of a laser-produced plasma, was performed. Table 4.1 lists the characteristic initial plasma conditions inputted into the 3D hybrid PIC code for the original and modified cases.

Numerical simulation of a 3D hybrid PIC code is performed for two initial conditions with and without considering the creation process of a laser-produced plasma. The calculation model of the 3D hybrid PIC code is illustrated in Fig. 4.14. This model is an $100\Delta x \times 100\Delta x \times 100\Delta x$ cube, where Δx=1 mm is the mesh width. The calculation time is $100{,}000\Delta t$ (5 μs), where Δt=50 ps.

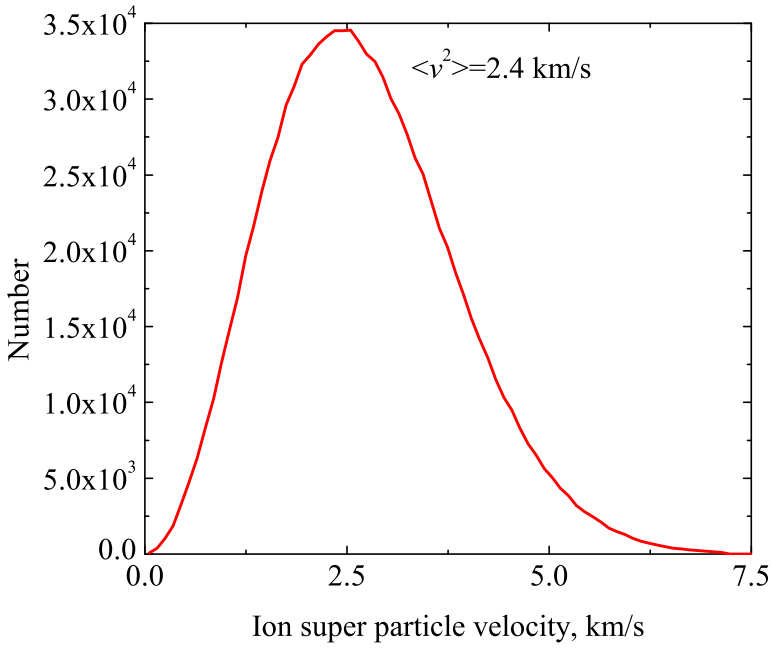

Figure 4.13: Maxwell super particle velocity distribution. The characteristic velocity is assumed to be v_p=2.4 km/s.

Table 4.1: Plasma conditions for original and modified cases.

	Original case	Modified case
Plasma radius, mm	9	6
Plasma mass, kg	6.9×10^{-8}	2.5×10^{-8}
Atomic mass, amu	6.5	6.5
<Atomic number>	1.25	0.36
Ion density, cm^{-3}	2.1×10^{18}	non-uniform
Kinetic energy, J	0.30	0.58
Ion expansion velocity	Maxwell distribution	non-uniform
Initial max. velocity, km/s	7.5	117

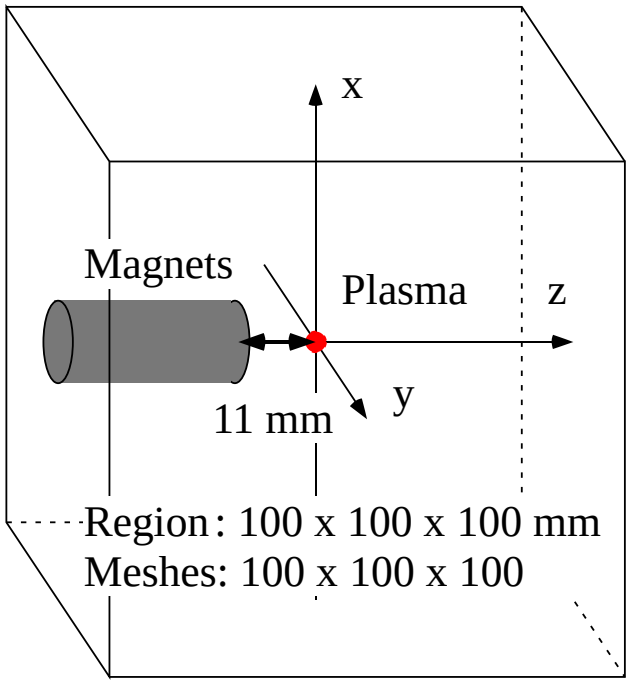

Figure 4.14: Cubic calculation model of 3D hybrid PIC code.

4.4.2 Results and discussion for numerical simulations

The modified numerical simulation with considering the creation process of a laser-produced plasma combines Star-1D and the 3D hybrid PIC code described in Chaps. 2 and 3, respectively. Figure 4.15 shows the unit vector distributions of the diamagnetic current calculated by the modified numerical simulation at calculation times of 75 ns, 1.325, 2.575 and 3.825 μs. At 75 ns, the plasma is expanding isotropically. Then, with updating calculation time, the current rotates clockwise. It is indicated that the plasma produced the diamagnetic cavity as shown in Fig. 1.2.

The measured impulse is 2.42 ± 0.23 μNs at a laser pulse energy of 1.05 J and a laser pulse duration of 9 ns. In the numerical simulations, the original numerical simulation used only a 3D hybrid PIC code, which employs the initial plasma conditions without considering the creation process of a laser-produced plasma; it computed the impulse to be 72.7 μNs. There is a large difference between these results. On the other hand, the calculated impulse of the modified numerical simulation is 10.3 μNs. The impulse of the modified numerical simulation does not agree with the value of the previous experiment. This is considered that the ablation plasma on the opposite surface of laser injection is not calculated well. However, the value is closer to that of the experiment than that of the original numerical simulation. This indicates that the creation process of a laser-produced plasma (initial plasma condition) is important when investigating plasma behavior in a magnetic field by numerical simulations. This is considered to be because the different ion expansion velocities calculated by the two numerical simulations affect the impulse. Consequently, the modified numerical simulation can describe the ablation plasma dynamics in the magnetic field but the original numerical simulation does not. This confirms the validity of the modified numerical simulation.

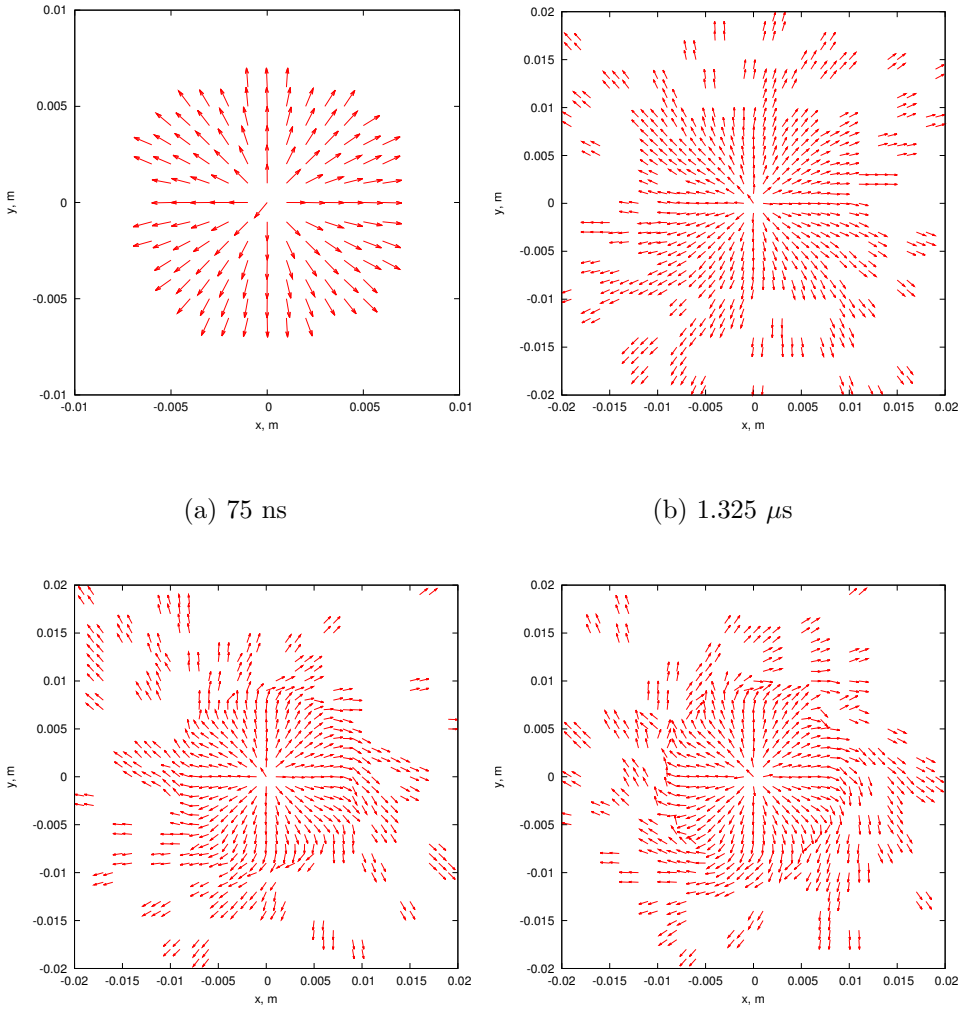

(a) 75 ns

(b) 1.325 μs

(c) 2.575 μs

(d) 3.825 μs

Figure 4.15: Unit vector distributions of diamagnetic current calculated by modified and original numerical simulation.

4.5 Summary

In this Chapter, we described the direct measurement of impulse due to the interaction between a diamagnetic current in the laser-produced plasma and a magnetic field produced by the cylindrical neodymium permanent magnet.

In the experiments, the impulse was measured directly by means of a pendulum type thrust stand for various incident laser energies at EUV database and GXII laser facilities of ILE in the collaboration with Osaka University. The pendulum type thrust stand was fabricated for measuring a small impulse. Without a magnetic field, the measured impulse was zero. On the other hand, with a magnetic field, impulse was generated. These results show that the system for generating impulse works as theory tells. Thus, the system was demonstrated experimentally for eventual use in a space propulsion system. The experiments also found that the dependences of the impulse on the laser pulse duration, laser wavelength and incident laser energy in the system. Thus, for producing large impulse, it is revealed that longer pulse durations, shorter wavelengths and higher energies are better.

In the numerical simulations, in order to compare the measured impulse of EUV facility with the calculated ones, the original and modified numerical simulations were performed. The modified numerical simulation combining Star-1D and the 3D hybrid PIC code computes high energy laser injection onto a spherical target and the ablation plasma dynamics in a magnetic field. The original numerical simulation does not consider the creation process of a laser-produced plasma. The measured impulse was 2.42 $\pm$ 0.23 μNs at a laser pulse energy of 1.05 J and a laser pulse duration of 9 ns. The calculated impulse of the original case was 72.7 μNs. There is a large difference between these results. The calculated impulse for the modified case was 10.3 μNs. From these values, the calculated impulse of the modified case is closer to

the measured impulse than the original case. This indicates that the creation process of a laser-produced plasma is important factor for the numerical simulation.

The achievements in this Chapter are as follows.

Experiments

- By using cylindrical neodymium permanent magnet and non-magnetized iron cylinder, impulse due to the interaction between a diamagnetic current in a laser-produced plasma and a magnetic field was generated and the magnetic thrust chamber system for LFR was demonstrated experimentally to work as theory tells.
- The impulse for the duration of 9 ns was larger than that of 3 ns. The impulse increases, as the laser pulse duration becomes longer.
- The impulse for the wavelength of 3ω is the largest, followed in order by that of 2ω and ω. The impulse increases, as the laser wavelength becomes shorter.
- The impulse increases with increasing the incident laser energy.
- In order to produce large impulse, longer pulse durations, shorter wavelengths and higher energies enlarge the impulse.

Numerical simulations

- The measured impulse of EUV facility was compared with the calculated impulse.
- The modified numerical simulation with considering the creation process of a laser-produced plasma as the initial plasma conditions of the 3D hybrid PIC code was performed.

- The modified numerical simulation can describe the ablation plasma dynamics in the magnetic field but the original numerical simulation does not. This confirms the validity of the modified numerical simulation.

Bibliography

[1] Akira Kakami, "Study of pulsed plasma thrusters by using liquid propellants," Ph.D. Dissertation, University of Tokyo Graduate School of Engineering, 2002. [In Japanese]

[2] Koizumi, H., Kakami. A., Komurasaki, K., and Arakawa, Y., "A Thrust Stand for Low-Power Electric Propulsion," *Journal of the Japan Society for Aeronautical and Space Sciences*, Vol. 51, Issue 593, 2003, pp. 270-275. [In Japanese]

[3] Koizumi, H., Komurasaki, K., and Arakawa, Y., "Development of thrust stand for low impulse measurement from microthrusters," *Rev. Sci. Instrum.*, Vol. 75, Issue 10, 2004, pp. 3185-3190. doi: 10.1063/1.1790568

[4] Tahara, H., "Dependence of Solid Propellant Species on Performance of Small Laser Ablative Thrusters," *J. IAPS*, Vol. 16, Issue 1, 2008, pp. 27-32. [In Japanese]

[5] Azechi, H., "Concept of Laser Fusion.," *J. Plasma Fusion Res.*, Vol. 81, 2005, pp. 2-10. [in Japanese].

Chapter 5

Comparison of ion expansion velocity

5.1 Introduction

In addition to the direct measurement of the impulse, we measured the ion expansion velocity of a laser-produced plasma in a magnetic field. The magnetic field is produced by an edgewise coil at EUV database laser facility of ILE in the collaboration with Osaka University. To confirm the validity of the modified numerical simulation with considering the creation process of a laser-produced plasma, the numerical simulations with and without considering the creation process were performed for comparing with the experimental result.

5.2 Experiment for measuring ion expansion velocity

5.2.1 Experimental setup

Figure 5.1 shows the experimental setup. A laser-produced plasma is created by focusing a 1064 nm Nd:YAG laser beam (laser pulse duration: 9 ns; incident laser energy: 4 J) onto a 500-μm-diameter spherical polystyrene target. The laser beam is focused on the central axis of the coil by a lens (F-number: 20) so that its diameter is equal to that of the target. To reduce the measurement error caused by the ablation plasma generated by the glass rod, the target is suspended on the end of a carbon fiber attached to a glass rod. A pulsed power supply and an edgewise coil are used to generate a pulsed magnetic field. The coil (outer diameter: 60 mm; inner diameter: 50 mm; length: 10 mm) that generates the magnetic field consists of 10 turns of a rectangular copper wire (width: 5 mm; thickness perpendicular to the coil axis: 1 mm) as shown in Fig. 5.2. The wire is coated with a polyimide thin film, as an insulator, whose breakdown voltage is 10 kV. The edgewise coil has a high lamination factor, a small temperature difference between the inside and outside of the coil, and a high-frequency response. The coil is set 25 mm from the origin as shown in Fig. 5.1.

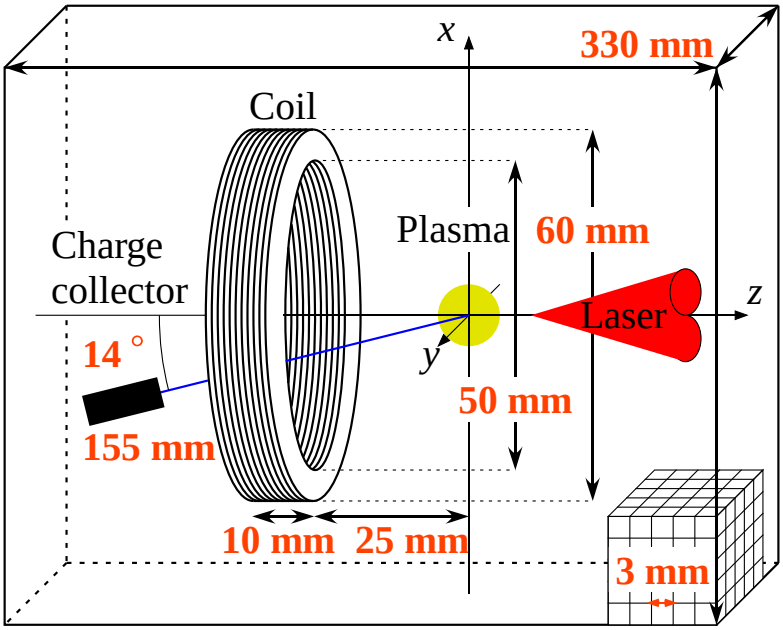

Figure 5.1: Experimental setup & Cubic calculation model of 3D hybrid PIC code.

Figure 5.2: Edgewise coil for generating a pulsed magnetic filed.

5.2.2 Charge collector with a Faraday cup

The ion beam current of a laser-produced plasma is measured using a charge collector with a Faraday cup. The distance between the charge collector and the origin is 155 mm. The angle between the charge collector and a single laser beam is 14° as shown in Fig. 5.1. Figure 5.3 shows the charge collector that consists of a Faraday cup [1, 2, 3] and the current-to-voltage (I-V) converter. The charge collector in the vacuum chamber is biased to -50 V to repel electrons. Four resistors with a resistance of 50 Ω each are used for impedance matching and signal denoising through the high pass filter. The Faraday cup reabsorbs secondary electrons, making it very suitable for absolute measurement. This is because that almost none of the secondary electrons generated in the Faraday cup escape from the charge collector through the 2-mm-diameter hole, as shown in Fig. 5.3. To prevent electrons in the plasma from entering the Faraday cup, the hole is covered with a mesh which has 500 lines/inch with a line diameter of 0.025 mm and an ion penetration rate of 25%.

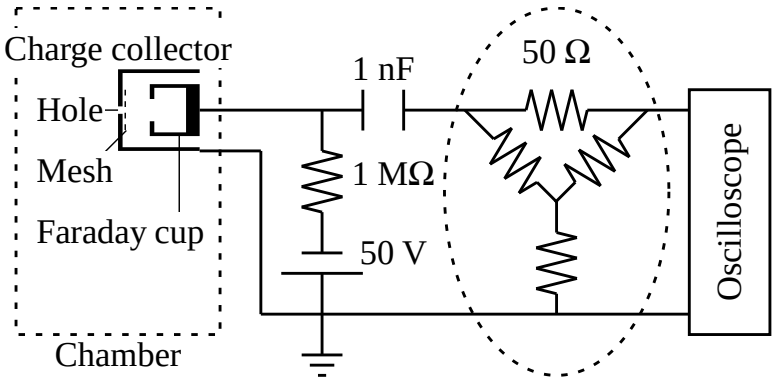

Figure 5.3: Charge collector with a Faraday cup and an I-V converter. The 2-mm-diameter hole is covered with a mesh to prevent electrons in the plasma from entering the Faraday cup.

5.2.3 Pulsed power supply for generating high pulsed current

Pulse Forming Network

It is difficult for neodymium permanent magnet to generate strong magnetic field flexibility, since the surface magnetic flux density of the neodymium permanent magnet is within 0.5 T. On the other hand, coil and high-current can make strong magnetic field than the permanent magnets. For producing high pulsed current, pulsed power supply is superior to steady power supply under the thermal limitation of circuit diagram. Thus, we made a pulsed power supply using a 3-step pulse forming network (PFN) [4, 5, 6]. PFN consists of a series of energy storage capacitors for high-voltage and inductors which are interconnected as a ladder network. The circuit diagram of the supply is shown in Fig. 5.4. The edgewise coil in the vacuum chamber has a self-inductance of 7 μH.

The oil capacitors made by General Atomics corporation (Model 39745) are rapidly charged by means of a high-voltage direct-current power supply via a high-voltage switch; the charging voltage is V_{C}. The switch is GH2 (withstand voltage; 10 kV and allowable current; 25 A) made by Gigavac corporation. Another assemblies for storing electrical energy consists of a charging resistor (100 kΩ), and a potential divider (1 GΩ and 1 MΩ).

The section for releasing high pulsed current consists of three capacitors (withstand voltage; 5 kV, capacitance C; 32 μF), two self-made inductors (inductance L; 2 μH), a metal clad wire wound resistor, a fast high-voltage solid-state diode and a thyristor switch as shown in Fig. 5.5. The inductance of the inductors is determined by the measurement with probe and calculation [7]. The diode and the thyristor switch are FDA-100-300 (withstand voltage; 16 kV and peak current; 3 kA) and HTS 120-1600-SCR (withstand voltage; 12 kV and peak current; 16 kA) made by Behlke corporation, respec-

tively. They have much faster switching capability because of their unipolar conduction. The functional drawback of the thyristor switch, like a diode, only conducts in one direction.

To prevent an oscillating current, a matching impedance Z_{PFN} is needed. The impedance is the following equation.

$$Z_{\mathrm{PFN}} = \sqrt{\frac{L}{C}} \tag{5.1}$$

The impedance is determined to be 250 mΩ from Eq. (5.1). The resistor is IRH300 (power consumption; 300 W) made by PCN corporation. PFN accumulates electrical energy over a comparatively long time, and then releases the stored energy in the form of a relatively square pulse of comparatively short duration. The duration τ_{PFN} is expressed as follows, where n is the number of step of PFN. Here, n is three.

$$\tau_{\mathrm{PFN}} = 2n\sqrt{LC} \tag{5.2}$$

The peak current I_{PFN} of PFN is also expressed as follows. The supply can theoretically generate a maximum current of 10 kA with 48 μs when the charging voltage is 5 kV.

$$I_{\mathrm{PFN}} = \frac{V_{\mathrm{C}}}{2Z_{\mathrm{PFN}}} \tag{5.3}$$

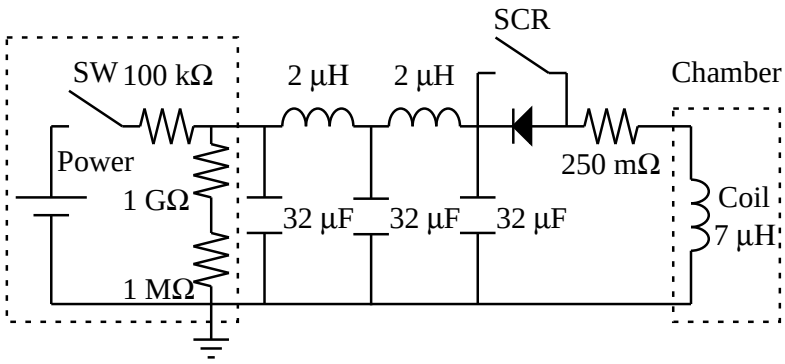

Figure 5.4: Circuit diagram of pulsed power supply with a 3-step PFN.

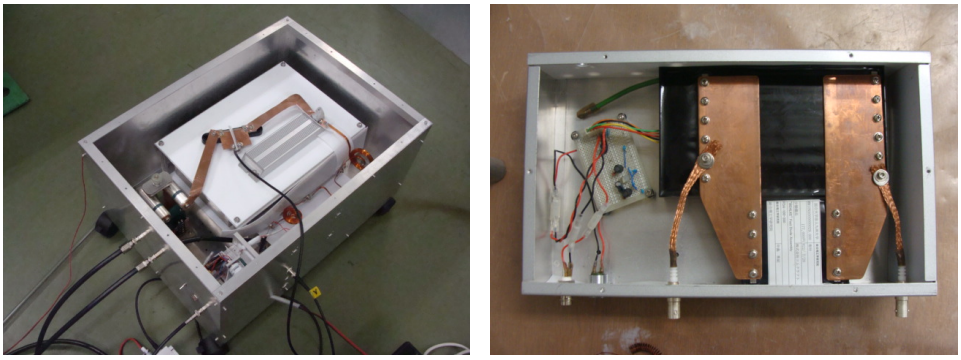

Figure 5.5: Pulsed power supply made by myself.

Rogowski coil

Rogowski coil [8] is an electrical device for measuring high-frequency pulsed current as shown in Fig. 5.6, where N is the number of turns and l is the circumference of the coil. The coil is a helical coil. The both terminals of lead wire are at the same end of the coil. This allows the coil to be open-ended and flexible, and be installed and wrapped easily around a live conductor of the pulsed power supply without disturbing the conductor. It is highly linear for the current because the coil has no iron core to saturate and a low inductance. Equation (5.4) indicates the voltage produced by a rogowski coil, where μ_0 is the permeability of vacuum, A is the area of one of the poloidal loops, and $\mathrm{d}I_{\mathrm{PFN}}/\mathrm{d}t$ is the derivation of the circuit current. This formula assumes that the turns are evenly spaced.

$$E_{\mathrm{in}} = -\frac{\mu_0 AN}{l}\frac{\mathrm{d}I_{\mathrm{PFN}}}{\mathrm{d}t} = K_{\mathrm{r}}\frac{\mathrm{d}I_{\mathrm{PFN}}}{\mathrm{d}t} \tag{5.4}$$

The output of the rogowski coil is connected to the integral and non-inverting amplifier circuits. Figure 5.7 indicates equivalent circuit diagram of these circuit. The output of the external circuit is proportional to the current as shown in Eq. (5.5), where A_{f} is $1 + 100\mathrm{k}\Omega/4.7k\Omega$.

$$E_{\mathrm{out}} = \frac{K_{\mathrm{r}}A_{\mathrm{f}}}{1\mathrm{k}\Omega \times 1\mu\mathrm{F}}I_{\mathrm{PFN}} \tag{5.5}$$

Since $0.001K_{\mathrm{r}}A_{\mathrm{f}}$ in Eq. (5.5) calibrated and determined, the current of this pulsed power supply is measured from the output of this rogowski coil.

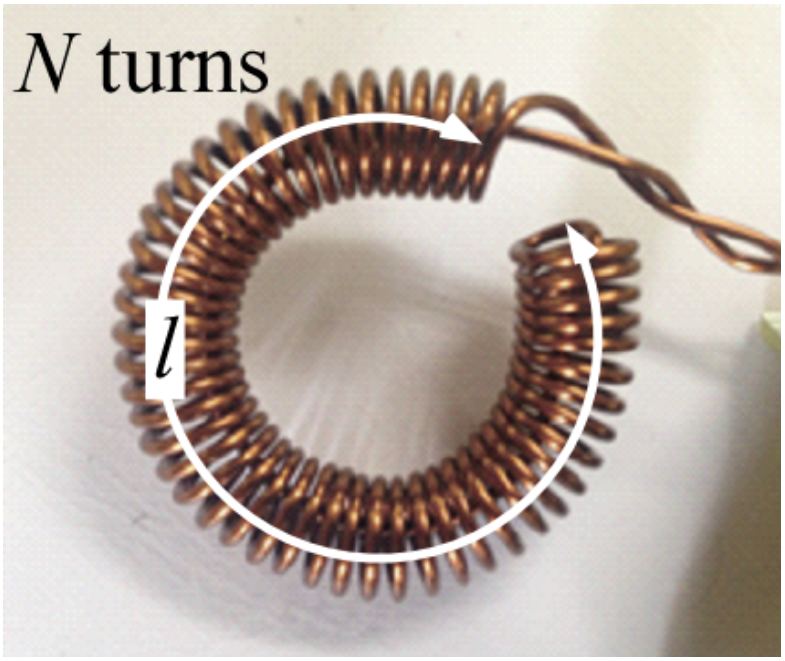

Figure 5.6: Rogowski coil for measuring a pulsed current.

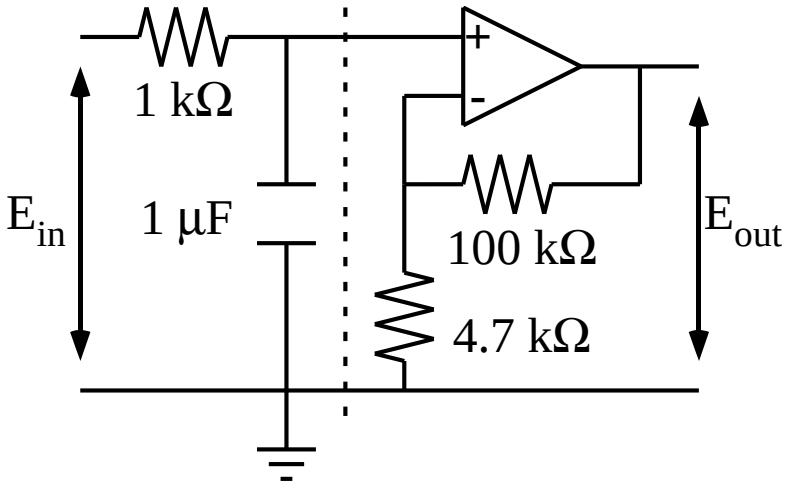

Figure 5.7: Equivalent circuit diagram of integral and non-inverting amplifier circuits.

Figure 5.8 shows the experimental and simulated output currents of this supply when measuring a rogowski coil and a potential drop across a 0.002 mΩ current shunt resistor for a charging voltage of 230 V. The noises at the time of 0 s, -31 and 59 μs are caused by a laser injection and a flip of the thyristor switch. The monitored currents agree well with the simulated value. The peak current is 450 A at the time of 10 μs. The current starts to flow 31 μs before laser ignition induced by a digital delay/pulse generator for generating the strongest peak current at the laser ignition.

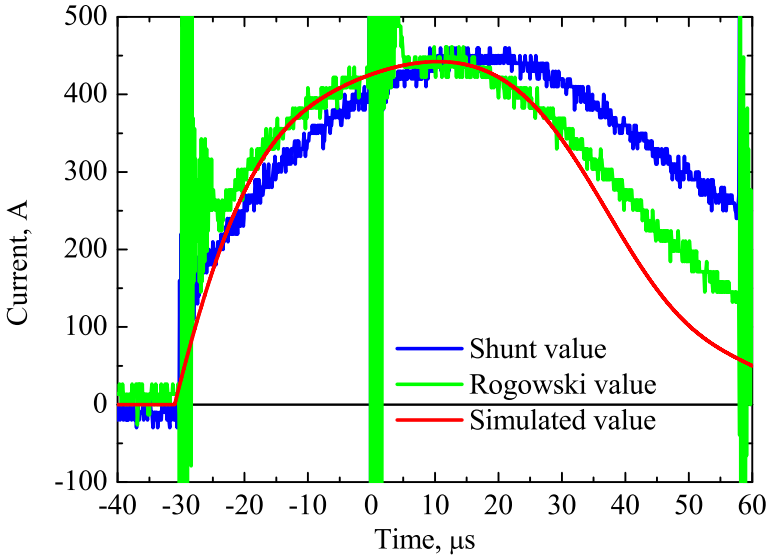

Figure 5.8: Experimental and theoretical output currents of pulsed power supply at the peak current of 450 A. Current starts flowing 31 μs before laser ignition.

5.3 Numerical simulation with and without considering creation process of laser-produced plasma

5.3.1 Calculation model of Star-1D

To compute this experiment using a CH spherical target with a diameter of 500 μm, the target is divided into six parts. Each part has a solid angle of 0.636π steradian, as shown in Fig. 5.9. In the experiment, a single laser beam is focused onto the target. In contrast, a single laser beam is assumed to be focused onto each part in Star-1D. The surface area of the part in Star-1D is equal to the laser beam spot size (i.e., the full width at half maximum of the laser beam). Each laser beam has energy of 0.636 J; i.e., the total energy of the laser beams focused onto the target is about 4 J. The laser beam is generated by a 1064 nm Nd:YAG laser with a Gaussian intensity profile. Figure 5.10 shows the Gaussian time-variable power profile of the laser beam. The rise and fall times of the peak power are 10 and 20 ns, respectively. The peak power of the laser beam is 2.51×10^8 W at the calculation time of 25 ns. The distance between the laser focal point and the target is set to 0.5 cm. The number of radial meshes with widths in the range 0.01 to 1 μm is 500. They move with the hydrodynamic evolution of the plasma heated by the laser beam. For a CH material, the atomic mass averaged over carbon and hydrogen and the mass density are assumed to be 6.5 amu and 1.06 g/cm^3, respectively. The calculation start and finish times are set to zero and 75 ns, respectively. The calculation time step Δt is initially set to 0.1 ps and it is subsequently varied according to the CFL condition [9].

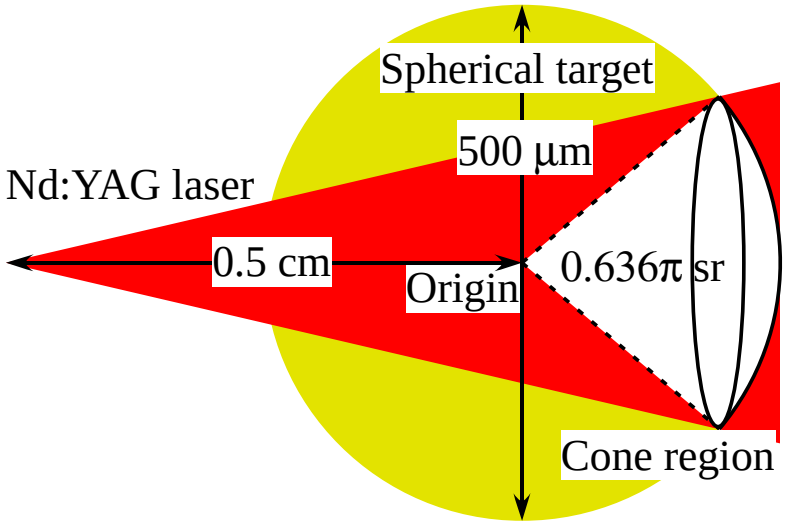

Figure 5.9: Lagrangian calculation model for ray-tracing.

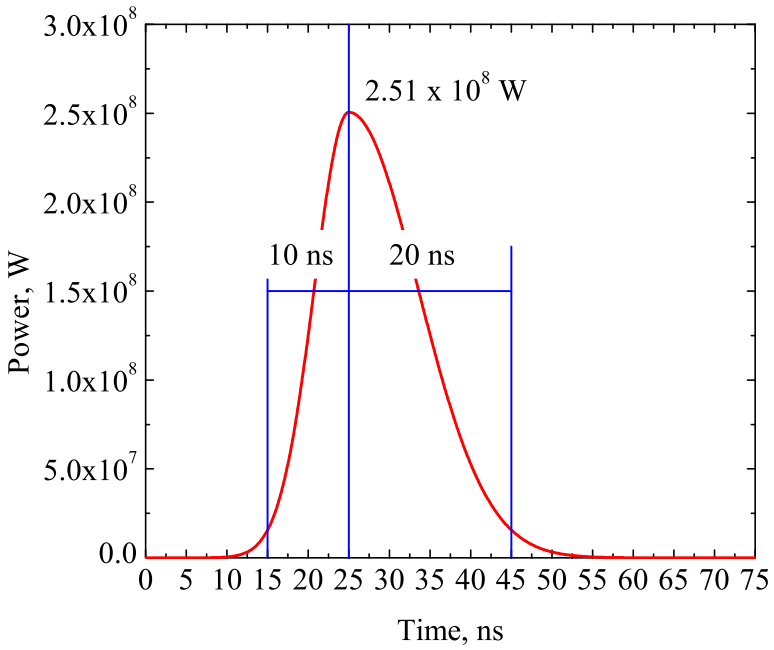

Figure 5.10: Gaussian time-variable power profile of a single laser beam.

5.3.2 Results and discussion of Star-1D

Figure 5.11 shows the results of Star-1D at the calculation time of 75 ns. The horizontal axis represents the radius of the laser-produced plasma from the center of plasma. The ablation and expansion surfaces are located at radii of 0.25 and 9 mm. The vertical axes represent the 1D ion density n_{i}, the ion expansion velocity v, and the charge state of ion Z in the plasma. The material between the center and a radius of 0.25 mm is not considered to be ionized because the ion expansion velocity in this region is zero.

Figure 5.12 indicates the time-variation of plasma kinetic, internal and radiation energies. The absorption rate is 93% of the incident laser energy (4.0 J). The plasma has kinetic and inertial energies at 75 ns of 3.1 J (78% of incident laser energy) and 0.26 J (7% of the incident laser energy), respectively. The remaining absorption energy is the heat loss from the expansion surface. The ablation plasma mass is 2.1×10^{-8} kg (30%) for a target mass of 6.9×10^{-8} kg. The ablation plasma expanding into vacuum expands nearly isothermally. Consequently, the ion expansion velocity increases to 175 km/s and the ion density decreases exponentially, as shown in Fig. 5.11. The charge state of ion near a radius of 5 mm is rapidly altered by shock waves.

The results of Star-1D are used as the initial plasma conditions, which are inputted into the 3D hybrid PIC code. The conditions are 3D distributions of ion super particle for the particle position, expansion velocity, charge state and mass.

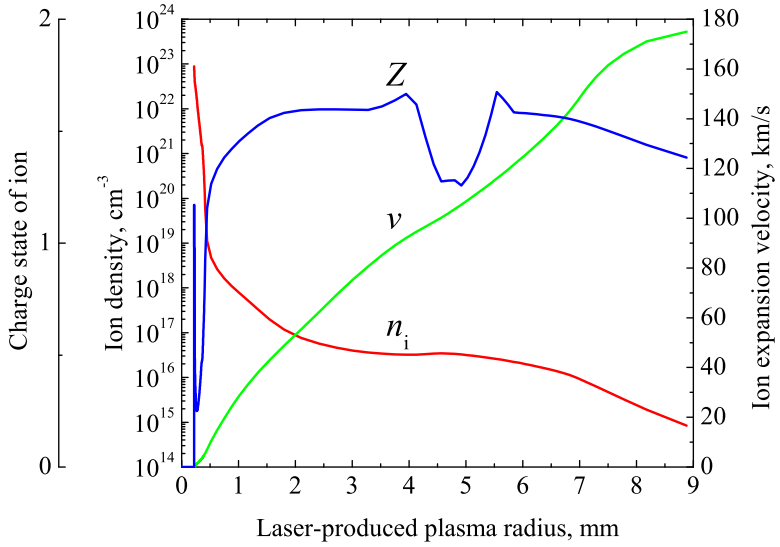

Figure 5.11: 1D distributions of plasma for ion density, ion expansion velocity, and charge state as a function of plasma radius at 75 ns.

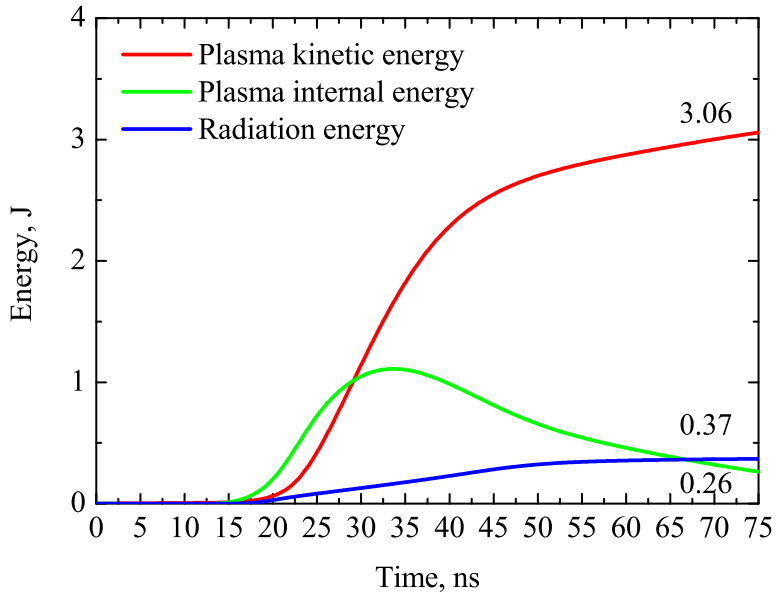

Figure 5.12: Time-variation of plasma kinetic, internal and radiation energies.

5.3.3 Calculation model of 3D hybrid PIC code

The initial laser-produced plasma is located at the origin of the model as shown in Fig. 5.1. The model is an $110\Delta x \times 110\Delta x \times 110\Delta x$ cube, where Δx=3 mm is the mesh width. Figure 5.13 shows the magnetic field strength along the central axis of z at $x = y = 0$ and in the $z - x$ plane at $y = 0$ produced by the edgewise coil at the peak current of 450 A. The magnetic field strength at the origin is calculated to be 0.0321 T. The calculation start time is set to zero. At this time, numerical simulations are changed from Star-1D to the 3D hybrid PIC code. The number of ion super particles is 1,000,000. The calculation time is $100{,}000\Delta t$ (5 μs), where Δt=50 ps (ion cyclotron frequency ω_{ci}=$1/2047\Delta t$) is the time step. It is according to CFL condition. Table 5.1 lists the characteristic plasma conditions for the original and modified cases.

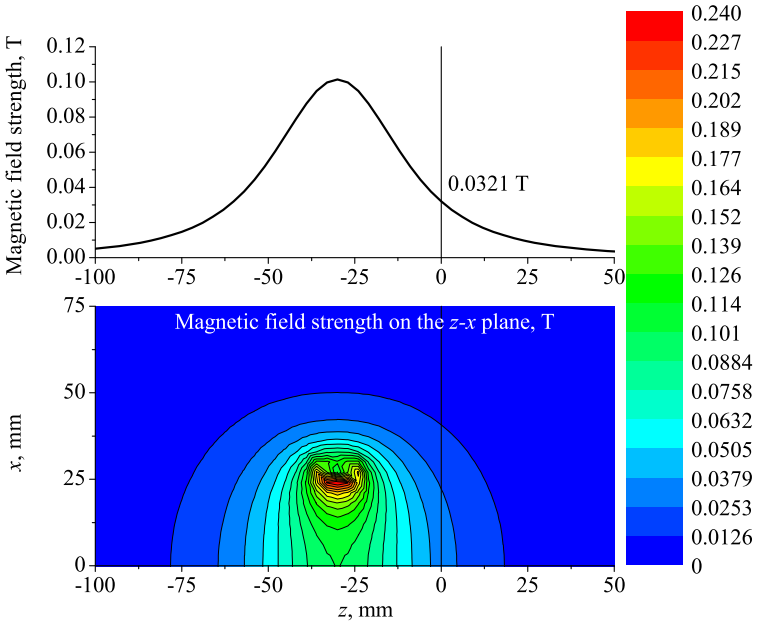

Figure 5.13: Calculated magnetic field strength produced by the edgewise coil at the peak current of 450 A. The magnetic field strength at the origin is 0.0321 T.

Table 5.1: Plasma conditions for original and modified cases.

	Original case	Modified case
Plasma radius, mm	9	9
Plasma mass, kg	6.9×10^{-8}	2.1×10^{-8}
Atomic mass, amu	6.5	6.5
<Atomic number>	1.25	0.5
Ion density, cm^{-3}	2.1×10^{18}	non-uniform
Kinetic energy, J	1.2	3.1
Ion expansion velocity	Maxwell distribution	non-uniform

5.4 Results and discussion

The ion expansion velocity was measured by the charge collector with a Faraday cup in the experiment and calculated by the modified and original numerical simulations. The values were derived by dividing the distance between the target and the probe (155 mm) by the arrival time of ion beam current.

In the experiment, the measured ion expansion velocity at B=0.0321 T is 199 km/s. The uncertainty in the time range at the oscilloscope is in the order of nanoseconds, so that the uncertainty in the measured velocity is negligible. In the original numerical simulation without considering the creation process of a laser-produced plasma, the velocity is calculated to be 15 km/s. The velocity obtained using the modified numerical simulation with considering the creation process is 194 km/s. Thus, the experimentally measured velocity and that calculated by the modified numerical simulation at B=0.0321 T are almost the same; that is, the initial plasma velocity for the modified numerical simulations is adequate for the experiment.

5.5 Summary

In this Chapter, we described ion expansion velocity of a laser-produced plasma in a magnetic field produced by a edgewise coil.

In the experiments at EUV database laser facility of ILE in the collaboration with Osaka University, to generate a magnetic field, a pulsed power supply and an edgewise coil were made. The ion expansion velocity was measured by using a charge collector with a Faraday cup. To confirm the validity of the modified numerical simulation, the results obtained using the modified numerical simulation were compared with those of experiments and the original numerical simulation. The modified numerical simulation compute high

energy laser injection onto a spherical target and the ablation plasma dynamics in a magnetic field. The measured ion expansion velocity at B=0.0321 T was 199 km/s. In the numerical simulations, the calculated velocity for the modified and original numerical simulations were 194 km/s and 15 km/s, respectively. Comparison of the ion expansion velocities revealed that the experiment and the modified numerical simulation at B=0.0321 T give almost the same ion expansion velocities. These results demonstrate that the modified numerical simulation can describe the ablation plasma dynamics in the magnetic field but the original numerical simulation does not. This confirms the validity of the modified numerical simulation.

The achievements in this Chapter are as follows.

Experiments

- In order to measure the ion beam current of a laser-produced plasma in a pulsed magnetic field, charge collector with a Faraday cup and pulsed power supply using a three-step PFN were made.
- By measuring the ion beam current was measured, the ion expansion velocity was estimated.

Numerical simulations

- The measured ion expansion velocity was compared with the calculated one.
- The experimentally measured velocity and that calculated by the modified numerical simulation are almost the same; that is, the initial plasma velocity for the modified numerical simulation is adequate for the experiment.

Bibliography

[1] Pearlman, J. S., "Faraday Cups for Laser Plasmas," *Rev. Sci. Instrum.*, Vol. 48, Issue 8, 1977, pp. 1064-1067. doi: 10.1063/1.1135184

[2] Sakawa, Y., Watanabe, D., Shibahara, D., Sugiyama K., and Tanabe, T., "Pulsed-laser Ablation of Co-deposits on JT-60 Graphite Tile," *J. Nuclear Materials*, Vol. 367370, 2007, pp. 1516-1521. doi: 10.1016/j.jnucmat.2007.04.014

[3] Ikeda, S., Nakajima, M., and Horioka, K., "Control of Laser Ablation Plasma with Longitudinal Magnetic Field," *Plasma Fusion Res.*, Vol. 7, 2012, 1201015. doi: 10.1585/pfr.7.1201015

[4] Nojiri, H., "パルス強磁場用小型コンデンサ電源の自作," *Solid State Physics*, Vol. 37, Issue 7, 2002, pp. 465-472. [In Japanese]

[5] Akiyama, H., 高電圧パルスパワー工学, EE Text Series, Ohmsha, Tokyo, 2003, Chaps. 10 and 11. [In Japanese]

[6] Minami, T., Funaki, I., Yamakawa, H., and Nakayama, Y., "Experimental Study of Magnetic Sails," ISAS Research Note 790, 2005. [In Japanese]

[7] Hayashi, I., "Formulas for Use in Calculating Electromagnetic Forces on the Cylindrical Air Core Coils and its Applications for the Power Reactors," *J. IEEJ*, Vol. 81, Issue 9, 1961, pp. 60-65. [In Japanese]

[8] 川崎昌二, “ロゴスキーコイルによる交流大電流測定,” 九州大学応用力学研究所技術レポート, Vol. 1, 2000, pp. 14-23. [In Japanese]

[9] Ohsawa, Y., “Relativistic Electromagnetic Particle Simulation,” *J. Plasma Fusion Res.*, Vol. 74, Issue 7, 1998, pp. 746-752. [In Japanese]

Chapter 6

Effect of magnetic field strength on impulse

6.1 Introduction

In the previous Chapters, it was brought up the differences between the modified and original numerical simulations, which are with and without considering the creation process of a laser-produced plasma for the impulse and ion expansion velocity under the same conditions of the magnetic field strength and geometry. It is considered that the initial plasma condition inputted into the 3D hybrid PIC code is important. In this Chapter, the details of the initial plasma condition affecting the impulse is analyzed by using the modified and original numerical simulations. Finally, the interaction between initial plasma condition and magnetic field strength is investigated.

6.2 Dependence on ion expansion velocity distribution in initial laser-produced plasma

6.2.1 Calculation model of 3D hybrid PIC code

The calculation model of 3D hybrid PIC code is shown in Fig. 6.1. The initial plasma is located at the center of model. The model is a $100\Delta x \times 100\Delta x \times 100\Delta x$ cube, where Δx=1 mm is the mesh width. The edgewise coil that generates the pulsed magnetic field is formed by winding five turns of a rectangular copper wire (width: 5 mm; thickness perpendicular to the coil axis: 1 mm; external diameter: 18 mm; internal diameter: 8 mm; length: 5 mm). The coil is set at a distance of 6.5 mm from the center. Figure 6.2 shows the magnetic field strength along the z-axis at $x = y = 0$ and in the $z - x$ plane at $y = 0$ produced by the coil at the peak current of 5.2 kA. The magnetic field strength at the center is 0.51 T. The calculation start time is set to 75 ns. The calculation time is $100{,}000\Delta t$, where Δt=50 ps (ion cyclotron frequency $\omega_{\rm ci}=1/2047\Delta t$) is the time step. The numerical simulation finishes at 5.075 μs. The number of particles is 1,000,000.

The plasma condition in Chap. 5 are used as the initial conditions for the calculations. The conditions are 3D distributions of ion super particle for the particle position, expansion velocity, charge state and mass. Table 6.1 lists the characteristic plasma conditions for the original and modified cases.

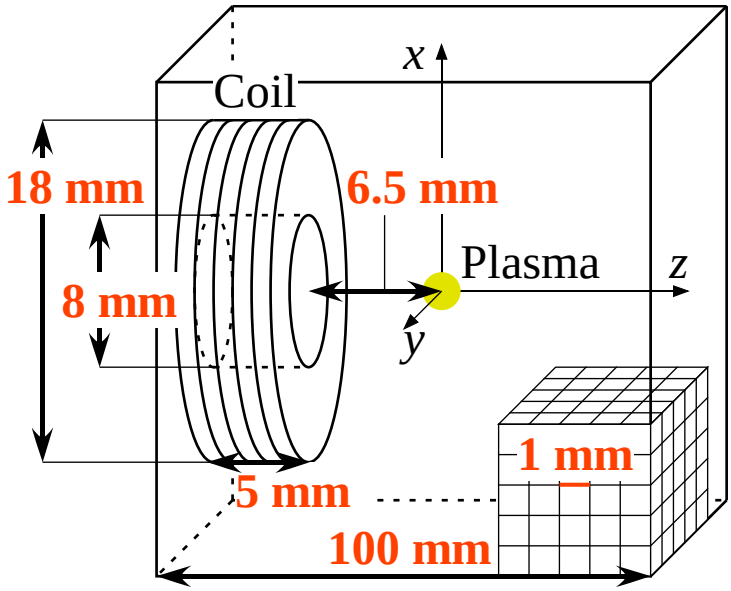

Figure 6.1: Cubic calculation model of 3D hybrid PIC code.

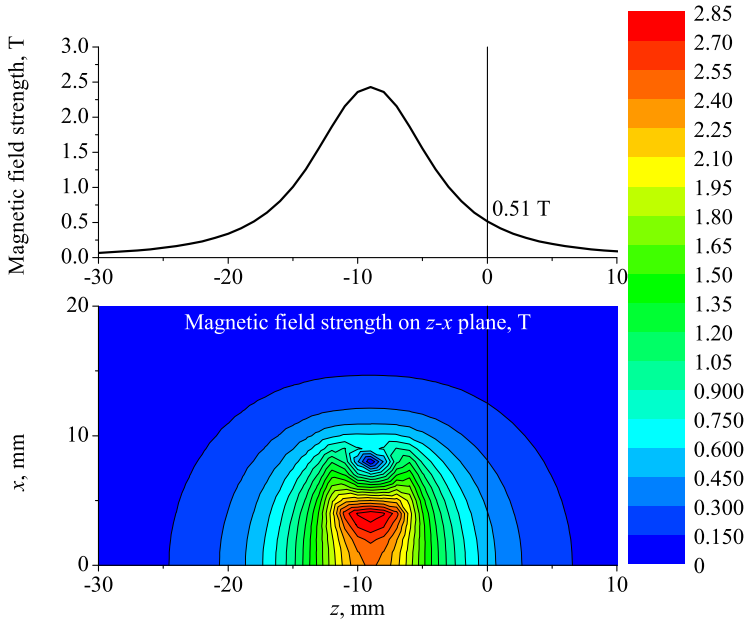

Figure 6.2: Calculated magnetic field strength produced by the edgewise coil when the peak current is 5.2 kA. The magnetic field strength at the center is 0.51 T.

Table 6.1: Plasma conditions for original and modified cases.

	Original case	Modified case
Plasma radius, mm	9	9
Plasma mass, kg	6.9×10^{-8}	2.1×10^{-8}
Atomic mass, amu	6.5	6.5
<Atomic number>	1.25	0.5
Ion density, cm^{-3}	2.1×10^{18}	non-uniform
Kinetic energy, J	1.2	3.1
Ion expansion velocity	Maxwell distribution	non-uniform

6.2.2 Results and discussion

Diamagnetic cavity

Figures 6.3 and 6.4 show the distribution of the magnetic field strength in the $z-x$ plane at $y=0$ at calculation times of 325, 575, 825 ns, 1.075, 1.325, 1.575, 3.075 and 3.575 μs for the original case. Comparison with the initial magnetic field shown in Fig. 6.2 reveals that the magnetic field disappears inside the area indicated by the red circle in Fig. 6.3(a). The diamagnetic current in a laser-produced plasma forms a diamagnetic cavity. Figures 6.3 and 6.4 show that the magnetic field returns to the initial magnetic field up to 3.575 μs and the cavity moves in the $+z$ direction for pushing plasma back.

Figure 6.5 shows the distribution of the magnetic field strength in the $z-x$ plane at $y=0$ at calculation times of 1.325, 2.575, 3.825 and 5.075 μs for the modified case. The distribution does not change from 75 ns to 1.325 μs. Comparison with the initial magnetic field shown in Fig. 6.2 reveals that the magnetic field disappears inside the area indicated by the red circle in Fig. 6.5(a). The diamagnetic current in a laser-produced plasma forms a diamagnetic cavity. Figure 6.5 shows that the magnetic field returns to the initial magnetic field up to 5.075 μs and the cavity moves in the $+z$ direction for pushing the plasma back.

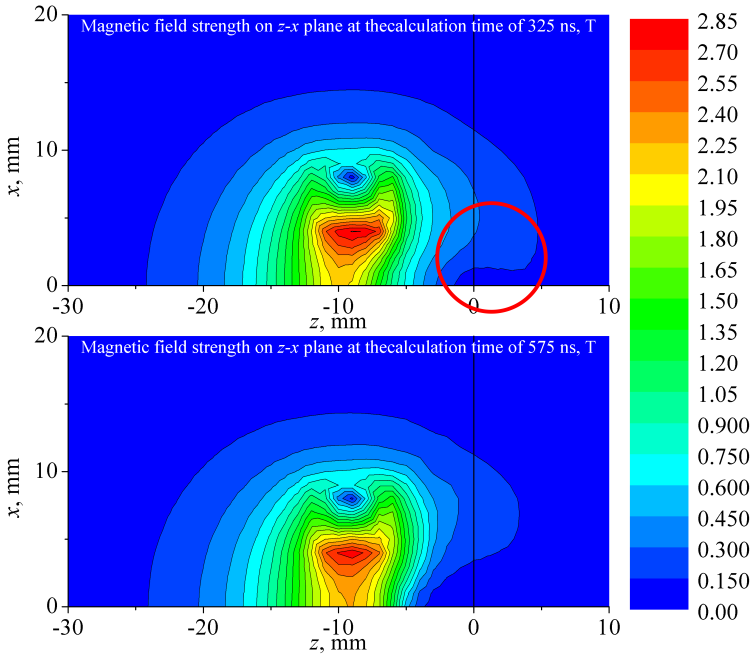

(a) 325 ns & 575 ns

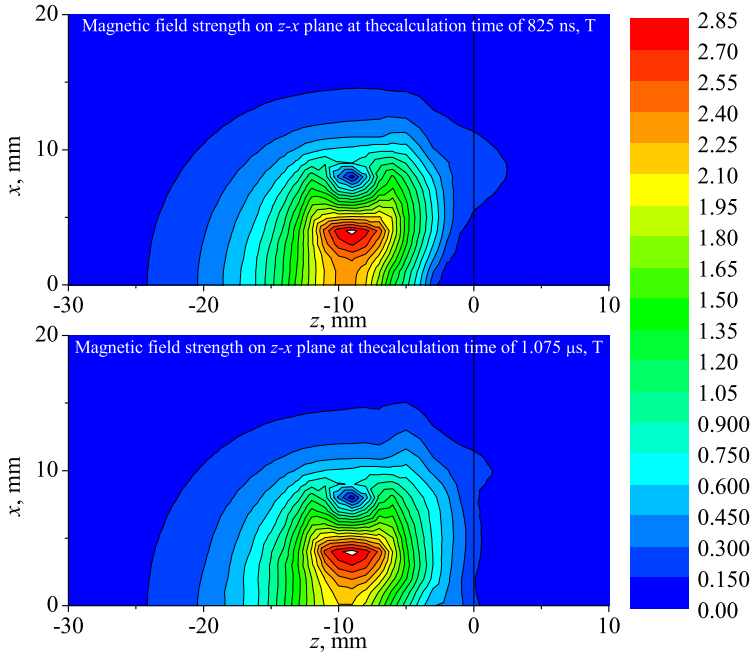

(b) 825 ns & 1.075 μs

Figure 6.3: Magnetic field strength distribution for the original case in $z-x$ plane at $y = 0$ for calculation times of 325, 575, 825 ns, and 1.075 μs. A diamagnetic cavity is formed.

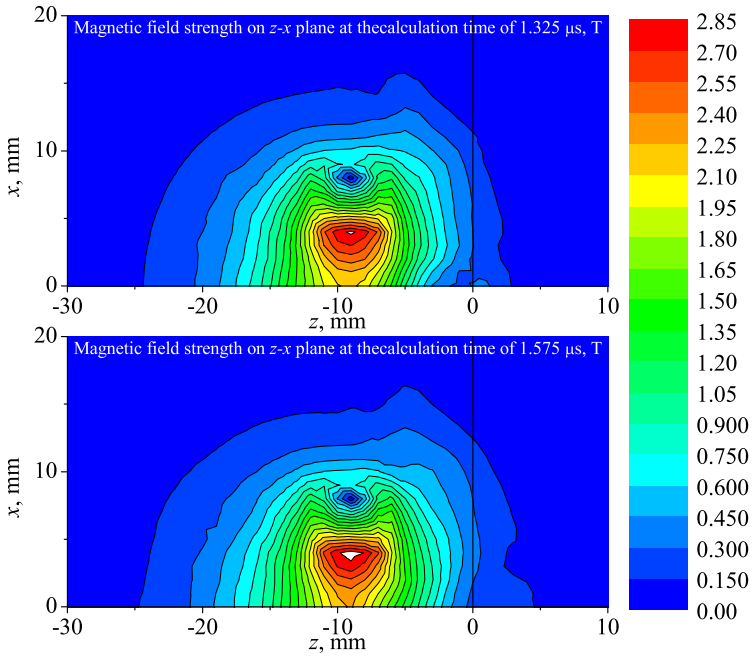

(a) 1.325 μs & 1.575 μs

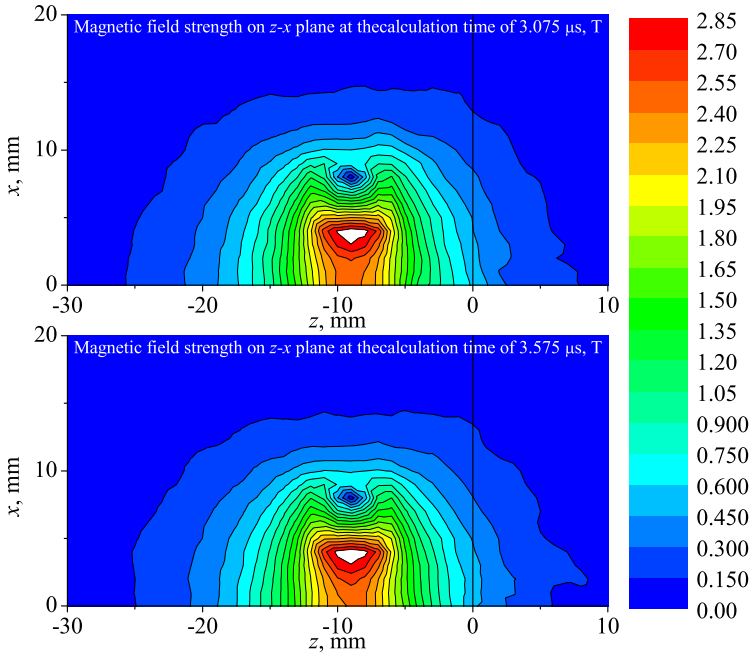

(b) 3.075 μs & 3.575 μs

Figure 6.4: Magnetic field strength distribution for the original case in $z-x$ plane at $y = 0$ for calculation times of 1.325, 1.575, 3.075, and 3.575 μs. A diamagnetic cavity is formed.

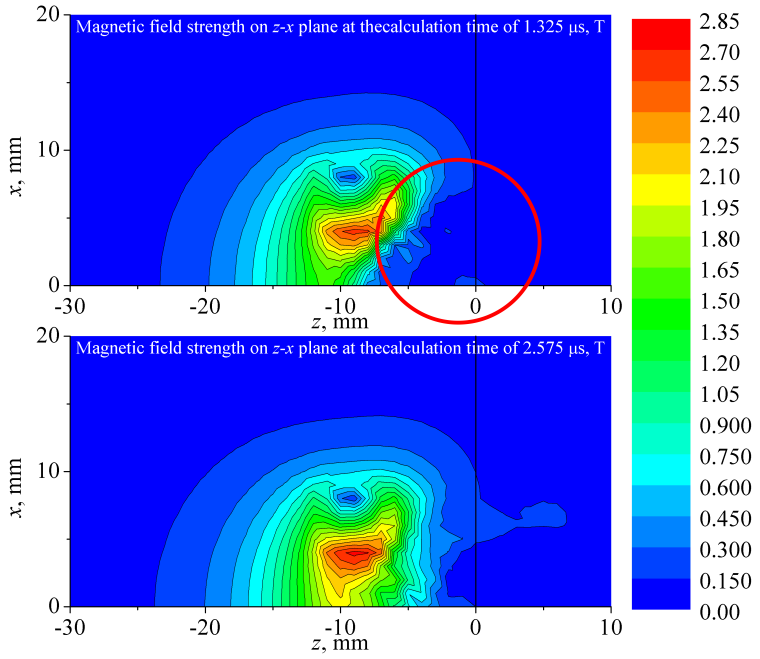

(a) 1.325 μs & 2.575 μs

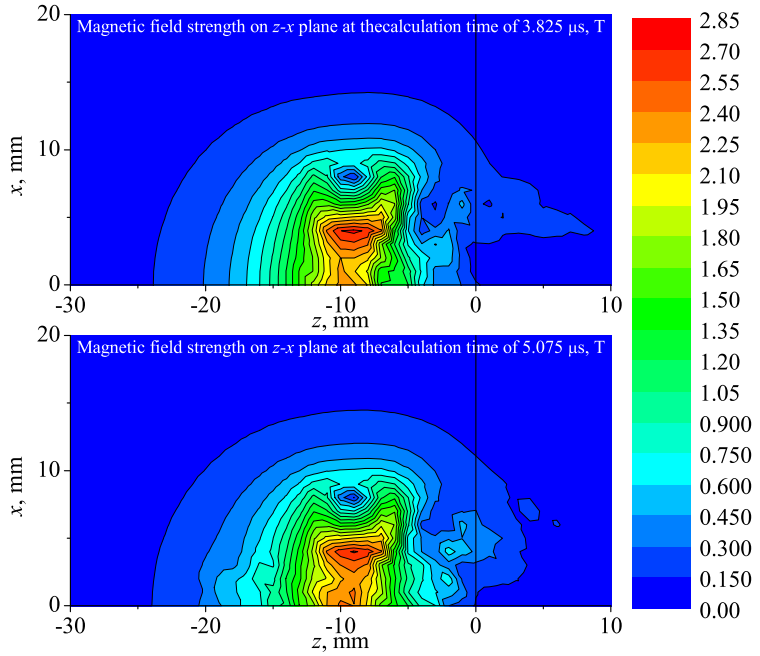

(b) 3.825 ns & 5.075 μs

Figure 6.5: Magnetic field strength distribution for the modified case in $z-x$ plane at $y = 0$ for calculation times of 1.325, 2.575, 3.825, and 5.075 μs. A diamagnetic cavity is formed.

Thrust energy and impulse

The efficiencies in terms of the kinetic energy η_{kin} and momentum η_{Ibit} are calculated using Eqs. (6.1) and (6.2), where $v_{\pm z}$ is the velocity of a super particle which moves in the $\pm z$ direction. Ibit stands for impulse bit (impulse per pulse). The sums are performed over all super particles. Figure 6.6 shows the time evolutions of the thrust energy and impulse for the original and modified cases.

$$\eta_{\mathrm{kin}} = \frac{\sum \frac{1}{2} m_{\mathrm{i}} v_{+z}^2 - \sum \frac{1}{2} m_{\mathrm{i}} v_{-z}^2}{\sum \frac{1}{2} m_{\mathrm{i}} v_0^2} \tag{6.1}$$

$$\eta_{\mathrm{Ibit}} = \frac{\sum m_{\mathrm{i}} v_z - \sum m_{\mathrm{i}} v_{z0}}{\sum m_{\mathrm{i}} |v_{z0}|} \tag{6.2}$$

For the original case, the thrust energy increases gradually up to 3 μs, after which it saturates at 0.36 J; the final efficiency η_{kin} is 31%. In a similar fashion, the impulse increases and saturates at 151 μNs; the final efficiency η_{Ibit} is 41%. For the modified case, the thrust energy increases rapidly up to 200 ns, after which it saturates at 0.37 J (12%). In a similar fashion, the impulse increases and saturates at 31.6 μNs (41%). Figure 6.6 indicates that the direction of movement of many super particles is changed in the $+z$ direction by the magnetic field of the coil, as shown in Figs. 6.3, 6.4 and 6.5. The time-variable magnetic field, thrust energy, and impulse for the two cases exhibit a time difference.

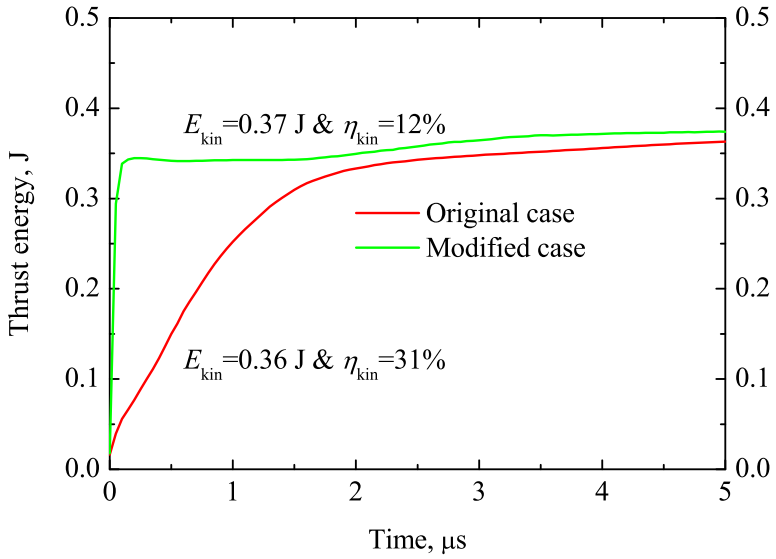

(a) Thrust energy

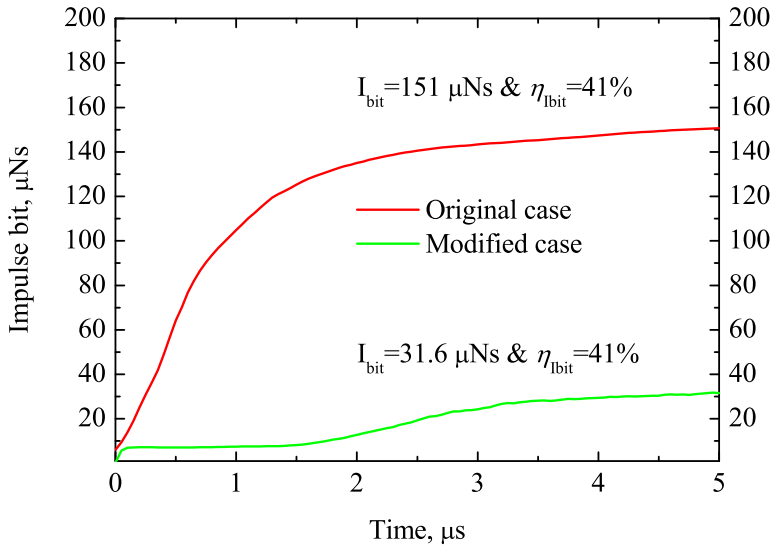

(b) Impulse

Figure 6.6: Time evolutions of thrust energy and impulse. For the original case, thrust energy and impulse saturate at 0.36 J (31%) and 151 μNs (41%), respectively. For the modified case, thrust energy and impulse saturate at 0.37 J (12%) and 31.6 μNs (41%), respectively.

Discussion

When the Larmor radius is shorter than the coil radius, it is considered that the charged particles move in the $+z$ direction effectively. The threshold of the Larmor radius is set as 5 mm which is a bit larger than the internal radius of the edgewise coil. The region of slow expansion velocity in the range 0-20 km/s is focused using the threshold. In this region, the charge state and ion density are almost same for the two cases.

For the original case, most initial plasma is in the region of slow expansion velocity. For the modified case, the initial plasma can be divided into two groups: group A that has a slow expansion velocity (kinetic energy: 0.027 J), and group B that has a fast expansion velocity in the range 20-175 km/s (kinetic energy: 3.0 J). Figure 6.7 shows the thrust energy and impulse of these groups. For the group B as shown in Fig. 6.7(b), the thrust energy and impulse increase rapidly up to 200 ns, after which they saturate at 0.34 J (11%) and 7.5 μNs (14%), respectively. The group B forms the diamagnetic cavity but it does not contribute the impulse. For group A as shown in Fig. 6.7(a), the thrust energy and impulse increase slowly up to 1.5 μs, after which they saturate at 0.0337 J (125%) and 24.1 μNs (102%), respectively. Thus, the group A contributes the impulse efficiently. The reason for the high efficiency is that the group A moves in the diamagnetic cavity formed by the group B and pushed back by the diamagnetic cavity.

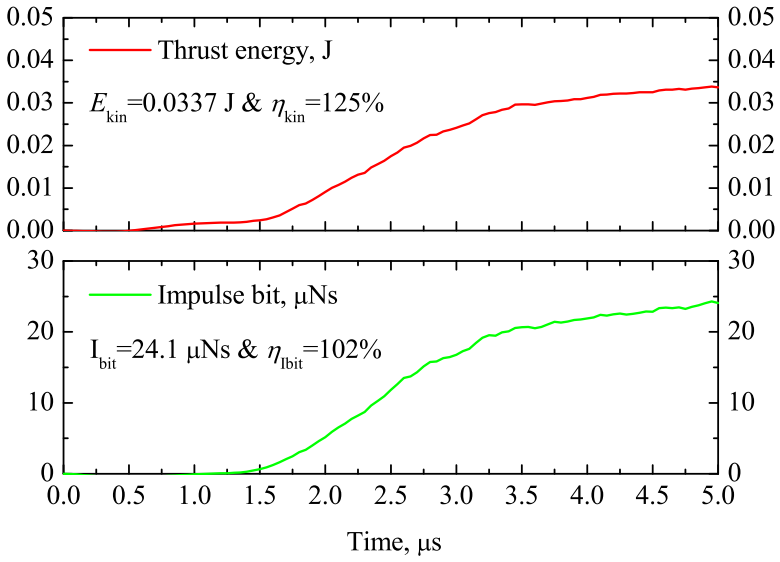

(a) Slow velocity group

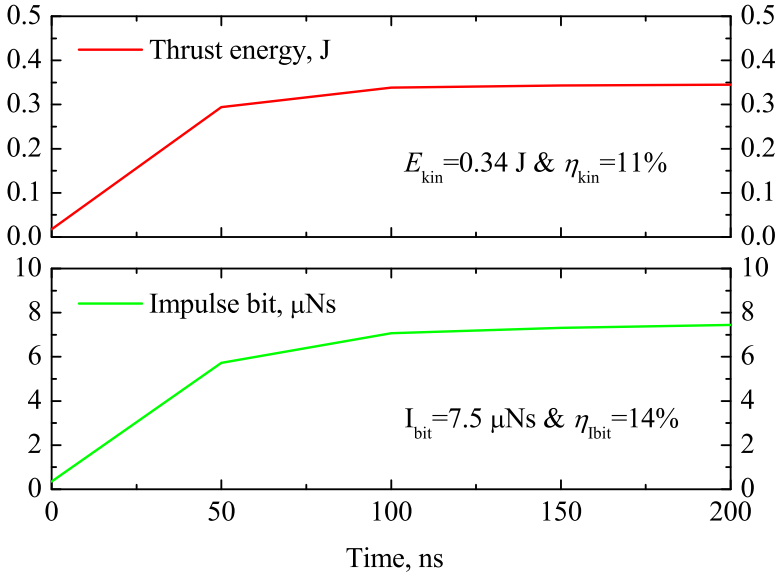

(b) Fast velocity group

Figure 6.7: Time evolutions of thrust energy and impulse for (a) slow velocity group and (b) fast velocity group. For group A, thrust energy and impulse saturate at 0.0337 J (125%) and 24.1 μNs (102%). For group B, thrust energy and impulse saturate at 0.34 J (11%) and 7.5 μNs (14%), respectively.

6.3 Thrust performances for various magnetic field strengths

6.3.1 Numerical simulation conditions

In the experiment of Chap. 5, an impulse due to the interaction between a diamagnetic current in a laser-produced plasma and a magnetic field generated by an edgewise coil has been measured by using a torsional thrust stand. However, the level of the impulse has been lower than the detection limit of a torsional thrust stand. This is considered that the magnetic field strength of the experiment (B=0.0321 T) has been too weak. When the magnetic field strength is sufficiently high, the impulse should increase. Calculations were conducted at the origin of stronger magnetic field, which strengths are B=0.0321, 0.961, 1.92, and 2.88 T.

6.3.2 Results and discussion

Figures 6.8-6.11 show the ion super particle distributions at a calculation time of 5.075 μs in the $z-x$ plane at $y = 0$ for various magnetic fields calculated by the two numerical simulations. They show the effect of the magnetic field strength in the magnetic thrust chamber system for LFR. The squares in the figures indicate the edgewise coil.

For the modified case, most particles of B=0.0321 T are expanding isotropically, while the other particles are excluded by colliding the edgewise coil as shown in Fig. 6.8(a). This indicates that the interaction between the particles and the magnetic field is too weak to generate the impulse. Then, Figs. 6.9(a), 6.10(a) and 6.11(a) show that the directions of particles movement are limited along z-axis with increasing magnetic field strength. The particles move in the exhaust direction with anisotropic expansion. Thus, the impulse is predicted to be improved by increasing the magnetic field strength.

The reason for this is considered that the particles of fast expansion velocity are interacting with the magnetic field and the Larmor radius is decreasing with increasing the strength. This indicates that the interaction between the particles and the magnetic field is stronger with increasing the strength.

For the original case, Figs. 6.8(b), 6.9(b), 6.10(b) and 6.11(b) show that the particles are guided by the magnetic field through the edgewise coil. The particle distribution at B=0.961 T shown in Fig. 6.9(b) is similar to the results for B=1.92 T shown in Fig. 6.10(b) and for B=2.88 T shown in Fig. 6.11(b). The directions of particles movement are limited enough along z-axis. This suggests that the impulse will saturate at magnetic field strengths greater than B=0.961 T.

Figure 6.12 shows the impulses calculated by the modified and original numerical simulations. As the ion super particle distributions in Figs. 6.8-6.11 show, the impulse in the modified numerical simulation increases with increasing magnetic field strength from B=0.961 T, whereas the impulse in the original numerical simulation saturates at high magnetic field strengths. The reason for this proportion relation between the magnetic field strength and the impulse is that the diamagnetic cavity which increases with increasing the magnetic field strength interacts more with the particles of slow expansion velocity. Therefore, it is revealed that the impulse increases with increasing magnetic field strength and saturates at higher magnetic field strength.

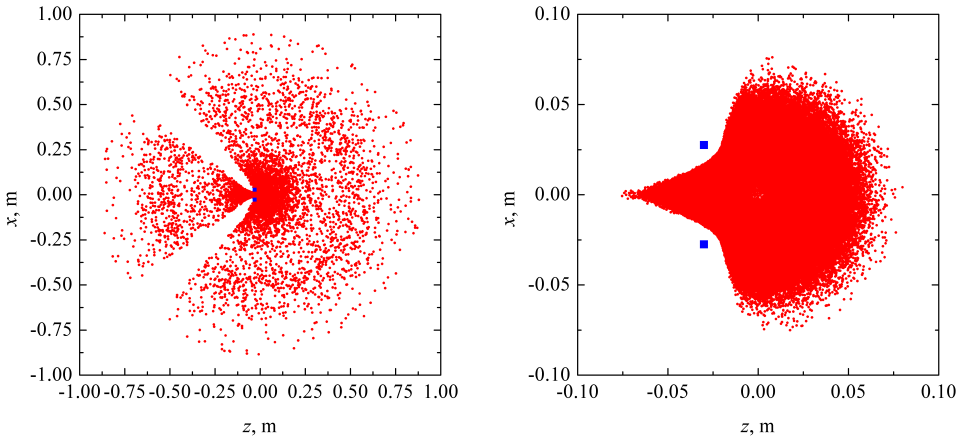

(a) Modified case. (b) Original case.

Figure 6.8: Ion super particle distributions at B=0.0321 T calculated by modified and original numerical simulations.

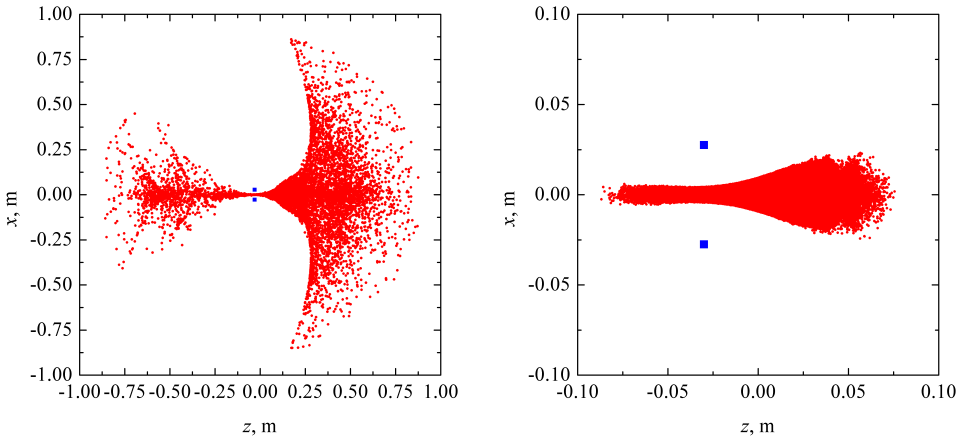

(a) Modified case. (b) Original case.

Figure 6.9: Ion super particle distributions at B=0.961 T calculated by modified and original numerical simulations.

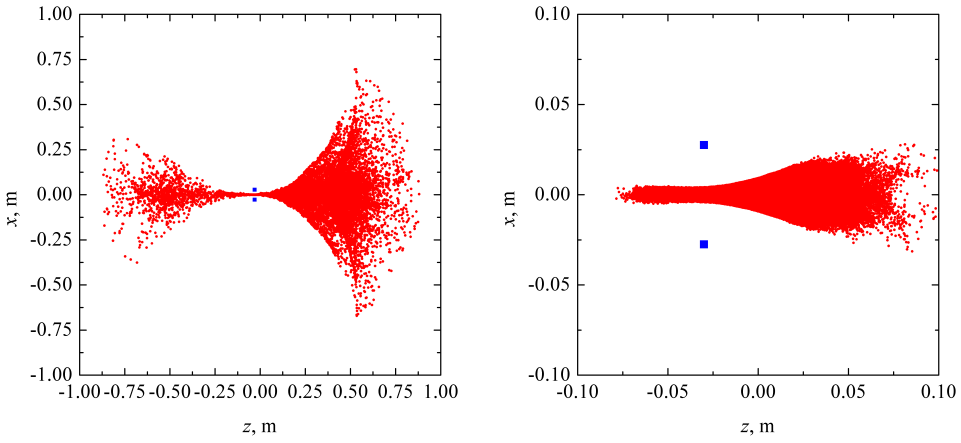

(a) Modified case. (b) Original case.

Figure 6.10: Ion super particle distributions at B=1.92 T calculated by modified and original numerical simulations.

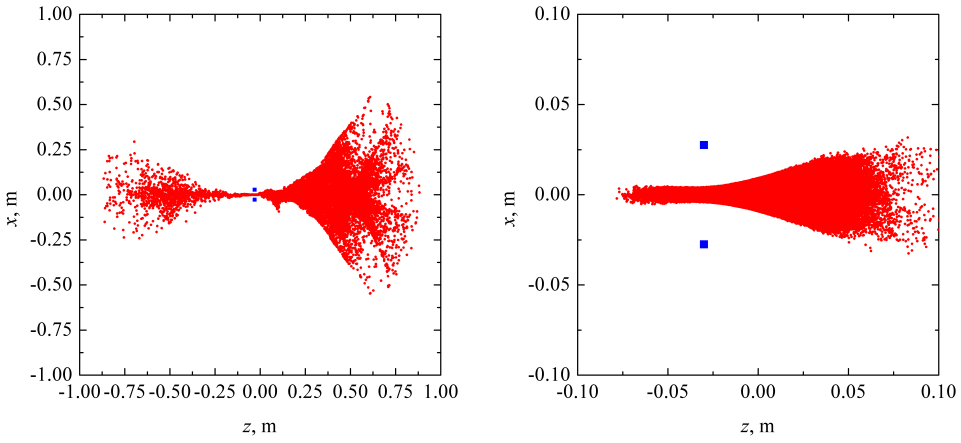

(a) Modified case. (b) Original case.

Figure 6.11: Ion super particle distributions at B=2.88 T calculated by modified and original numerical simulations.

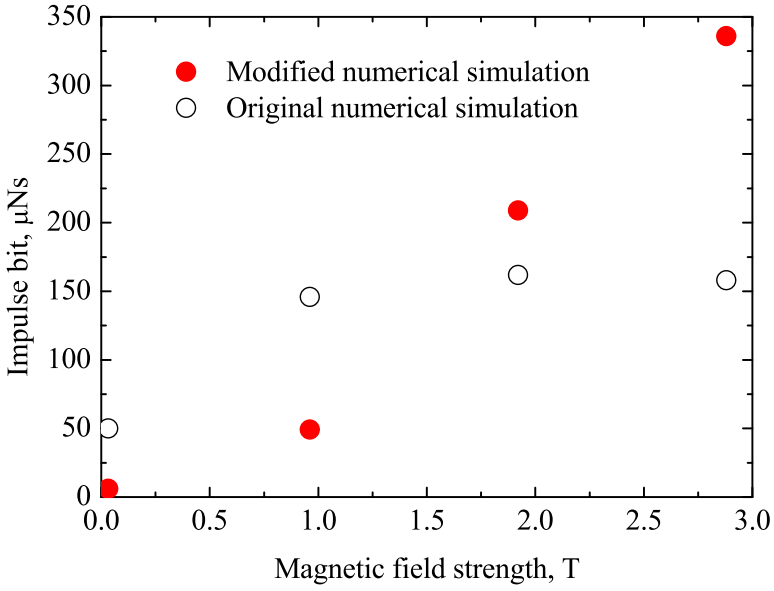

Figure 6.12: Impulse for various magnetic field strengths calculated by modified and original numerical simulations.

6.4 Summary

In this Chapter, we described the dependences of the interaction between initial laser-produced plasma property and magnetic field strength by comparing the two numerical simulations. The following results were obtained.

- The particles of slow expansion velocity contributes the impulse efficiently. The reason for the high efficiency is that the diamagnetic cavity produced by the particles of fast expansion velocity interact with the particles of slow expansion velocity.
- Calculations of the impulse reveal that the impulse increases with increasing magnetic field strength and saturates at higher magnetic field strength.

Chapter 7

Summary

In this study, the followings are conducted to study the magnetic thrust chamber system for LFR.

1. The direct measurement of the impulse due to the interaction between a diamagnetic current and a magnetic field has not been demonstrated experimentally yet. To produce the impulse by using laser-produced plasma and magnet, we attempt to conduct experiments in the actual research laboratory instead of ICF plasma and SCM. The experiments are conducted for various laser pulse energies at Extreme Ultra-Violet (EUV) database and Gekko XII (GXII) laser facilities of Institute of Laser Engineering (ILE) in the collaboration with Osaka University.

2. The creation process of a laser-produced plasma has not sufficiently been considered in the numerical simulation yet. This process is needed to compare numerical simulations with experiments in the actual research laboratory. By combining a 3D hybrid PIC code with a one-dimensional (1D) Lagrangian radiation hydrodynamic code which can compute the hydrodynamic evolution of radiating plasma heated by laser pulses, we attempt to compute high energy laser injection onto a spherical target and the ablation plasma dynamics in a magnetic field.

3. To find the scaling law of the magnetic thrust chamber system, it is necessary to confirm the validity of the numerical simulation. In order to validate the modified numerical simulation with considering the creation process, the experimental results are compared with these of the numerical simulations which are with and without considering the creation process of a laser-produced plasma.

As a result, the achievements in this study are obtained as follows.

- By using cylindrical neodymium permanent magnet and non-magnetized iron cylinder, impulse due to the interaction between a diamagnetic current in a laser-produced plasma and a magnetic field was generated and the magnetic thrust chamber system for LFR was demonstrated experimentally to work as theory tells.

- The modified numerical simulation with considering the creation process of a laser-produced plasma as the initial plasma conditions of the 3D hybrid PIC code was performed. The modified numerical simulation can describe the ablation plasma dynamics in the magnetic field but the original numerical simulation does not. This confirms the validity of the modified numerical simulation.

- The experimentally measured velocity and that calculated by the modified numerical simulation are almost the same; that is, the initial plasma velocity for the modified numerical simulation is adequate for the experiment.

- In order to produce large impulse, longer pulse durations, shorter wavelengths and higher energies are better.

- Calculations of the impulse reveal that the impulse increases with increasing magnetic field strength and saturates at higher magnetic field strength.

- The particles of slow expansion velocity contributes the impulse efficiently. The reason for the high efficiency is that the diamagnetic cavity produced by the particles of fast expansion velocity interact with the particles of slow expansion velocity.

Then, the magnetic thrust chamber system for LFR is demonstrated experimentally to work as theory tells. In addition to that, the modified numerical simulation with considering the creation process of a laser-produced plasma as the initial plasma conditions of the 3D hybrid PIC code can determine the ablation plasma dynamics in the magnetic field more accurately than the original numerical simulation. Finally, the dependences of the impulse on the laser parameters and initial conditions are obtained in order to improve the thrust performance of the magnetic thrust chamber system for LFR.

The suggestions for the further work are as follows.

- Under the guidances obtained in this study for improving the thrust performance of the magnetic thrust chamber system for LFR, we are planning to conduct experiments and numerical simulation of the system. In addition to that, it is also necessary to consider how to create the optimal laser-produced plasma for the system in the experiments.

- The modified numerical simulation can describe the ablation plasma dynamics in the magnetic field but the original numerical simulation does not. This confirms the validity of the modified numerical simulation. However, there is the discrepancy between measured and calculated values. The reason for the discrepancy is considered to be due to the calculation assumptions in Star-1D and the 3D hybrid PIC code. Star-1D assumes that a laser-produced plasma expands into the vacuum isotropically. However, in the experiments, the plasma created by a single laser beam is ablating in one direction. This is considered that

the ablation plasma on the opposite surface of laser injection is not calculated well in the modified numerical simulation. This difference of plasma ablation may affect initial plasma property. Then, we must use a 2D radiation hydrodynamic code which can compute the axial symmetry hydrodynamic evolution of radiating plasma heated by laser pulses.

- Because it is impossible to conduct experiment using ICF plasma and SCM in several decades, to investigate the magnetic thrust chamber system of LFR is proceeding by computing high energy laser injection onto a ICF target and the ablation plasma dynamics in a magnetic field produced by SCM.

Acknowledgments

I would like to express the deepest appreciation to my doctoral advisors, Professor Hideki Nakashima, Professor Kazuo Nakamura, Professor Kiichiro Uchino, and Associate Professor Naoji Yamamoto.

I would like to express the appreciation to my advisers, Dr. Atsushi Sunahara of Institute for Laser Technology, Dr. Tomoyuki Johzaki of Hiroshima University, Dr. Yoshihiro Kajimura of Akashi National College of Technology, Dr. Shinsuke Fujioka of Osaka University, and Yoshitaka Mori of The Graduate School for the Creation of New Photonics Industries. I would like to appreciate Megumi Oogami, Kazuyo Mine, Mieko Inoue, and Takako Mawatari who take care of my various paperwork.

I would like to thank my junior labmates whose work about my research theme together, Masato Yasunaga, Tomoyuki Hinaga, Yasuma Hidehira, Hiroshi Tominaga and Yudai Miwa. In addition, I thank my junior labmates of Kyushu University, Yusuke Nakamura, Kenji Hirano, Naruya Hiroike, Yutaro Sasagawa, Yuji Toyoda, Yuta Tajiri, Hiroshi Umishio, Shouhei Araki, Kohei Nagaoka, Shouta Maeda, Yuki Sakamoto and Keisuke Kataoka.

This work was supported by the Japan Society for the Promotion of Science (JSPS) KAKENHI (Grant Number 21360418) and Grant-in-Aid for JSPS Fellows (Grant Number 22-1672) and Collaboration Research with the Institute of Laser Engineering at Osaka University since 2008.

Finally, I would like to express the deepest gratitude to my friends, my family and my precious one for their kind support and help.

Appendix A

Ampere's law with Darwin approximation

Here, we derive Ampere's law with Darwin approximation. Equation (A.1) is Gauss's law for magnetism, where $\boldsymbol{B}$ is magnetic field.

$$\nabla \cdot \boldsymbol{B} = 0 \tag{A.1}$$

Because magnetic field is solenoidal field, magnetic field is expressed by vector potential $\boldsymbol{A}$ (i.e., $\nabla \cdot \boldsymbol{A} = 0$).

$$\boldsymbol{B} = \nabla \times \boldsymbol{A} \tag{A.2}$$

Equation (A.3) is Maxwell-Faraday equation, where $\boldsymbol{E}$ is electric field.

$$\nabla \times \boldsymbol{E} = -\frac{\partial \boldsymbol{B}}{\partial t} \tag{A.3}$$

By substituting Eq. (A.2) into Eq. (A.3), the following equation is obtained.

$$\nabla \times \left(\boldsymbol{E} + \frac{\partial \boldsymbol{A}}{\partial t} \right) = 0 \tag{A.4}$$

Electric field is expressed as follows by using Eq. (A.4) and scalar potential ϕ (i.e., $\nabla \times \nabla\phi = 0$).

$$\boldsymbol{E} = -\nabla\phi - \frac{\partial \boldsymbol{A}}{\partial t} \tag{A.5}$$

Equation (A.6) is Ampere's law, where $\boldsymbol{j}$ is current density, μ_0 is the permeability of vacuum and ε_0 is the permittivity of vacuum.

$$\nabla \times \boldsymbol{B} = \mu_0 \left(\boldsymbol{j} + \varepsilon_0 \frac{\partial \boldsymbol{E}}{\partial t} \right) \tag{A.6}$$

By substituting Eq. (A.5) into Eq. (A.6), the following equation is obtained.

$$\nabla \times \boldsymbol{B} = \mu_0 \left(\boldsymbol{j} - \varepsilon_0 \nabla \frac{\partial \phi}{\partial t} \right) - \frac{1}{c^2} \frac{\partial^2 \boldsymbol{A}}{\partial t^2} \tag{A.7}$$

The first and second terms on r.h.s of Eq. (A.7) have the order of $(v/c)^2$ and $(v/c)^3$, respectively. When the speed of light c $(= 1/\mu_0\varepsilon_0)$ is more faster than plasma velocity, the second term on r.h.s. of Eq. (A.7) is neglected. Darwin approximation means to neglect the transverse displacement current. Ampere's law with Darwin approximation is given as shown in Eq. (A.8).

$$\nabla \times \boldsymbol{B} = \mu_0 \left(\boldsymbol{j} - \varepsilon_0 \nabla \frac{\partial \phi}{\partial t} \right) \tag{A.8}$$

Current density is separeted to the density of solenoidal field $\boldsymbol{j}_\mathrm{r}$ (i.e., $\nabla \times \boldsymbol{j}_\mathrm{r} = 0$) and that of potential field $\boldsymbol{j}_\mathrm{d}$. Equation (A.9) is obtained by the curl of Eq. (A.8) and the relationship between curl and gradient (i.e., $\nabla \times \nabla\phi = 0$).

$$\nabla \times (\nabla \times \boldsymbol{B}) = \nabla \times \mu_0 \boldsymbol{j} - \nabla \times \left(\frac{1}{c^2} \nabla \frac{\partial \phi}{\partial t} \right)$$

$$= \mu_0 \nabla \times (\boldsymbol{j}_\mathrm{r} + \boldsymbol{j}_\mathrm{d})$$

$$\nabla \times \boldsymbol{B} = \mu_0 \boldsymbol{j}_\mathrm{d} \tag{A.9}$$

By substituting Eq. (A.5) into Eq. (A.8), the following equation is obtained.

$$\nabla \times \boldsymbol{B} = \mu_0 \left\{ \boldsymbol{j} + \varepsilon_0 \frac{\partial}{\partial t} \left(\boldsymbol{E} + \frac{\partial \boldsymbol{A}}{\partial t} \right) \right\} \tag{A.10}$$

Electric field is separeted to the part of solenoidal field $\boldsymbol{E}_\mathrm{r}$ and that of potential field $\boldsymbol{E}_\mathrm{d}$ (i.e., $\nabla \cdot \boldsymbol{E}_\mathrm{d} = 0$). By using Eqs. (A.9) and the divergence of (A.10), the following equation is obtained.

$$\nabla \cdot (\nabla \times \boldsymbol{B}) = \mu_0 \left\{ \nabla \cdot \boldsymbol{j} + \varepsilon_0 \frac{\partial}{\partial t} (\nabla \cdot \boldsymbol{E} + \nabla \cdot \frac{\partial \boldsymbol{A}}{\partial t}) \right\}$$

$$0 = \nabla \cdot \left(\mu_0 \boldsymbol{j}_\mathrm{r} + \frac{1}{c^2} \frac{\partial \boldsymbol{E}_\mathrm{r}}{\partial t} \right) \tag{A.11}$$

Equation (A.12) is Gauss's law, where ρ is charge density. Here, it is assumed to be quasi-neutrality (ρ is constant).

$$\nabla \cdot \boldsymbol{E} = \frac{\rho}{\varepsilon_0} \tag{A.12}$$

By differenting partially both sides of Eq. (A.12), Eq. (A.13) is given.

$$\nabla \cdot \frac{\partial \boldsymbol{E}}{\partial t} = \nabla \cdot \frac{\partial \boldsymbol{E}_\mathrm{r}}{\partial t} = 0 \tag{A.13}$$

By substituting Eq. (A.11) into Eq. (A.13), $\nabla \cdot \boldsymbol{j}_{\mathrm{r}} = 0$ is obtained, that is, $\boldsymbol{j}_{\mathrm{r}} = 0$. Thus, $\boldsymbol{j} = \boldsymbol{j}_{\mathrm{d}}$. The Ampere's law with Darwin approximation is expressed as follows, where $\boldsymbol{j}_{\mathrm{i}}$ is the ion current density and $\boldsymbol{j}_{\mathrm{e}}$ is the electron current density.

$$\nabla \times \boldsymbol{B} = \mu_0(\boldsymbol{j}_{\mathrm{i}} + \boldsymbol{j}_{\mathrm{e}})$$

Appendix B

Components of matrix equations

B.1 x component of $\boldsymbol{v}_{\mathrm{i}}^{n+\frac{1}{2}}$

We derive x component of $\boldsymbol{v}_{\mathrm{i}}^{n+\frac{1}{2}}$ for Eq. (3.18) in the Chapter 3. This is much of the same for $v_{\mathrm{i}y}^{n+\frac{1}{2}}$ and $v_{\mathrm{i}z}^{n+\frac{1}{2}}$.

$$m_{\mathrm{i}}^{n}\frac{\mathrm{d}\boldsymbol{v}_{\mathrm{i}}^{n}}{\mathrm{d}t} = Z^{n}e\left(\boldsymbol{E}^{n} + \boldsymbol{v}_{\mathrm{i}}^{n}\times\boldsymbol{B}^{n} - \frac{\eta}{\mu_{0}}\nabla\times\boldsymbol{B}^{n}\right) \tag{B.1}$$

$$\frac{\mathrm{d}\boldsymbol{v}_{\mathrm{i}}^{n}}{\mathrm{d}t} = \frac{\boldsymbol{v}_{\mathrm{i}}^{n+\frac{1}{2}} - \boldsymbol{v}_{\mathrm{i}}^{n-\frac{1}{2}}}{\Delta t} \tag{B.2}$$

By substituting Eq. (B.2), $\boldsymbol{v}_{\mathrm{i}}^{n+\frac{1}{2}}(v_{\mathrm{i}x}^{n+\frac{1}{2}}, v_{\mathrm{i}y}^{n+\frac{1}{2}}, v_{\mathrm{i}z}^{n+\frac{1}{2}})$, $\boldsymbol{B}^{n}(B_{x}^{n}, B_{y}^{n}, B_{z}^{n})$ and $\boldsymbol{E}^{n}(E_{x}^{n}, E_{y}^{n}, E_{z}^{n})$ into Eq. (B.1), the following equation is obtained.

$$\frac{m_{\mathrm{i}}^n}{\Delta t}\begin{pmatrix} v_{\mathrm{i}x}^{n+\frac{1}{2}} - v_{\mathrm{i}x}^{n-\frac{1}{2}} \\ v_{\mathrm{i}y}^{n+\frac{1}{2}} - v_{\mathrm{i}y}^{n-\frac{1}{2}} \\ v_{\mathrm{i}z}^{n+\frac{1}{2}} - v_{\mathrm{i}z}^{n-\frac{1}{2}} \end{pmatrix}$$
$$= Z^n e \begin{pmatrix} E_x^n \\ E_y^n \\ E_z^n \end{pmatrix} + Z^n e \begin{pmatrix} v_{\mathrm{i}y}^n B_z^n - v_{\mathrm{i}z}^n B_y^n \\ v_{\mathrm{i}z}^n B_x^n - v_{\mathrm{i}x}^n B_z^n \\ v_{\mathrm{i}x}^n B_y^n - v_{\mathrm{i}y}^n B_x^n \end{pmatrix} - \frac{\eta Z^n e}{\mu_0} \begin{pmatrix} \frac{\partial B_z^n}{\partial y} - \frac{\partial B_y^n}{\partial z} \\ \frac{\partial B_x^n}{\partial z} - \frac{\partial B_z^n}{\partial x} \\ \frac{\partial B_y^n}{\partial x} - \frac{\partial B_x^n}{\partial y} \end{pmatrix}$$

$$\begin{pmatrix} v_{\mathrm{i}x}^{n+\frac{1}{2}} \\ v_{\mathrm{i}y}^{n+\frac{1}{2}} \\ v_{\mathrm{i}z}^{n+\frac{1}{2}} \end{pmatrix} - \frac{Z^n e \Delta t}{2 m_{\mathrm{i}}^n} \begin{pmatrix} v_{\mathrm{i}y}^{n+\frac{1}{2}} B_z^n - v_{\mathrm{i}z}^{n+\frac{1}{2}} B_y^n \\ v_{\mathrm{i}z}^{n+\frac{1}{2}} B_x^n - v_{\mathrm{i}x}^{n+\frac{1}{2}} B_z^n \\ v_{\mathrm{i}x}^{n+\frac{1}{2}} B_y^n - v_{\mathrm{i}y}^{n+\frac{1}{2}} B_x^n \end{pmatrix}$$
$$= \begin{pmatrix} v_{\mathrm{i}x}^{n-\frac{1}{2}} \\ v_{\mathrm{i}y}^{n-\frac{1}{2}} \\ v_{\mathrm{i}z}^{n-\frac{1}{2}} \end{pmatrix} + \frac{Z^n e \Delta t}{m_{\mathrm{i}}^n} \begin{pmatrix} E_x^n \\ E_y^n \\ E_z^n \end{pmatrix} + \frac{Z^n e \Delta t}{2 m_{\mathrm{i}}^n} \begin{pmatrix} v_{\mathrm{i}y}^{n-\frac{1}{2}} B_z^n - v_{\mathrm{i}z}^{n-\frac{1}{2}} B_y^n \\ v_{\mathrm{i}z}^{n-\frac{1}{2}} B_x^n - v_{\mathrm{i}x}^{n-\frac{1}{2}} B_z^n \\ v_{\mathrm{i}x}^{n-\frac{1}{2}} B_y^n - v_{\mathrm{i}y}^{n-\frac{1}{2}} B_x^n \end{pmatrix}$$
$$- \frac{\eta Z^n e \Delta t}{\mu_0 m_{\mathrm{i}}^n} \begin{pmatrix} \frac{\partial B_z^n}{\partial y} - \frac{\partial B_y^n}{\partial z} \\ \frac{\partial B_x^n}{\partial z} - \frac{\partial B_z^n}{\partial x} \\ \frac{\partial B_y^n}{\partial x} - \frac{\partial B_x^n}{\partial y} \end{pmatrix} \tag{B.3}$$

Space derivative is defined as follows.

$$\frac{\partial B_z^n}{\partial y} = D_y B_z^n \tag{B.4}$$

The second term of l.h.s and third term of r.h.s. in Eq. (B.3) are expressed by the following definition.

$$\begin{pmatrix} \alpha \\ \beta \\ \gamma \end{pmatrix} = \frac{Z^n e \Delta t}{2 m_{\mathrm{i}}^n} \begin{pmatrix} B_x^n \\ B_y^n \\ B_z^n \end{pmatrix} \tag{B.5}$$

Equation (B.6) is given by the definitions Eqs. (B.4) and (B.5).

$$
\begin{aligned}
&\begin{pmatrix} v_{\mathrm{i}x}^{n+\frac{1}{2}} \\ v_{\mathrm{i}y}^{n+\frac{1}{2}} \\ v_{\mathrm{i}z}^{n+\frac{1}{2}} \end{pmatrix} - \begin{pmatrix} v_{\mathrm{i}y}^{n+\frac{1}{2}}\gamma - v_{\mathrm{i}z}^{n+\frac{1}{2}}\beta \\ v_{\mathrm{i}z}^{n+\frac{1}{2}}\alpha - v_{\mathrm{i}x}^{n+\frac{1}{2}}\gamma \\ v_{\mathrm{i}x}^{n+\frac{1}{2}}\beta - v_{\mathrm{i}y}^{n+\frac{1}{2}}\alpha \end{pmatrix} \\
&= \begin{pmatrix} v_{\mathrm{i}x}^{n-\frac{1}{2}} \\ v_{\mathrm{i}y}^{n-\frac{1}{2}} \\ v_{\mathrm{i}z}^{n-\frac{1}{2}} \end{pmatrix} + \frac{Z^n e\Delta t}{m_{\mathrm{i}}^n} \begin{pmatrix} E_x^n \\ E_y^n \\ E_z^n \end{pmatrix} + \begin{pmatrix} v_{\mathrm{i}y}^{n-\frac{1}{2}}\gamma - v_{\mathrm{i}z}^{n-\frac{1}{2}}\beta \\ v_{\mathrm{i}z}^{n-\frac{1}{2}}\alpha - v_{\mathrm{i}x}^{n-\frac{1}{2}}\gamma \\ v_{\mathrm{i}x}^{n-\frac{1}{2}}\beta - v_{\mathrm{i}y}^{n-\frac{1}{2}}\alpha \end{pmatrix} - \frac{\eta Z^n e\Delta t}{\mu_0 m_{\mathrm{i}}^n} \begin{pmatrix} D_y B_z^n - D_z B_y^n \\ D_z B_x^n - D_x B_z^n \\ D_x B_y^n - D_y B_x^n \end{pmatrix}
\end{aligned}
$$

$$
\begin{aligned}
&\begin{pmatrix} 1 & -\gamma & \beta \\ \gamma & 1 & -\alpha \\ -\beta & \alpha & 1 \end{pmatrix} \begin{pmatrix} v_{\mathrm{i}x}^{n+\frac{1}{2}} \\ v_{\mathrm{i}y}^{n+\frac{1}{2}} \\ v_{\mathrm{i}z}^{n+\frac{1}{2}} \end{pmatrix} \\
&= \begin{pmatrix} v_{\mathrm{i}x}^{n-\frac{1}{2}} + \frac{Z^n e\Delta t}{m_{\mathrm{i}}^n} E_x^n + \gamma v_{\mathrm{i}y}^{n-\frac{1}{2}} - \beta v_{\mathrm{i}z}^{n-\frac{1}{2}} \\ v_{\mathrm{i}y}^{n-\frac{1}{2}} + \frac{Z^n e\Delta t}{m_{\mathrm{i}}^n} E_y^n + \alpha v_{\mathrm{i}z}^{n-\frac{1}{2}} - \gamma v_{\mathrm{i}x}^{n-\frac{1}{2}} \\ v_{\mathrm{i}z}^{n-\frac{1}{2}} + \frac{Z^n e\Delta t}{m_{\mathrm{i}}^n} E_z^n + \beta v_{\mathrm{i}x}^{n-\frac{1}{2}} - \alpha v_{\mathrm{i}y}^{n-\frac{1}{2}} \end{pmatrix} - \frac{\eta Z^n e\Delta t}{\mu_0 m_{\mathrm{i}}^n} \begin{pmatrix} D_y B_z^n - D_z B_y^n \\ D_z B_x^n - D_x B_z^n \\ D_x B_y^n - D_y B_x^n \end{pmatrix}
\end{aligned}
\tag{B.6}
$$

Here, $\boldsymbol{A}$ and $\boldsymbol{S}$ are defined as follows, respectively.

$$
\boldsymbol{A} = \begin{pmatrix} 1 & -\gamma & \beta \\ \gamma & 1 & -\alpha \\ -\beta & \alpha & 1 \end{pmatrix}
$$

$$
\boldsymbol{S} = \begin{pmatrix} v_{\mathrm{i}x}^{n-\frac{1}{2}} + \frac{Ze\Delta t}{m_{\mathrm{i}}} E_x^n + \gamma v_{\mathrm{i}y}^{n-\frac{1}{2}} - \beta v_{\mathrm{i}z}^{n-\frac{1}{2}} \\ v_{\mathrm{i}y}^{n-\frac{1}{2}} + \frac{Ze\Delta t}{m_{\mathrm{i}}} E_y^n + \alpha v_{\mathrm{i}z}^{n-\frac{1}{2}} - \gamma v_{\mathrm{i}x}^{n-\frac{1}{2}} \\ v_{\mathrm{i}z}^{n-\frac{1}{2}} + \frac{Ze\Delta t}{m_{\mathrm{i}}} E_z^n + \beta v_{\mathrm{i}x}^{n-\frac{1}{2}} - \alpha v_{\mathrm{i}y}^{n-\frac{1}{2}} \end{pmatrix} - \frac{\eta Ze\Delta t}{\mu_0 m_{\mathrm{i}}} \begin{pmatrix} D_y B_z^n - D_z B_y^n \\ D_z B_x^n - D_x B_z^n \\ D_x B_y^n - D_y B_x^n \end{pmatrix}
$$

$\boldsymbol{v}_{\mathrm{i}}^{n+\frac{1}{2}}$ is expressed as follows by using $\boldsymbol{A}$ and $\boldsymbol{S}$.

$$\boldsymbol{A}\boldsymbol{v}_{\mathrm{i}}^{n+\frac{1}{2}} = \boldsymbol{S}$$

$$\boldsymbol{v}_{\mathrm{i}}^{n+\frac{1}{2}} = \boldsymbol{A}^{-1}\boldsymbol{S}$$

$$\boldsymbol{A}^{-1} = \frac{1}{1+\alpha^2+\beta^2+\gamma^2}\begin{pmatrix} 1+\alpha^2 & \alpha\beta+\gamma & \alpha\gamma-\beta \\ \alpha\beta-\gamma & 1+\beta^2 & \beta\gamma+\alpha \\ \alpha\gamma+\beta & \beta\gamma-\alpha & 1+\gamma^2 \end{pmatrix}$$

Finally, $v_{\mathrm{i}x}^{n+\frac{1}{2}}$ is obtained as follows.

$$\begin{aligned} v_{\mathrm{i}x}^{n+\frac{1}{2}} = & \frac{1}{1+\alpha^2+\beta^2+\gamma^2} \\ & \Bigg[(1+\alpha^2)\left\{v_{\mathrm{i}x}^{n-\frac{1}{2}} + \frac{Z^n e\Delta t}{m_{\mathrm{i}}^n}\left[E_x^n + \frac{1}{2}(B_z^n v_{\mathrm{i}y}^{n-\frac{1}{2}} - B_y^n v_{\mathrm{i}z}^{n-\frac{1}{2}}) - \frac{\eta}{\mu_0}(D_y B_z^n - D_z B_y^n)\right]\right\} \\ & + (\alpha\beta+\gamma)\left\{v_{\mathrm{i}y}^{n-\frac{1}{2}} + \frac{Z^n e\Delta t}{m_{\mathrm{i}}^n}\left[E_y^n + \frac{1}{2}(B_x^n v_{\mathrm{i}z}^{n-\frac{1}{2}} - B_z^n v_{\mathrm{i}x}^{n-\frac{1}{2}}) - \frac{\eta}{\mu_0}(D_z B_x^n - D_x B_z^n)\right]\right\} \\ & + (\alpha\gamma-\beta)\left\{v_{\mathrm{i}z}^{n-\frac{1}{2}} + \frac{Z^n e\Delta t}{m_{\mathrm{i}}^n}\left[E_z^n + \frac{1}{2}(B_y^n v_{\mathrm{i}x}^{n-\frac{1}{2}} - B_x^n v_{\mathrm{i}y}^{n-\frac{1}{2}}) - \frac{\eta}{\mu_0}(D_x B_y^n - D_y B_x^n)\right]\right\}\Bigg] \end{aligned}$$

B.2 x component of $\boldsymbol{E}^n$

We derive x component of $\boldsymbol{E}^n$ for Eq. (3.17) in the Chapter 3. This is much of the same for E_y^n and E_z^n.

$$\boldsymbol{E}^n = -\frac{1}{Z^n e n_{\mathrm{i}}^n}\left\{\left(\boldsymbol{j}_{\mathrm{i}}^n - \frac{\nabla\times\boldsymbol{B}^n}{\mu_0}\right)\times\boldsymbol{B}^n + k_{\mathrm{B}}T_{\mathrm{e}}Z^n\nabla n_{\mathrm{i}}^n\right\} + \frac{\eta}{\mu_0}\nabla\times\boldsymbol{B}^n$$

$$\begin{aligned} E_x^n = & \frac{1}{\mu_0 Z^n e n_{\mathrm{i}}^n}\left\{\left(\frac{\partial B_x^n}{\partial z} - \frac{\partial B_z^n}{\partial x}\right)B_z^n - \left(\frac{\partial B_y^n}{\partial x} - \frac{\partial B_x^n}{\partial y}\right)B_y^n\right\} \\ & - \frac{1}{Z^n e n_{\mathrm{i}}^n}\left(j_{\mathrm{i}y}^n B_z^n - j_{\mathrm{i}z}^n B_y^n\right) - \frac{k_{\mathrm{B}}T_{\mathrm{e}}}{e n_{\mathrm{i}}^n}\frac{\partial n_{\mathrm{i}}^n}{\partial x} + \frac{\eta}{\mu_0}\left(\frac{\partial B_z^n}{\partial y} - \frac{\partial B_y^n}{\partial z}\right) \end{aligned}$$

Appendix C

Neumann boundary condition

At the calculation boundary, the outflow particles are crossing simply and the electromagnetic field is kept constant. The field at the boundary is interpolated by only the known physical quantities of the inside cells. For an orthogonal cell, this is simple, since the volume which has to be filled is a slice of this cell, which is again simply an orthogonal volume. For a nonorthogonal cell, this volume is more complicated and it is difficult to place the particles inside this volume with the correct distribution function. Figure C.1 shows the calculation boundary. The red and blue cells indicate orthogonal and nonorthogonal cells, respectively.

Here, the boundary condition adopted for the field quantities ϕ is that the spatial differences of the normal components $\partial\phi/\partial\boldsymbol{n}$ are set to be zero; i.e., a Neumann boundary condition is adopted. We describe two examples for determining the physical quantity $\phi(P)$ at the point P, as shown in Fig. C.2.

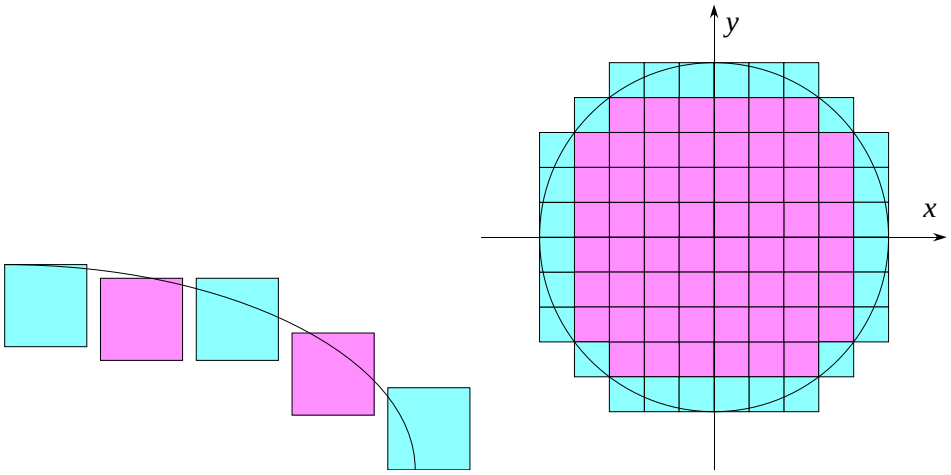

Figure C.1: Orthogonal and nonorthogonal cells.

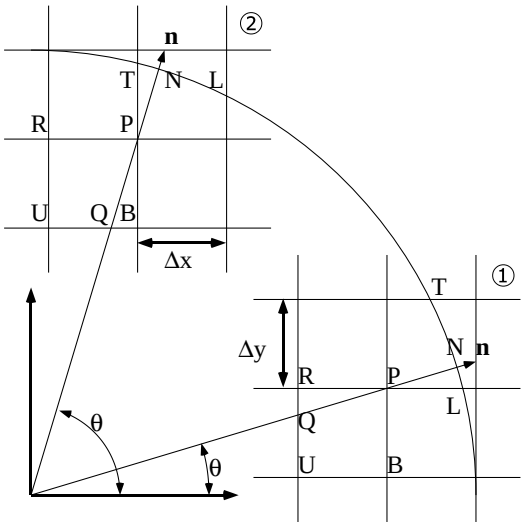

Figure C.2: Two examples of Neumann boundary condition.

1. From $\overline{RQ} = \Delta x \tan\theta$ and $\overline{QU} = \Delta y - \Delta x \tan\theta$, $\phi(Q)$ is expressed as follows, where the over line indicates the distance between two points.

$$\phi(Q) = \frac{\phi(R)(\Delta y - \Delta x \tan\theta) + \phi(U)\Delta x \tan\theta}{\Delta y} \tag{C.1}$$

From $\overline{PQ} = \Delta x / \cos\theta$ and Eq. (C.1), the normal component is expressed.

$$\begin{aligned}\frac{\partial\phi(N)}{\partial \boldsymbol{n}} &= \frac{\phi(P) - \phi(Q)}{\overline{PQ}} \\ &= \frac{\phi(P)\cos\theta}{\Delta x} - \frac{\phi(R)(\Delta y \cos\theta - \Delta x \sin\theta) + \phi(U)\Delta x \sin\theta}{\Delta x \Delta y}\end{aligned} \tag{C.2}$$

From Eq. (C.2), $\phi(P)$ is expressed when Δx is equal to Δy.

$$\begin{aligned}\phi(P) &= \frac{\Delta x}{\cos\theta}\frac{\partial\phi(N)}{\partial \boldsymbol{n}} + \frac{\phi(R)(\Delta y \cos\theta - \Delta x \sin\theta) + \phi(U)\Delta x \sin\theta}{\Delta y \cos\theta} \\ &= \frac{\Delta x}{\cos\theta}\frac{\partial\phi(N)}{\partial \boldsymbol{n}} + \phi(R)(1 - \tan\theta) + \phi(U)\tan\theta\end{aligned} \tag{C.3}$$

By substituing $\partial\phi(N)/\partial \boldsymbol{n} = 0$ into Eq. (C.3), $\phi(P)$ is obtained as follows.

$$\phi(P) = \phi(U)\tan\theta + \phi(R)(1 - \tan\theta)$$

2. From $\overline{UQ} = \Delta x - \Delta y / \tan\theta$ and $\overline{QB} = \Delta y / \tan\theta$, $\phi(Q)$ is expressed as follows.

$$\phi(Q) = \frac{\phi(U)\frac{\Delta y}{\tan\theta} + \phi(B)\left(\Delta x - \frac{\Delta y}{\tan\theta}\right)}{\Delta x} \tag{C.4}$$

From $\overline{PQ} = \Delta y / \sin\theta$ and Eq. (C.4), the normal component is expressed.

$$\begin{aligned}\frac{\partial \phi(N)}{\partial \boldsymbol{n}} &= \frac{\phi(P) - \phi(Q)}{\overline{PQ}} \\ &= \frac{\phi(P)\sin\theta}{\Delta y} - \frac{\phi(U)\Delta y\cos\theta + \phi(B)(\Delta x\sin\theta - \Delta y\cos\theta)}{\Delta x \Delta y}\end{aligned} \tag{C.5}$$

From Eq. (C.5), $\phi(P)$ is expressed when Δx is equal to Δy.

$$\begin{aligned}\phi(P) &= \frac{\Delta y}{\sin\theta}\frac{\partial \phi(N)}{\partial \boldsymbol{n}} + \frac{\phi(U)\Delta y\cos\theta + \phi(B)(\Delta x\sin\theta - \Delta y\cos\theta)}{\Delta x\sin\theta} \\ &= \frac{\Delta y}{\sin\theta}\frac{\partial \phi(N)}{\partial \boldsymbol{n}} + \frac{\phi(U)}{\tan\theta} + \phi(B)\left(1 - \frac{1}{\tan\theta}\right)\end{aligned} \tag{C.6}$$

By substituting $\partial\phi(N)/\partial \boldsymbol{n} = 0$ into Eq. (C.6), $\phi(P)$ is obtained as follows.

$$\phi(P) = \frac{\phi(U)}{\tan\theta} + \phi(B)\left(1 - \frac{1}{\tan\theta}\right)$$

Appendix D

Normalization

All physical quantities used in 3D hybrid PIC code are normalized as follows to reduce the calculation error and prevent the calculation from divergence.

Length;	$\tilde{x} = \dfrac{x}{c\Delta t}$
Mesh width;	$\Delta\tilde{x} = \dfrac{\Delta x}{c\Delta t}$
Velocity;	$\tilde{v} = \dfrac{v}{c}$
Magnetic field;	$\tilde{B} = B \cdot \dfrac{Ze\Delta t}{m_{\mathrm{i}}}$
Electric field;	$\tilde{E} = E \cdot \dfrac{Ze\Delta t}{cm_{\mathrm{i}}}$
Current density;	$\tilde{j} = j \cdot \dfrac{c^2\Delta t^3}{Ze}$
Particle density;	$\tilde{n} = n(c\Delta t)^3$
Resistivity;	$\tilde{\eta} = \dfrac{1}{\mu_0 c^2 \Delta t}\eta$

Appendix E

CFL condition

Time step Δt and mesh width Δx are limited by Courant-Friedrichs-Lewy (CFL) condition for solving partial differential equations numerically. This CFL condition is easily derived from the wave dispersion relation. Here, $A(x,t)$ is expressed, where $\hat{A}$ is complex magnitude, k is the wave number and ω is the frequency.

$$A(x,t) = \hat{A}\exp(ikx - i\omega t)$$

Here, the spatial central difference at x_0 is considered.

$$\begin{aligned}\frac{\Delta A}{\Delta x} &= \frac{A(x_0 + \Delta x/2, t) - A(x_0 - \Delta x/2, t)}{\Delta x} \\ &= \frac{\exp(ik\Delta x/2) - \exp(-ik\Delta x/2)}{\Delta x} A(x_0, t) \\ &= i\frac{\sin(k\Delta x/2)}{\Delta x/2} A(x_0, t) \end{aligned} \tag{E.1}$$

By comparing Eq. (E.1) with $\partial A/\partial x$, the wave number is expressed as follows.

$$K = \frac{\sin(k\Delta x/2)}{\Delta x/2} \tag{E.2}$$

This is much of the same for ω by using Ω.

$$\Omega = \frac{\sin(\omega\Delta t/2)}{\Delta t/2} \tag{E.3}$$

The wave dispersion relation is $\omega^2 = c^2k^2$. c is the speed of light. From replacing k and ω by Eqs. (E.2) and (E.3), $\Omega^2 = c^2K^2$. Since the maximum wave number is $k_{\max} = \pi/\Delta x$,

$$\sin^2(\omega\Delta t/2) = \left(\frac{c\Delta t}{\Delta x}\right)^2 \tag{E.4}$$

is obtained. When $c\Delta t/\Delta x > 1$, ω becomes complex and the calculation becomes unstable and diverges. Since hybrid PIC code uses the implicit method not the explicit method, c is replaced by the Alfven speed V_A. Then, the CFL condition is $\Delta t < \Delta x/V_A$.